SANDIA REPORT

SAND2012-7764
Unlimited Release
Printed September 2012

Phase Diversity for Advanced Systems

Eric A. Shields, James K. Gruetzner, and Gregory R. Brady

Prepared by
Sandia National Laboratories
Albuquerque, New Mexico 87185 and Livermore, California 94550

Sandia National Laboratories is a multi-program laboratory managed and operated by Sandia Corporation, a wholly owned subsidiary of Lockheed Martin Corporation, for the U.S. Department of Energy's National Nuclear Security Administration under contract DE-AC04-94AL85000.

Approved for public release; further dissemination unlimited.

Sandia National Laboratories

Issued by Sandia National Laboratories, operated for the United States Department of Energy by Sandia Corporation.

NOTICE: This report was prepared as an account of work sponsored by an agency of the United States Government. Neither the United States Government, nor any agency thereof, nor any of their employees, nor any of their contractors, subcontractors, or their employees, make any warranty, express or implied, or assume any legal liability or responsibility for the accuracy, completeness, or usefulness of any information, apparatus, product, or process disclosed, or represent that its use would not infringe privately owned rights. Reference herein to any specific commercial product, process, or service by trade name, trademark, manufacturer, or otherwise, does not necessarily constitute or imply its endorsement, recommendation, or favoring by the United States Government, any agency thereof, or any of their contractors or subcontractors. The views and opinions expressed herein do not necessarily state or reflect those of the United States Government, any agency thereof, or any of their contractors.

Printed in the United States of America. This report has been reproduced directly from the best available copy.

Available to DOE and DOE contractors from
U.S. Department of Energy
Office of Scientific and Technical Information
P.O. Box 62
Oak Ridge, TN 37831

Telephone: (865) 576-8401
Facsimile: (865) 576-5728
E-Mail: reports@adonis.osti.gov
Online ordering: http://www.osti.gov/bridge

Available to the public from
U.S. Department of Commerce
National Technical Information Service
5285 Port Royal Rd.
Springfield, VA 22161

Telephone: (800) 553-6847
Facsimile: (703) 605-6900
E-Mail: orders@ntis.fedworld.gov
Online order: http://www.ntis.gov/help/ordermethods.asp?loc=7-4-0#online

SAND2012-7064
Unlimited Release
Printed September 2012

Phase Diversity for Advanced Systems

Eric A. Shields
Optical Payload Design and Realization

James K. Gruetzner
Directed Energy Laser Applications

Gregory R. Brady
Photonic Microsystem Technologies

Sandia National Laboratories
P.O. Box 5800
Albuquerque, New Mexico 87185-MS0406

Abstract

Phase diversity (PD) is an image processing technique that operates on a collection of defocused images of a scene. The ensemble of defocused images and known defocus values are used to reconstruct the un-aberrated scene and the wavefront of the imaging system. PD has successfully been applied to imaging systems with limited fields of view (FOV) over narrow spectral bands.

Theoretical development has not addressed issues of field-dependent aberrations inherent in systems with larger fields of view. Algorithms which can accommodate wavelength-dependent aberrations in systems with broad spectral content have also largely been ignored.

This report presents research into the second of these issues. An algorithm is presented that theoretically enables reconstruction of wavelength-dependent wavefront data from images of a broadband point source. The theoretical basis of this algorithm is presented and an experimental study into its utility are presented.

ACKNOWLEDGMENTS

The authors would like to acknowledge Sandia's Laboratory Directed Research and Development (LDRD) Office. This work was funded and performed as a two-year LDRD program.

CONTENTS

1 Introduction 11

2Equation Section 2 Monochromatic Phase-Diverse Phase Retrieval 13
2.1 Variable Definitions 13
2.2 Mathematical Theory 15
2.2.1 Optical Model 15
2.2.2 Objective Function 17
2.2.3 Gradient with respect to PSF Estimates 19
2.2.4 Gradient with respect to Transverse Shifts 21
2.2.5 Gradient with respect to Optical Intensity Estimates 23
2.2.6 Gradient with respect to Defocus Amounts 24
2.2.7 Gradient with respect to Pupil Phase 27
2.2.8 Gradient with respect to Pupil Amplitude 29
2.3 Optimization 30
2.4 Phase Diversity Testbed 31
2.4.1 Testbed Design 31
2.4.2 Interferometric Measurements 33
2.4.3 Phase Diversity Reconstructions 35

3Equation Section 3 Broadband Phase-Diverse Phase retrieval 45
3.1 Variable Definitions 45
3.2 Mathematical Theory 45
3.2.1 Optical Model 45
3.2.2 Objective Function 46
3.2.3 Unchanged Gradients 47
3.2.4 Gradient with respect to Defocus Amounts 47
3.2.5 Gradient with respect to Pupil Phase 50
3.2.6 Gradient with respect to Spectral Weights 52

4Equation Section 4 Broadband Simulation 53
4.1 Simulation at Five Discrete Wavelengths 53

5Equation Section 5 Experimental Testing 56
5.1 Simulations of Broadband Images 57
5.2 632.8 nm Monochromatic Testing 65
5.3 405 nm Monochromatic Testing 67
5.4 Two-Wavelength Testing 70

6Equation Section 6 Conclusions 75

7Equation Section 7 References 77

FIGURES

Figure 1: Monochromatic Testbed in the Interferometric Configuration 32
Figure 2: Monochromatic Testbed in the Phase Diversity Configuration 32
Figure 3: Interferometrically-Measured Wavefronts Analyzed for Monochromatic PDPR 34
Figure 4: Interferometrically-Measured Wavefronts Decomposed to 37 Zernike Terms 35
Figure 5: Wavefront Reconstructions Using the Trust-Region Algorithm..... 37
Figure 6: Wavefront Reconstructions Using the Conjugate Gradient Algorithm..... 37
Figure 7: Wavefront Reconstructions Using the Quasi-Newton Algorithm..... 38
Figure 8: Measured and Reconstructed PSFs for Wavefront A..... 40
Figure 9: Measured and Reconstructed PSFs for Wavefront B..... 41
Figure 10: Measured and Reconstructed PSFs for Wavefront C..... 41
Figure 11: Measured and Reconstructed PSFs for Wavefront D..... 42
Figure 12: Objective Function Values vs. Defocus with Linear Transverse PSF Motion..... 43
Figure 13: Objective Function Values versus Defocus after Optimizing Lateral Shifts 44
Figure 14: Basic optical model used in simulations 53
Figure 15: Histograms of wavefronts after phase diversity reconstruction:..... 54
Figure 16: Results using 7thorder Zernike polynomials for simulation and reconstruction: 56
Figure 17: Dual-Wavelength Phase-Diverse Phase Retrieval Testbed Configuration 57
Figure 18: Log of the error function versus iteration step for an arbitrary simulation:..... 59
Figure 19: Histograms showing phase errors for 50 simulation runs in each set:..... 59
Figure 20: Wavefront reconstructions at 525 nm for an arbitrarily selected simulation:..... 62
Figure 21: Wavefront reconstructions at 633 nm for an arbitrarily selected simulation:..... 63
Figure 22: Wavefront reconstructions at 725 nm for an arbitrarily selected simulation:..... 64
Figure 23: Reconstructed Wavefront at 632.8 nm without Piston, Tip, Tilt, and Power 65
Figure 24: Interferometrically Measured Wavefront fit to 37 Zernike Terms..... 66
Figure 25: NRMSE vs. Position for the 632.8 nm Phase Diversity Reconstruction 66
Figure 26: Measured and Reconstructed PSFs at -4 mm Position for the 632.8 nm Test 67
Figure 27: Reconstructed Wavefront at 405 nm without Piston, Tip, Tilt, and Power 67
Figure 28: NRMSE vs. Position for the 405 nm Phase Diversity Reconstruction 68
Figure 29: Measured and Reconstructed PSFs at 0.5 mm Position for the 405 nm Test..... 68
Figure 30: Zemax Model of 632.8 nm Wavefront assuming 1.45° Lens Tilt..... 69
Figure 31: Zemax Model of 405 nm Wavefront assuming 1.45° Lens Tilt..... 70
Figure 33: Simulation of testbed..... 71
Figure 33: Wavefront images from arbitrary simulation. 71
Figure 34: 405 nm Wavefront Reconstructed from Two-Wavelength Data..... 72
Figure 35: 632.8 nm Wavefront Reconstructed from Two-Wavelength Data..... 72
Figure 36: NRMSE vs. Position for the Two-Wavelength Phase Diversity Reconstruction..... 73
Figure 37: Measured and Reconstructed PSFs at 8 mm Position for the Two-Wavelength Test. 73
Figure 38: The First 15 Standard Zernike Polynomials..... 79

TABLES

Table 1: Comparison of Monochromatic Reconstruction Results 36
Table 2: Zernike Coefficients for Wavefront A 38
Table 3: Zernike Coefficients for Wavefront B 39
Table 4: Zernike Coefficients for Wavefront C 39
Table 5: Zernike Coefficients for Wavefront D 39
Table 6: Definition of the First 15 Standard Zernike Polynomials 80

ACRONYMS

DFT	Discrete Fourier transform
DOE	Department of Energy
FOV	Field of view
FPA	Focal plane array
IDFT	Inverse discrete Fourier transform
LDRD	Laboratory directed research and development
NRMSE	Normalized root-mean-square error
PD	Phase diversity
PDPR	Phase-diverse phase retrieval
PSF	Point-source function
QTH	Quartz tungsten halogen
RMS	Root mean square
SNL	Sandia National Laboratories

1 INTRODUCTION

In a traditional imaging system, a measured scene is the convolution of the actual scene with the system point-source function (PSF). The shape of the point-spread function is affected by diffraction, optical aberrations, focal plane sampling, focal plane charge diffusion, motion blur, and other effects. These effects are deleterious to the imaging process since the goal is to obtain the scene in the absence of these effects.

We focus here on the effects of diffraction and optical aberrations. The impacts of these on the point-spread function are well understood; the PSF is the square of the Fourier transform of the complex pupil function. If one knows the complex pupil function of the system one can correct imagery to account for the effects of diffraction and optical aberration.

Traditionally the magnitude of the complex pupil function is well known. The magnitude is simply the shape of the aperture of the system. For many optical systems this is simply a circular disk, in which case the pupil function is unity inside the disk and zero outside. More complicated optical systems may have a central obscuration and support structure. However, the geometry of the obscuration and support structure are generally well known as well.

Hence investigation of the complex pupil function is generally limited to its phase. The phase of the complex pupil function is known as the system aberration. The wavefront of an optical system is the shape of a surface of constant phase at the exit pupil of an optical system. For a diffraction-limited system the wavefront is spherical. Deviations from this spherical shape are called aberrations. Note that the term aberrations and wavefront are often intermingled and the base spherical nature of the wavefront is generally neglected.

The key to understanding the performance of a system is therefore measurement of the system wavefront. Interferometry is generally used for this purpose. Traditional interferometric measurements involve the use of a laser source which passes light through the optical system, off of a specialized return mirror, through the optical system a second time, and back to a detector within the interferometer. Light at the detector is coherently interfered with a reference beam of known wavefront so that the wavefront difference can be measured.

Phase retrieval algorithms have also been used to reconstruct the system wavefront from a measurement of the system point-spread function. The accuracy and converge rates of these algorithms can be improved by using multiple measurements where the wavefront has been changed in a known manner between measurements. For example, measurements may be taken at different defocus depths. Such algorithms are referred to as phase-diverse phase retrieval (PDPR).

The theory behind phase-diverse phase retrieval is presented in Section 2 below. Inherent in the formulation of traditional PDPR theory is that light is monochromatic. In spectrally broad systems, the wavefront error varies as a function of wavelength. Previous studies have investigated the use of PDPR on spectrally broad systems, but the variation in wavelength was assumed known since the optical system being modeled was reflective (J. R. Fienup 1999).

We seek to extend the theory of phase-diverse phase retrieval to the case where the wavefront error is allowed to vary in an unknown manner as a function of wavelength. Such would be the case for a system with significant wavefront error due to refractive components. We wish to reconstruct the wavefront as a function of wavelength from measurements of the PSF made at a number of different defocus depths.

If successful, this algorithm would present a new and useful way of characterizing the performance of an optical system. By reconstructing wavefront as a function of wavelength, optical engineers could build more accurate models of the system. Furthermore, imagery could be corrected more accurately in post-processing using deconvolution techniques with the reconstructed, broadband PSF.

Another interesting application arises. The algorithm allows for the spectral weights to be optimized as well. A mission could be developed where the wavefront of the optical system as a function of wavelength is characterized by application of the algorithm on a known point source (i.e., the spectral content of the point source is known). Once this information is obtained, the system could be pointed at a point source of unknown spectral content. Since the wavefront of the system as a function of wavelength is known, the algorithm would be run to optimize the spectral weights. In this manner the spectral content of a point source could be measured with a panchromatic imaging system.

2 MONOCHROMATIC PHASE-DIVERSE PHASE RETRIEVAL

The mathematics used for broadband phase-diverse phase retrieval is closely related to the monochromatic phase-diverse phase retrieval algorithm presented by Thurman (Thurman, DeRosa and Fienup 2009). The mathematical theory is presented briefly in that paper. This chapter presents that theory in more detail so that the underlying math can be better understood.

2.1 Variable Definitions

Variable definitions are given in this section. Variables with a caret (^) over them are estimates. DFT[] is used to represent the discrete Fourier transform operation while IDFT[] is used to represent the inverse discrete Fourier transform operation.

K: The number of diversity measurements

$k = 1, 2, \ldots K$: Index on the diversity measurements

α_k: Scaling coefficients used to minimize the objective function

M: The number of data points in transverse dimension 1

N: The number of data points in transverse dimension 2

$m \in \left\{-\frac{M}{2}, -\frac{M}{2}+1, \ldots \frac{M}{2}-1\right\}$: Index of dimension 1 in pupil plane space

$n \in \left\{-\frac{N}{2}, -\frac{N}{2}+1, \ldots \frac{N}{2}-1\right\}$: Index of dimension 2 in pupil plane space

$p \in \left\{-\frac{M}{2}, -\frac{M}{2}+1, \ldots \frac{M}{2}-1\right\}$: Index of dimension 1 in image plane space

$q \in \left\{-\frac{N}{2}, -\frac{N}{2}+1, \ldots \frac{N}{2}-1\right\}$: Index of dimension 2 in image plane space

$\hat{A}(m,n)$: Estimate of the amplitude at the pupil plane

$\hat{\phi}(m,n)$: Estimated phase at the pupil plane

$\hat{E}_p(m,n) = \hat{A}(m,n)\exp\left[i\hat{\phi}(m,n)\right]$: Estimated complex field at the pupil plane

$\hat{A}(m,n) = \dfrac{MN\left|\hat{B}(m,n)\right|}{\sum_{m',n'}\left|\hat{B}(m',n')\right|}$: definition of the dummy function $\hat{B}(m,n)$

d: Distance from the pupil plane to the lens

f: Focal length of the optical system

$Z_j(m,n)$: The basis functions for $\hat{\phi}$(m,n)

$\hat{E}_f(p,q) = \mathrm{DFT}\left[\hat{\mathrm{E}}_p(m,n)\right]$

$\hat{E}_f(p,q) = \dfrac{1}{\sqrt{MN}}\sum_{m,n}\hat{E}_p(m,n)\exp\left[-i2\pi\left(\dfrac{mp}{M}+\dfrac{nq}{N}\right)\right]$: Optical field in the image plane

$\Delta_p = \Delta_q = \Delta_d$: Detector pitch

$\Delta_m = \dfrac{1}{M\Delta_p} = \dfrac{1}{M\Delta_d}$: Sample spacing in dimension 1 in the pupil plane

$\Delta_n = \dfrac{1}{N\Delta_q} = \dfrac{1}{N\Delta_d}$: Sample spacing in dimension 2 in the pupil plane

$\hat{U}_f(m,n) = \mathrm{DFT}\left[\hat{\mathrm{E}}_f(p,q)\right]$:

Estimated angular plane-wave spectrum in the back focal plane of the image lens

$\hat{\mathrm{z}}_k$: Estimated kth defocus amount

$\hat{U}_k(m,n) = \hat{U}_f(m,n)\exp\left[2\pi\hat{z}_k\sqrt{\dfrac{1}{\lambda^2} - m^2\Delta_m^2 - n^2\Delta_n^2}\right]$:

Estimated angular plane-wave spectrum at the kth image plane

$\hat{E}_k(p,q) = \mathrm{IDFT}\left[\hat{U}_k(m,n)\right]$: Estimated optical field at the kth image plane

$\hat{I}_k(p,q) = \left|\hat{E}_k(p,q)\right|^2$: Estimated intensity at the kth image plane

f_d: Area fill factor of the detector

$H_d(m,n) = \mathrm{sinc}\left(\dfrac{\sqrt{f_d}}{N}n\right)\mathrm{sinc}\left(\dfrac{\sqrt{f_d}}{M}m\right)$: Detector transfer function

$\hat{p}_{s,k}$: Estimated transverse shift of image k in direction 1 in units of pixels

$\hat{q}_{s,k}$: Estimated transverse shift of image k in direction 2 in units of pixels

$\mathrm{H}_{s,k}(m,n) = \exp\left[-i2\pi\left(\dfrac{m\hat{p}_{s,k}}{M} + \dfrac{n\hat{q}_{s,k}}{N}\right)\right]$:

Transfer function for estimated transverse shift of kth image

$\hat{\mathrm{f}}_k(m,n) = \mathrm{DFT}\left[\hat{I}_k(p,q)\right]$: Fourier transform of the estimated intensity of the kth image

$\hat{g}_k(m,n) = \mathrm{H}_{s,k}(m,n)H_d(m,n)\hat{\mathrm{f}}_k(m,n)$:

Fourier transform of the estimated point-spread function

$G_k(p,q)$: kth measured point-spread function

$\hat{\mathrm{G}}_k(p,q) = \mathrm{IDFT}\left[\hat{g}_k(m,n)\right]$: Estimated point-spread function

$\mathrm{W}_k(p,q)$: Pixel weights in the image plane

$\Phi_d(p,q)$: Objective function to be minimized

$\mathbb{R}$: The set of real numbers

J: The number of basis functions to be considered in the phase decomposition

2.2 Mathematical Theory

In this section we develop the mathematical theory for the phase-diverse phase retrieval algorithm. First the mathematics of the optical system are developed. Then an objective function to be minimized is defined.

2.2.1 Optical Model

We write the estimated optical field $\hat{E}_p(m,n)$ in the pupil plane as

$$\hat{E}_p(m,n) = \hat{A}(m,n)\exp\left[i\hat{\phi}(m,n)\right], \tag{2.1}$$

where m and n are indices in the pupil plane space, $\hat{A}(m,n)$ is the estimated pupil amplitude, and $\hat{\phi}(m,n)$ is the estimated pupil phase in radians.

To calculate the optical field $\hat{E}_f(p,q)$ at the nominal focal plane of the image system, we calculate the discrete Fourier transform (DFT) of the pupil plane optical amplitude. Thus we have

$$\hat{E}_f(p,q) = \frac{1}{\sqrt{MN}}\sum_{m,n}\hat{E}_p(m,n)\exp\left[-i2\pi\left(\frac{mp}{M}+\frac{nq}{N}\right)\right], \tag{2.2}$$

where p and q are indices in the focal plane space. Notice that in Equation (2.2) we have implicitly assumed that the pupil is in the front focal plane of the lens. For the more general case of a system with the pupil plane a distance d in front of the lens we have (Goodman 1996)

$$\hat{E}_f(p,q) = \frac{1}{\sqrt{MN}}\exp\left[\frac{i\pi}{\lambda f}\left(1-\frac{d}{f}\right)\left(p^2\Delta_p^2+q^2\Delta_q^2\right)\right]\sum_{m,n}\hat{E}_p(m,n)\exp\left[-i2\pi\left(\frac{mp}{M}+\frac{nq}{N}\right)\right], \tag{2.3}$$

A common assumption in phase diversity applications is to assume $d=0$, i.e., the pupil at the lens plane itself is calculated. Standard free-space propagation techniques can then be used to determine the phase at a distance in front of the lens.

The angular plane-wave spectrum technique for free space propagation is used to calculate the field at the various measurement planes. We calculate the angular plane-wave spectrum $\hat{U}_f(m,n)$ of the field $\hat{E}_f(p,q)$ by calculating its discrete Fourier transform. Thus we have

$$\hat{U}_f(m,n) = \frac{1}{\sqrt{MN}}\sum_{p,q}\hat{E}_f(p,q)\exp\left[-i2\pi\left(\frac{mp}{M}+\frac{nq}{N}\right)\right]. \tag{2.4}$$

The field at the *k*th defocus plane can then be calculated simply by multiplying by the free space transfer function. We have

$$\hat{U}_k(m,n) = \hat{U}_f(m,n)\exp\left[i2\pi\hat{z}_k\sqrt{\frac{1}{\lambda^2}-m^2\Delta_m^2-n^2\Delta_n^2}\right], \tag{2.5}$$

where $\hat{z}_k$ is the estimate of the *k*th defocus plane. Note that in Equation (2.5) we have neglected constant phase terms that do not affect the measured point-spread function.

The optical field at the kth defocus plane $\hat{E}_k(p,q)$ is obtained by calculating the inverse discrete Fourier transform (IDFT) of $\hat{U}_k(m,n)$. We therefore have

$$\hat{E}_k(p,q) = \frac{1}{\sqrt{MN}} \sum_{m,n} \hat{U}_k(m,n) \exp\left[+i2\pi \left(\frac{mp}{M} + \frac{nq}{N} \right) \right]. \tag{2.6}$$

Assuming a square-law detector we have the following equation for the computed intensity in the kth defocus plane $\hat{I}_k(p,q)$:

$$\hat{I}_k(p,q) = \left| \hat{E}_k(p,q) \right|^2 . \tag{2.7}$$

The detector modulation transfer function and spatial jitter in the measured point-spread functions are handled in the frequency domain. A simple model for an idealized detector modulation transfer function is

$$H_d(m,n) = \mathrm{sinc}\left(\frac{\sqrt{f_d}}{N} n \right) \mathrm{sinc}\left(\frac{\sqrt{f_d}}{M} m \right), \tag{2.8}$$

where f_d is the area fill factor of the detector and we assume the pixels are square. Diffusion effects associated with the focal plane could be accounted for in this term as well.

The transfer function associated with spatial jitter is

$$\mathrm{H}_{s,k}(m,n) = \exp\left[-i2\pi \left(\frac{m\hat{p}_{s,k}}{M} + \frac{n\hat{q}_{s,k}}{N} \right) \right], \tag{2.9}$$

where $\hat{p}_{s,k}$ and $\hat{q}_{s,k}$ are estimates of the transverse shifts of the PSF in units of pixels.

Since the detector and spatial jitter effects are considered in the frequency domain, the transfer function $\hat{\mathrm{f}}_k(m,n)$ associated with the estimated point-spread function must be calculated as well. This transfer function is simply the DFT of $\hat{I}_k(p,q)$ and thus we have

$$\hat{f}_k(m,n) = \frac{1}{\sqrt{MN}} \sum_{p,q} \hat{I}_k(p,q) \exp\left[-i2\pi \left(\frac{mp}{M} + \frac{nq}{N} \right) \right]. \tag{2.10}$$

The total estimated transfer function $\hat{g}_k(m,n)$ associated with the PSF, detector effects, and jitter effects is the product of the three terms, or

$$\hat{g}_k(m,n) = \mathrm{H}_{s,k}(m,n) H_d(m,n) \hat{\mathrm{f}}_k(m,n). \tag{2.11}$$

To calculate the estimated PSF $\hat{G}_k(p,q)$ we calculate the inverse discrete Fourier transform of $\hat{g}_k(m,n)$. That is,

$$\hat{G}_k(p,q) = \frac{1}{\sqrt{MN}} \sum_{m,n} \hat{g}_k(m,n) \exp\left[+i2\pi \left(\frac{mp}{M} + \frac{nq}{N} \right) \right]. \tag{2.12}$$

2.2.2 Objective Function

The error Φ_d between the estimated PSFs $\hat{G}_k(p,q)$ and measured PSFs $G_k(p,q)$ is given by (J. R. Fienup 1997):

$$\Phi_d = \frac{1}{K} \sum_{k=1}^{K} \left\{ \frac{\sum_{p,q} W_k(p,q) \left[\alpha_k \hat{G}_k(p,q) - G_k(p,q) \right]^2}{\sum_{p,q} W_k(p,q) G_k^2(p,q)} \right\}, \tag{2.13}$$

In Equation (2.13) $W_k(p,q)$ is a pixel weighting mask that can vary from measurement to measurement and α_k is a scaling factor that can vary from measurement to measurement as well. The mask $W_k(p,q)$ allows bad pixels to be masked out or regions of low signal to be weighted lower than regions of high signal. The scaling factor α_k allows for energy variations from measurement to measurement.

In practice the user supplies the weighting mask $W_k(p,q)$. One possible choice is to set W to zero for bad pixels and let it be unity everywhere else. Other possible choices exist as well, such as setting W to zero below a certain signal-to-noise level.

The scaling factor α_k can be determined analytically. To do this, the partial derivative of Φ_d with respect to α_k is taken. The following steps show this calculation. Note that the arguments (p,q) are omitted for brevity. We start by expanding the squared term in Equation (2.13) to obtain:

$$\Phi_d = \frac{1}{K} \sum_{k=1}^{K} \left\{ \frac{\sum_{p,q} W_k \left[\alpha_k^2 \hat{G}_k^2 - 2\alpha_k \hat{G}_k G_k + G_k^2 \right]}{\sum_{p,q} W_k G_k^2} \right\}. \tag{2.14}$$

We split the summation as shown:

$$\Phi_d = \frac{1}{K} \sum_{j \neq k}^{K} \left\{ \frac{\sum_{p,q} W_j \left[\alpha_j^2 \hat{G}_j^2 - 2\alpha_j \hat{G}_j G_j + G_j^2 \right]}{\sum_{p,q} W_j G_j^2} \right\} + \frac{1}{K} \frac{\sum_{p,q} W_k \left[\alpha_k^2 \hat{G}_k^2 - 2\alpha_k \hat{G}_k G_k + G_k^2 \right]}{\sum_{p,q} W_k G_k^2} \tag{2.15}$$

We then calculate the derivative of Φ_d with respect to α_k and set this equal to zero. The first term (involving the summation over *j*) in Equation (2.15) is independent of α_k and thus does not contribute to the derivative. We therefore have

$$\frac{\partial \Phi_d}{\partial \alpha_k} = 0 = \frac{1}{K} \frac{\sum_{p,q} W_k \left[2\alpha_k \hat{G}_k^2 - 2\hat{G}_k G_k \right]}{\sum_{p,q} W_k G_k^2}, \tag{2.16}$$

which implies that

$$\alpha_k \sum_{p,q} W_k \hat{G}_k^2 = \sum_{p,q} W_k G_k \hat{G}_k, \tag{2.17}$$

or, now inserting the (p,q) terms back,

$$\alpha_k = \frac{\sum_{p,q} W_k(p,q) \hat{G}_k(p,q) G_k(p,q)}{\sum_{p,q} W_k(p,q) \hat{G}_k^2(p,q)}. \tag{2.18}$$

We start the process of inserting Equation (2.18) into Equation (2.13) by further expanding Equation (2.14):

$$\Phi_d = \frac{1}{K} \sum_{k=1}^{K} \left\{ \frac{\sum_{p,q} W_k G_k^2}{\sum_{p,q} W_k G_k^2} \right\} - \frac{1}{K} \sum_{k=1}^{K} \left\{ \frac{\sum_{p,q} W_k \hat{G}_k \left[2\alpha_k G_k - \alpha_k^2 \hat{G}_k \right]}{\sum_{p,q} W_k G_k^2} \right\}, \text{ or} \tag{2.19}$$

$$\Phi_d = 1 - \frac{1}{K} \sum_{k=1}^{K} \left\{ \frac{\sum_{p,q} W_k \hat{G}_k \left[2\alpha_k G_k - \alpha_k^2 \hat{G}_k \right]}{\sum_{p,q} W_k G_k^2} \right\}. \tag{2.20}$$

Now we must remember the meaning of α_k, namely it is a scaling factor to get the estimate $\hat{G}_k$ to have the same scale as the measurement G_k. When the optimization is complete we therefore have

$$\alpha_k \hat{G}_k = G_k. \tag{2.21}$$

Using Equation (2.21) in Equation (2.20) yields

$$\Phi_d = 1 - \frac{1}{K} \sum_{k=1}^{K} \left\{ \frac{\sum_{p,q} \alpha_k W_k \hat{G}_k G_k}{\sum_{p,q} W_k G_k^2} \right\}. \tag{2.22}$$

Inserting Equation (2.18) into this expression yields

$$\Phi_d = 1 - \frac{1}{K}\sum_{k=1}^{K}\left\{\frac{\sum_{p,q}\left(\frac{\sum_{p',q'} W_k(p',q')\hat{G}_k(p',q')G_k(p',q')}{\sum_{p',q'} W_k(p',q')\hat{G}_k^2(p',q')}\right)W_k(p,q)\hat{G}_k(p,q)G_k(p,q)}{\sum_{p,q} W_k(p,q)G_k^2(p,q)}\right\}, \quad (2.23)$$

where the variables have been re-inserted to emphasize them. This equation can be simplified to

$$\Phi_d = 1 - \frac{1}{K}\sum_{k=1}^{K}\frac{\left[\sum_{p,q} W_k(p,q)\hat{G}_k(p,q)G_k(p,q)\right]^2}{\left[\sum_{p,q} W_k(p,q)G_k^2(p,q)\right]\left[\sum_{p,q} W_k(p,q)\hat{G}_k^2(p,q)\right]}. \quad (2.24)$$

The phase diversity algorithm now simplifies to the problem of minimizing Equation (2.24). Any suitable nonlinear optimization algorithm can be used. Traditionally, conjugate gradient algorithms have proven effective. For these algorithms to work the derivatives of the objective function with respect to the free parameters must be calculated. These derivatives can be derived analytically so that computationally-expensive numerical derivative calculations are not needed.

2.2.3 Gradient with respect to PSF Estimates

Equation (2.24) is differentiated with respect to $\hat{G}_k(p,q)$, which is a real number. Since the partial derivative of one estimate with respect to another is zero, the sum collapses. We therefore have:

$$\frac{\partial \Phi_d}{\partial \hat{G}_k(p,q)} = -\frac{1}{K}\frac{\partial}{\partial \hat{G}_k(p,q)}\left\{\frac{\sum_{p,q}\left[W_k(p,q)\hat{G}_k(p,q)G_k(p,q)\right]^2}{\sum_{p,q}\left[W_k(p,q)G_k^2(p,q)\right]\sum_{p,q}\left[W_k(p,q)\hat{G}_k^2(p,q)\right]}\right\}. \quad (2.25)$$

Now define

$$F = \sum_{p,q}\left[W_k(p,q)\hat{G}_k(p,q)G_k(p,q)\right]^2 \text{ and} \quad (2.26)$$

$$G = \sum_{p,q}\left[W_k(p,q)G_k^2(p,q)\right]\sum_{p,q}\left[W_k(p,q)\hat{G}_k^2(p,q)\right] \quad (2.27)$$

so we can write

$$\frac{\partial \Phi_d}{\partial \hat{G}_k(p,q)} = \frac{+1}{K}\frac{\frac{\partial G}{\partial \hat{G}_k(p,q)}F - \frac{\partial F}{\partial \hat{G}_k(p,q)}G}{G^2}, \quad (2.28)$$

where we have switched the sign on the quotient rule and changed the leading minus sign to a positive. We will break this equation into two parts, I and II. Equation I is:

$$I = \frac{-1}{K}\frac{\frac{\partial F}{\partial \hat{G}_k(p,q)}G}{G^2} = \frac{-1}{K}\frac{\frac{\partial F}{\partial \hat{G}_k(p,q)}}{G} \tag{2.29}$$

$$I = \frac{-1}{K}\frac{1}{\sum_{p',q'} W_k(p',q')G_k^2(p',q')\sum_{p',q'} W_k(p',q')\hat{G}_k^2(p',q')}\frac{\partial}{\partial \hat{G}_k(p,q)}\left\{\sum_{p',q'}\left[W_k(p',q')\hat{G}_k(p',q')G_k(p',q')\right]^2\right\}$$

(2.29)

$$I = \frac{-1}{K}\frac{2\left[\sum_{p',q'} W_k(p',q')\hat{G}_k(p',q')G_k(p',q')\right]W_k(p,q)G_k(p,q)}{\sum_{p',q'} W_k(p',q')G_k^2(p',q')\sum_{p',q'} W_k(p',q')\hat{G}_k^2(p',q')}. \tag{2.30}$$

We multiply the numerator and denominator by $\sum_{p',q'}\left[W_k(p',q')\hat{G}_k^2(p',q')\right]$ to get

$$I = \frac{-1}{K}\frac{2W_k(p,q)G_k(p,q)\sum_{p',q'} W_k(p',q')\hat{G}_k(p',q')G_k(p',q')\sum_{p',q'} W_k(p',q')\hat{G}_k^2(p',q')}{\sum_{p',q'} W_k(p',q')G_k^2(p',q')\left[\sum_{p',q'} W_k(p',q')\hat{G}_k^2(p',q')\right]^2}. \tag{2.31}$$

Next we deal with Equation II:

$$II = \frac{1}{K}\frac{F\frac{\partial G}{\partial \hat{G}_k(p,q)}}{G^2} \tag{2.32}$$

$$II = \frac{1}{K}\frac{\left[\sum_{p',q'} W_k(p',q')\hat{G}_k(p',q')G_k(p',q')\right]^2\sum_{p',q'} W_k(p',q')G_k^2(p',q')}{\left[\sum_{p',q'} W_k(p',q')G_k^2(p',q')\right]^2\left[\sum_{p',q'} W_k(p',q')\hat{G}_k^2(p',q')\right]^2}\frac{\partial}{\partial \hat{G}_k(p,q)}\left\{\sum_{p',q'} W_k(p',q')\hat{G}_k^2(p',q')\right\}.$$

(2.33)

The summation in the derivative term is collapsed since the derivative is with respect to a function of (p,q) rather than (p',q'). We therefore have

$$II = \frac{1}{K} \frac{\left[\sum_{p',q'} W_k(p',q') \hat{G}_k(p',q') G_k(p',q') \right]^2}{\left[\sum_{p',q'} W_k(p',q') G_k^2(p',q') \right] \left[\sum_{p',q'} W_k(p',q') \hat{G}_k^2(p',q') \right]^2} 2W_k(p,q) \hat{G}_k(p,q). \qquad (2.34)$$

The summation of Equations (2.31) and (2.34) can be written as

$$\frac{\partial \Phi_d}{\partial \hat{G}_k(p,q)} = \frac{2}{K} \frac{W_k(p,q) \left[\sum_{p',q'} W_k(p',q') \hat{G}_k(p',q') G_k(p',q') \right]}{\left[\sum_{p',q'} W_k(p',q') G_k^2(p',q') \right] \left[\sum_{p',q'} W_k(p',q') \hat{G}_k^2(p',q') \right]^2} \times \qquad (2.35)$$

$$\left\{ \hat{G}_k(p,q) \left[\sum_{p',q'} W_k(p',q') \hat{G}_k(p',q') G_k(p',q') \right] - G_k(p,q) \left[\sum_{p',q'} W_k(p',q') \hat{G}_k^2(p',q') \right] \right\}.$$

2.2.4 *Gradient with respect to Transverse Shifts*

The multi-variable chain rule states that if $z = f(x,y)$, $x = g(s,t)$, and $y = h(s,t)$, then

$$\frac{\partial z}{\partial s} = \frac{\partial z}{\partial x}\frac{\partial x}{\partial s} + \frac{\partial z}{\partial y}\frac{\partial y}{\partial s} \text{ and } \frac{\partial z}{\partial t} = \frac{\partial z}{\partial x}\frac{\partial x}{\partial t} + \frac{\partial z}{\partial y}\frac{\partial y}{\partial t}.$$

Thus we can write

$$\frac{\partial \Phi_d}{\partial \hat{p}_{s,k}} = \sum_{p',q'} \frac{\partial \Phi_d}{\partial \hat{G}_k(p',q')} \frac{\partial \hat{G}_k(p',q')}{\partial \hat{p}_{s,k}} \text{ and} \qquad (2.36)$$

$$\frac{\partial \Phi_d}{\partial \hat{q}_{s,k}} = \sum_{p',q'} \frac{\partial \Phi_d}{\partial \hat{G}_k(p',q')} \frac{\partial \hat{G}_k(p',q')}{\partial \hat{q}_{s,k}}. \qquad (2.37)$$

The calculation of $\frac{\partial \Phi_d}{\partial \hat{p}_{s,k}}$ will be shown. Using Equations (2.9), (2.11), and (2.12) gives

$$\hat{G}_k(p',q') = \frac{1}{\sqrt{MN}} \sum_{m,n} H_d(m,n) \hat{f}_k(m,n) \exp\left[-i2\pi \left(\frac{m\hat{p}_{s,k}}{M} \right) \right] \exp\left[-i2\pi \left(\frac{n\hat{q}_{s,k}}{N} \right) \right] \exp\left[+i2\pi \left(\frac{mp'}{M} + \frac{nq'}{N} \right) \right].$$

(2.37)

Thus we have

$$\frac{\partial \hat{G}_k(p',q')}{\partial \hat{p}_{s,k}} = \frac{1}{\sqrt{MN}} \sum_{m,n} \frac{-i2\pi m}{M} \hat{g}_k(m,n) \exp\left[+i2\pi \left(\frac{mp'}{M} + \frac{nq'}{N} \right) \right]. \qquad (2.38)$$

We will now put this back into the equation for $\frac{\partial \Phi_d}{\partial \hat{p}_{s,k}}$:

$$\frac{\partial \Phi_d}{\partial \hat{p}_{s,k}} = \sum_{p',q'} \frac{\partial \Phi_d}{\partial \hat{G}_k(p',q')} \frac{\partial \hat{G}_k(p',q')}{\partial \hat{p}_{s,k}} \tag{2.39}$$

$$\frac{\partial \Phi_d}{\partial \hat{p}_{s,k}} = \sum_{p',q'} \frac{\partial \Phi_d}{\partial \hat{G}_k(p',q')} \frac{1}{\sqrt{MN}} \sum_{m,n} \frac{-i2\pi m}{M} \hat{g}_k(m,n) \exp\left[+i2\pi\left(\frac{mp'}{M}+\frac{nq'}{N}\right)\right] \tag{2.40}$$

$$\frac{\partial \Phi_d}{\partial \hat{p}_{s,k}} = \sum_{m,n} \frac{-i2\pi m}{M} \hat{g}_k(m,n) \frac{1}{\sqrt{MN}} \sum_{p',q'} \frac{\partial \Phi_d}{\partial \hat{G}_k(p',q')} \exp\left[+i2\pi\left(\frac{mp'}{M}+\frac{nq'}{N}\right)\right]. \tag{2.41}$$

We now define

$$\hat{g}_k^{\dagger}(m,n) = \mathrm{DFT}\left[\frac{\partial \Phi_d}{\partial \hat{G}_k(p',q')}\right] = \frac{1}{\sqrt{MN}} \sum_{p',q'} \frac{\partial \Phi_d}{\partial \hat{G}_k(p',q')} \exp\left[+i2\pi\left(\frac{mp'}{M}+\frac{nq'}{N}\right)\right]. \tag{2.42}$$

.

This lets us write

$$\frac{\partial \Phi_d}{\partial \hat{p}_{s,k}} = \sum_{m,n} \frac{-i2\pi m}{M} \hat{g}_k(m,n) \hat{g}_k^{\dagger *}(m,n), \tag{2.43}$$

where the superscript * denotes complex conjugation. We know that $\frac{\partial \Phi_d}{\partial \hat{p}_{s,k}}$ is real since both Φ_d and $\hat{p}_{s,k}$ are real. Thus $i\hat{g}_k(m,n)\hat{g}_k^{\dagger *}(m,n)$ is real.

Next we need to prove a theorem for complex numbers. Let $z_1 = a_1 + ib_1$ and $z_2 = a_2 + ib_2$. We wish to prove that if $iz_1 z_2^* \in \mathbf{R}$ then $\mathrm{IM}\left[z_1^* z_2\right] = iz_1 z_2^*$. First we will calculate $iz_1 z_2^*$:

$$iz_1 z_2^* = i\left(a_1 + ib_1\right)\left(a_2 - ib_2\right)$$
$$iz_1 z_2^* = i\left[\left(a_1 a_2 + b_1 b_2\right) + i\left(a_2 b_1 - a_1 b_2\right)\right]$$
$$iz_1 z_2^* = \left(a_1 b_2 - a_2 b_1\right) + i\left(a_1 a_2 + b_1 b_2\right).$$

If $iz_1 z_2^* \in \mathbf{R}$ then $a_1 a_2 + b_1 b_2 = 0$ and $iz_1 z_2^* = a_1 b_2 - a_2 b_1$. Next calculate $\mathrm{IM}\left[z_1^* z_2\right]$:

$$\mathrm{IM}\left[z_1^* z_2\right] = \mathrm{IM}\left[\left(a_1 - ib_1\right)\left(a_2 + ib_2\right)\right]$$
$$\mathrm{IM}\left[z_1^* z_2\right] = \mathrm{IM}\left[\left(a_1 a_2 + b_1 b_2\right) + i\left(a_1 b_2 - a_2 b_1\right)\right]$$
$$\mathrm{IM}\left[z_1^* z_2\right] = a_1 b_2 - a_2 b_1$$
$$\mathrm{IM}\left[z_1^* z_2\right] = iz_1 z_2^* \text{ if } iz_1 z_2^* \in \mathbf{R}.$$

Using this result we can write

$$\frac{\partial \Phi_d}{\partial \hat{p}_{s,k}} = \sum_{m,n} \frac{-2\pi m}{M} \mathrm{IM}\left[\hat{g}_k^*(m,n)\hat{g}_k^{\dagger}(m,n)\right] \tag{2.44}$$

$$\frac{\partial \Phi_d}{\partial \hat{p}_{s,k}} = -\mathrm{IM}\left[\sum_{m,n} \frac{2\pi m}{M} \hat{g}_k^{\dagger}(m,n)\hat{g}_k^{*}(m,n)\right]. \tag{2.45}$$

Similarly we can write

$$\frac{\partial \Phi_d}{\partial \hat{q}_{s,k}} = -\mathrm{IM}\left[\sum_{m,n} \frac{2\pi n}{N} \hat{g}_k^{\dagger}(m,n)\hat{g}_k^{*}(m,n)\right]. \tag{2.46}$$

2.2.5 Gradient with respect to Optical Intensity Estimates

We now have accounted for the part of $\hat{G}_k$ that varies with translation of the images. Next we need to account for the variation in the intensity data itself. Again using the multivariable chain rule, we have:

$$\frac{\partial \Phi_d}{\partial \hat{I}_k(p',q')} = \sum_{p,q} \frac{\partial \Phi_d}{\partial \hat{G}_k(p,q)} \frac{\partial \hat{G}_k(p,q)}{\partial \hat{I}_k(p',q')}. \tag{2.47}$$

Inserting Equation (2.10) into Equation (2.11) lets us write

$$\hat{g}_k(m,n) = H_{s,k}(m,n)H_d(m,n)\frac{1}{\sqrt{MN}}\sum_{p,q} I_k(p,q)\exp\left[-i2\pi\left(\frac{mp}{M}+\frac{nq}{N}\right)\right] \tag{2.48}$$

and hence

$$\hat{G}_k(p,q) = \frac{1}{\sqrt{MN}}\sum_{m,n} H_d(m,n)H_{s,k}(m,n)\frac{1}{\sqrt{MN}}\sum_{p'',q''} I_k(p'',q'')\exp\left[-i2\pi\left(\frac{mp''}{M}+\frac{nq''}{N}\right)\right]\exp\left[i2\pi\left(\frac{mp}{M}+\frac{nq}{N}\right)\right]. \tag{2.49}$$

We therefore have

$$\frac{\partial \hat{G}_k(p,q)}{\partial I_k(p',q')} = \frac{1}{MN}\sum_{m,n} H_d(m,n)H_{s,k}(m,n)\exp\left[-i2\pi\left(\frac{mp'}{M}+\frac{nq'}{N}\right)\right]\exp\left[i2\pi\left(\frac{mp}{M}+\frac{nq}{N}\right)\right]. \tag{2.50}$$

Now let

$$H_k(m,n) = H_d(m,n)\hat{H}_{s,k}(m,n) \tag{2.51}$$

and

$$h_k(p,q) = \mathrm{IDFT}\left[H_d(m,n)\hat{H}_{s,k}(m,n)\right]. \tag{2.52}$$

We therefore have

$$\frac{\partial \hat{G}_k(p,q)}{\partial I_k(p',q')} = \frac{1}{\sqrt{MN}} h_k(p-p',q-q') \tag{2.53}$$

Plugging this back into the Equation (2.47) gives

$$\frac{\partial \Phi_d}{\partial \hat{I}_k(p',q')} = \sum_{p,q} \frac{\partial \Phi_d}{\partial \hat{G}_k(p,q)} \frac{1}{\sqrt{MN}} h_k(p-p',q-q'). \tag{2.54}$$

If we denote correlation with the symbol $\otimes$, we have

$$\frac{\partial \Phi_d}{\partial \hat{I}_k(p',q')} = \frac{1}{\sqrt{MN}} \frac{\partial \Phi_d}{\partial \hat{G}_k(p,q)} \otimes h_k(p-p',q-q') \ . \tag{2.55}$$

Next we use the correlation theorem $f \otimes g = \mathrm{IDFT}\left[\left\{\mathrm{DFT}[f]\right\}^* \mathrm{DFT}[g]\right]$ to write

$$\frac{\partial \Phi_d}{\partial \hat{I}_k(p',q')} = \frac{1}{\sqrt{MN}} \sum_{m,n} \hat{g}_k^{\dagger}(m,n) H_k^*(m,n) \exp\left[i2\pi\left(\frac{mp'}{M}+\frac{nq'}{N}\right)\right] \tag{2.56}$$

$$\frac{\partial \Phi_d}{\partial \hat{I}_k(p',q')} = \frac{1}{\sqrt{MN}} \sum_{m,n} \hat{g}_k^{\dagger}(m,n) H_d^*(m,n) \hat{H}_{s,k}^*(m,n) \exp\left[i2\pi\left(\frac{mp'}{M}+\frac{nq'}{N}\right)\right] \tag{2.57}$$

$$\frac{\partial \Phi_d}{\partial \hat{I}_k(p',q')} = \frac{1}{\sqrt{MN}} \sum_{m,n} \hat{g}_k^{\dagger}(m,n) H_d^*(m,n) \hat{H}_{s,k}^*(m,n) \exp\left[i2\pi\left(\frac{mp'}{M}+\frac{nq'}{N}\right)\right] \tag{2.58}$$

$$\frac{\partial \Phi_d}{\partial \hat{I}_k(p',q')} = \mathrm{IDFT}\left[\hat{f}_k^{\dagger}(m,n)\right] \tag{2.59}$$

$$\frac{\partial \Phi_d}{\partial \hat{I}_k(p',q')} = \frac{1}{\sqrt{MN}} \sum_{m,n} \hat{f}_k^{\dagger}(m,n) \exp\left[i2\pi\left(\frac{mp'}{M}+\frac{nq'}{N}\right)\right], \tag{2.60}$$

where we have defined

$$\hat{f}_k^{\dagger}(m,n) = \hat{H}_{s,k}^*(m,n) H_d^*(m,n) \hat{g}_k^{\dagger}(m,n). \tag{2.61}$$

2.2.6 Gradient with respect to Defocus Amounts

It is often useful to let the defocus amounts be optimized. This allows for compensation of any errors in the mechanism used to change the defocus. We need to go through several iterations of the chain rule to perform this analysis. We will first calculate derivatives with respect to $\hat{E}_k(m,n)$, then $\hat{U}_k(m,n)$, then $\hat{z}_k$.

Using the multivariable chain rule gives us

$$\frac{\partial \Phi_d}{\partial \hat{E}_k(p',q')} = \sum_{p,q} \frac{\partial \Phi_d}{\partial \hat{I}_k(p,q)} \frac{\partial \hat{I}_k(p,q)}{\partial \hat{E}_k(p',q')}. \tag{2.62}$$

Since $\hat{E}_k(p',q')$ is complex, we need to treat it as such in performing the derivative. We have

$$\frac{\partial \hat{I}_k(p,q)}{\partial \hat{E}_k(p',q')} = \frac{\partial \hat{I}_k(p,q)}{\partial\left\{\mathrm{RE}\left[\hat{E}_k\left(p',q'\right)\right]\right\}} + i\frac{\partial \hat{I}_k(p,q)}{\partial\left\{\mathrm{IM}\left[\hat{E}_k\left(p',q'\right)\right]\right\}} \tag{2.63}$$

where

$$\hat{I}_k(p,q) = \hat{E}_k(p,q)\hat{E}_k^*(p,q) \tag{2.64}$$

and $\mathrm{RE}[]$ denotes the operation that returns the real part of a complex value.

We calculate these terms below:

$$\frac{\partial \hat{I}_k(p,q)}{\partial\left\{\mathrm{RE}\left[\hat{E}_k\left(p',q'\right)\right]\right\}} = \frac{\partial}{\partial\left\{\mathrm{RE}\left[\hat{E}_k\left(p',q'\right)\right]\right\}}\left\{\hat{E}_k(p,q)\hat{E}_k^*(p,q)\right\} \tag{2.65}$$

$$\frac{\partial \hat{I}_k(p,q)}{\partial\left\{\mathrm{RE}\left[\hat{E}_k\left(p',q'\right)\right]\right\}} = \hat{E}_k^*(p',q') + \hat{E}_k(p',q') \tag{2.66}$$

$$\frac{\partial \hat{I}_k(p,q)}{\partial\left\{\mathrm{RE}\left[\hat{E}_k\left(p',q'\right)\right]\right\}} = 2\,\mathrm{RE}\left\{\hat{E}_k(p',q')\right\} \tag{2.67}$$

and

$$\frac{\partial \hat{I}_k(p,q)}{\partial\left\{\mathrm{IM}\left[\hat{E}_k\left(p',q'\right)\right]\right\}} = \frac{\partial}{\partial\left\{\mathrm{IM}\left[\hat{E}_k\left(p',q'\right)\right]\right\}}\left\{\hat{E}_k(p,q)\hat{E}_k^*(p,q)\right\} \tag{2.68}$$

$$\frac{\partial \hat{I}_k(p,q)}{\partial\left\{\mathrm{IM}\left[\hat{E}_k\left(p',q'\right)\right]\right\}} = i\hat{E}_k^*(p',q') - i\hat{E}_k(p',q') \tag{2.69}$$

$$\frac{\partial \hat{I}_k(p,q)}{\partial\left\{\mathrm{IM}\left[\hat{E}_k\left(p',q'\right)\right]\right\}} = -i\left[\hat{E}_k(p',q') - \hat{E}_k^*(p',q')\right] \tag{2.70}$$

$$\frac{\partial \hat{I}_k(p,q)}{\partial\left\{\mathrm{IM}\left[\hat{E}_k\left(p',q'\right)\right]\right\}} = -i\left[2i\,\mathrm{IM}\left\{\hat{E}_k(p',q'\right\}\right] \tag{2.71}$$

$$\frac{\partial \hat{I}_k(p,q)}{\partial\left\{\mathrm{IM}\left[\hat{E}_k\left(p',q'\right)\right]\right\}} = 2\,\mathrm{IM}\left\{\hat{E}_k(p',q'\right\}. \tag{2.72}$$

Thus

$$\frac{\partial \hat{I}_k(p,q)}{\partial \hat{E}_k\left(p',q'\right)} = 2\,\mathrm{RE}\left\{E_k\left(p',q'\right)\right\} + 2i\,\mathrm{IM}\left\{\hat{E}_k\left(p',q'\right)\right\} \tag{2.73}$$

$$\frac{\partial \hat{I}_k(p,q)}{\partial \hat{E}_k(p',q')} = 2\hat{E}_k(p',q'). \tag{2.74}$$

So we can write

$$\frac{\partial \Phi_d}{\partial E_k(p',q')} = \frac{\partial \Phi_d}{\partial \hat{I}_k(p,q)} 2\hat{E}_k(p',q') \tag{2.75}$$

since $\frac{\partial \hat{I}_k(p,q)}{\partial \hat{E}_k(p',q')} = 0$ for $p \neq p'$ and $q \neq q'$. If we define

$$\hat{E}_k^{\dagger}(p',q') = 2\hat{E}_k(p',q')\frac{\partial \Phi_d}{\partial \hat{I}_k(p',q')} \tag{2.76}$$

Equation (2.75) simplifies to

$$\frac{\partial \Phi_d}{\partial \hat{E}_k(p',q')} = \hat{E}_k^{\dagger}(p',q'). \tag{2.77}$$

Next we calculate

$$\frac{\partial \Phi_d}{\partial \hat{U}_k(m,n)} = \sum_{p,q} \frac{\partial \Phi_d}{\partial \hat{E}_k(p,q)} \frac{\partial \hat{E}_k(p,q)}{\partial \hat{U}_k(m,n)}. \tag{2.78}$$

Using Equation (2.6) it can be easily seen that

$$\frac{\partial \hat{E}_k(p,q)}{\partial \hat{U}_k(m,n)} = \frac{1}{\sqrt{MN}} \exp\left[+i2\pi\left(\frac{mp}{M} + \frac{nq}{N}\right)\right]. \tag{2.79}$$

So we have

$$\frac{\partial \Phi_d}{\partial \hat{U}_k(m,n)} = \sum_{p,q} \frac{\partial \Phi}{\partial \hat{E}_k(p,q)} \frac{\partial \hat{E}_k(p,q)}{\partial \hat{U}_k(m,n)} \tag{2.80}$$

$$\frac{\partial \Phi_d}{\partial \hat{U}_k(m,n)} = \frac{1}{\sqrt{MN}} \sum_{p,q} \hat{E}_k^{\dagger}(p,q) \exp\left[+i2\pi\left(\frac{mp}{M} + \frac{nq}{N}\right)\right] \tag{2.81}$$

$$\frac{\partial \Phi_d}{\partial \hat{U}_k(m,n)} = \hat{U}_k^{\dagger *}(m,n) \tag{2.82}$$

where we have defined

$$\hat{U}_k^{\dagger}(m,n) = \frac{1}{\sqrt{MN}} \sum_{p,q} \hat{E}_k^{\dagger}(p,q) \exp\left[-i2\pi\left(\frac{mp}{M} + \frac{nq}{N}\right)\right]. \tag{2.83}$$

Lastly we calculate

$$\frac{\partial \Phi_d}{\partial \hat{z}_k} = \sum_{m,n} \frac{\partial \Phi_d}{\partial \hat{U}_k(m,n)} \frac{\partial \hat{U}_k(m,n)}{\partial \hat{z}_k}. \tag{2.84}$$

Differentiating Equation (2.5) yields

$$\frac{\partial \hat{U}_k(m,n)}{\partial \hat{z}_k} = 2\pi i \hat{U}_k(m,n)\sqrt{\frac{1}{\lambda^2} - m^2\Delta_m^2 - n^2\Delta_n^2}. \tag{2.85}$$

Thus we have

$$\frac{\partial \Phi_d}{\partial z_k} = \sum_{m,n} \frac{\partial \Phi_d}{\partial \hat{U}_k(m,n)} \frac{\partial \hat{U}_k(m,n)}{\partial \hat{z}_k} \tag{2.86}$$

$$\frac{\partial \Phi_d}{\partial z_k} = \sum_{m,n} \hat{U}_k^{\dagger *}(m,n)\hat{U}_k(m,n) 2\pi i \sqrt{\frac{1}{\lambda^2} - m^2\Delta_m^2 - n^2\Delta_n^2} \tag{2.87}$$

$$\frac{\partial \Phi_d}{\partial \hat{z}_k} = \sum_{m,n} \mathrm{IM}\left\{ i2\pi \sqrt{\frac{1}{\lambda^2} - m^2\Delta_m^2 - n^2\Delta_n^2}\hat{U}_k^{\dagger}(m,n)\hat{U}_k^{*}(m,n) \right\}, \tag{2.88}$$

where we have used the fact that $\frac{\partial \Phi_d}{\partial \hat{z}_k} \in \mathbf{R}$ and our previous proof of $\mathrm{IM}\left[iz_1^* z_2 \right] = iz_1 z_2^*$ if $iz_1 z_2^* \in \mathbf{R}$.

2.2.7 *Gradient with respect to Pupil Phase*

We will once again use multiple iterations of the chain rule to perform this calculation. We will start with $\frac{\partial \Phi_d}{\partial \hat{U}_k(m,n)}$ and differentiate with respect to $\hat{U}_f(m,n)$, $\hat{E}_f(p,q)$, $\hat{E}_p(m,n)$, and finally $\hat{\phi}(m,n)$. We start with

$$\frac{\partial \Phi_d}{\partial \hat{U}_f(m',n')} = \sum_{m,n} \frac{\partial \Phi_d}{\partial \hat{U}_k(m,n)} \frac{\partial \hat{U}_k(m,n)}{\partial \hat{U}_f(m',n')} \tag{2.89}$$

and

$$\frac{\partial \hat{U}_k(m,n)}{\partial \hat{U}_f(m',n')} = \exp\left(i2\pi \hat{z}_k \sqrt{\frac{1}{\lambda^2} - m^2\Delta_m^2 - n^2\Delta_n^2} \right) \tag{2.90}$$

if $m = m'$ and $n = n'$, otherwise it is zero. Using this we can write

$$\frac{\partial \Phi_d}{\partial \hat{U}_f(m',n')} = \hat{U}_k^{\dagger *}(m,n) \exp\left(i2\pi \hat{z}_k \sqrt{\frac{1}{\lambda^2} - m^2\Delta_m^2 - n^2\Delta_n^2} \right) \tag{2.91}$$

$$\frac{\partial \Phi_d}{\partial \hat{U}_f(m',n')} = \hat{U}_f^{\dagger *}(m,n) \tag{2.92}$$

where we have defined

$$\hat{U}_f^{\dagger}(m,n) = \hat{U}_k^{\dagger}(m,n) \exp\left(-i2\pi \hat{z}_k \sqrt{\frac{1}{\lambda^2} - m^2\Delta_m^2 - n^2\Delta_n^2} \right). \tag{2.93}$$

Next we calculate

$$\frac{\partial \Phi_d}{\partial \hat{E}_f(p',q')} = \sum_{m,n} \frac{\partial \Phi_d}{\partial \hat{U}_f(m,n)} \frac{\partial \hat{U}_f(m,n)}{\partial \hat{E}_f(p',q')}. \tag{2.94}$$

Using Equation (2.4) lets us write

$$\frac{\partial \hat{U}_f(m,n)}{\partial \hat{E}_f(p',q')} = \frac{1}{\sqrt{MN}} \exp\left[-i2\pi \left(\frac{mp'}{M} + \frac{nq}{N} \right) \right] \tag{2.95}$$

where only the $p = p'$ and $q = q'$ terms are nonzero in the summation over (p,q). Thus

$$\frac{\partial \Phi_d}{\partial \hat{E}_f(p',q')} = \sum_{m,n} \hat{U}_f^{\dagger *}(m,n) \frac{1}{\sqrt{MN}} \exp\left[-i2\pi\left(\frac{mp'}{M} + \frac{nq'}{N}\right)\right] \tag{2.96}$$

$$\frac{\partial \Phi_d}{\partial \hat{E}_f(p',q')} = \hat{E}_f^{\dagger *}(p',q') \tag{2.97}$$

where we have defined

$$\hat{E}_f^{\dagger}(p',q') = \frac{1}{\sqrt{MN}} \sum_{m,n} \hat{U}_f^{\dagger}(m,n) \exp\left[+i2\pi\left(\frac{mp'}{M} + \frac{nq'}{N}\right)\right]. \tag{2.98}$$

Next we calculate

$$\frac{\partial \Phi_d}{\partial \hat{E}_p(m',n')} = \sum_{p,q} \frac{\partial \Phi_d}{\partial \hat{E}_f(p,q)} \frac{\partial \hat{E}_f(p,q)}{\partial \hat{E}_p(m',n')}. \tag{2.99}$$

Using Equation (2.2) we can write

$$\frac{\partial \hat{E}_f(p,q)}{\partial \hat{E}_p(m',n')} = \frac{1}{\sqrt{MN}} \exp\left[-i2\pi\left(\frac{m'p}{M} + \frac{n'q}{N}\right)\right]. \tag{2.100}$$

We therefore have

$$\frac{\partial \Phi_d}{\partial \hat{E}_p(m',n')} = \sum_{p,q} \frac{\partial \Phi_d}{\partial \hat{E}_f(p,q)} \frac{\partial \hat{E}_f(p,q)}{\partial \hat{E}_p(m',n')} \tag{2.101}$$

$$\frac{\partial \Phi_d}{\partial \hat{E}_p(m',n')} = \sum_{p,q} \hat{E}_f^{\dagger *}(p,q) \frac{1}{\sqrt{MN}} \exp\left[-i2\pi\left(\frac{m'p}{M} + \frac{n'q}{N}\right)\right] \tag{2.102}$$

$$\frac{\partial \Phi_d}{\partial \hat{E}_p(m',n')} = \hat{E}_p^{\dagger *}(m',n') \tag{2.103}$$

where we have defined

$$\hat{E}_p^{\dagger}(m',n') = \frac{1}{\sqrt{MN}} \sum_{p,q} \hat{E}_f^{\dagger}(p,q) \exp\left[+i2\pi\left(\frac{m'p}{M} + \frac{n'q}{N}\right)\right]. \tag{2.104}$$

Using Equation (2.1) we can calculate

$$\frac{\partial \Phi_d}{\partial \hat{\phi}(m',n')} = \frac{\partial \Phi_d}{\partial \hat{E}_p(m,n)} \frac{\partial \hat{E}_p(m,n)}{\partial \hat{\phi}(m',n')} \tag{2.105}$$

where we do not need the chain rule since $\hat{\phi}(m',n')$ is a single array (i.e., does not depend on *k*). We can write this as

$$\frac{\partial \Phi_d}{\partial \hat{\phi}(m',n')} = \frac{\partial \Phi_d}{\partial \hat{E}_p(m,n)} \frac{\partial \hat{E}_p(m,n)}{\partial \hat{\phi}(m',n')} \tag{2.106}$$

$$\frac{\partial \Phi_d}{\partial \hat{\phi}(m',n')} = \hat{E}_p^{\dagger *}(m',n') i \hat{E}_p(m',n') \tag{2.107}$$

$$\frac{\partial \Phi_d}{\partial \hat{\phi}(m',n')} = \mathrm{IM}\left\{ \hat{E}_p^{\dagger}(m',n') \hat{E}_p^{*}(m',n') \right\} \tag{2.108}$$

where we have used the fact that $\frac{\partial \Phi_d}{\partial \hat{\phi}(m',n')} \in \mathbf{R}$.

If we write $\hat{\phi}(m',n')$ using basis functions (i.e., $\hat{\phi}(m,n) = \sum_{j=1}^{J} \hat{\alpha}_j Z_j(m,n)$) we can write

$$\frac{\partial \Phi_d}{\partial \hat{\alpha}_j} = \sum_{m.n} \frac{\partial \Phi_d}{\partial \hat{E}_p(m,n)} \frac{\partial \hat{E}_p(m,n)}{\partial \hat{\alpha}_j}. \tag{2.109}$$

We have

$$\hat{E}_p(m,n) = \sum_{j=1}^{J} \hat{A}(m,n) \exp\left(i \hat{\alpha}_j Z_j(m,n) \right) \tag{2.110}$$

and thus

$$\frac{\partial \hat{E}_p(m,n)}{\partial \hat{\alpha}_j} = i Z_j(m,n) \hat{E}_p(m,n). \tag{2.111}$$

So we can write

$$\frac{\partial \Phi_d}{\partial \hat{\alpha}_j} = \sum_{m.n} \frac{\partial \Phi_d}{\partial \hat{E}_p(m,n)} \frac{\partial \hat{E}_p(m,n)}{\partial \hat{\alpha}_j} \tag{2.112}$$

$$\frac{\partial \Phi_d}{\partial \hat{\alpha}_j} = \sum_{m.n} \hat{E}_p^{\dagger *}(m,n) i Z_j(m,n) \hat{E}_p(m,n) \tag{2.113}$$

$$\frac{\partial \Phi_d}{\partial \hat{\alpha}_j} = \sum_{m.n} Z_j(m,n)\, \mathrm{IM}\left\{ \hat{E}_p^{\dagger}(m,n) \hat{E}_p^{*}(m,n) \right\} \tag{2.114}$$

where we have used the property that $\frac{\partial \Phi_d}{\partial \hat{\alpha}_j} \in \mathbf{R}$.

2.2.8 *Gradient with respect to Pupil Amplitude*

Next we calculate $\frac{\partial \Phi_d}{\partial \hat{A}(m,n)}$ using

$$\frac{\partial \Phi_d}{\partial \hat{A}(m',n')} = \frac{\partial \Phi_d}{\partial \hat{E}_p(m,n)} \frac{\partial \hat{E}_p(m,n)}{\partial \hat{A}(m',n')} \tag{2.115}$$

where we do not need the chain rule since $A(m',n')$ is a single array (i.e., does not depend on k). We have previously calculated $\frac{\partial \Phi_d}{\partial \hat{E}_p(m,n)}$. We can easily see from Equation (2.1) that

$$\frac{\partial \hat{E}_p(m,n)}{\partial \hat{A}(m',n')} = \exp\left[i\hat{\phi}(m',n') \right]$$

and thus

$$\frac{\partial \Phi_d}{\partial \hat{A}(m',n')} = \frac{\partial \Phi_d}{\partial \hat{E}_p(m,n)} \frac{\partial \hat{E}_p(m,n)}{\partial \hat{A}(m',n')} \tag{2.116}$$

$$\frac{\partial \Phi_d}{\partial \hat{A}(m',n')} = \hat{E}_p^{\dagger *}(m',n') \exp\left[i\hat{\phi}(m',n') \right], \tag{2.117}$$

where we have used Equation (2.103). We know that $\frac{\partial \Phi_d}{\partial \hat{A}(m',n')} \in \mathbf{R}$ and need one more property of complex numbers. Let $z_1 = a_1 + ib_1$ and $z_2 = a_2 + ib_2$. We wish to prove that if $z_1 z_2 \in \mathbf{R}$ then $\mathrm{RE}\left[z_1^* z_2^* \right] = z_1 z_2$. First we calculate

$$z_1 z_2 = \left(a_1 a_2 - b_1 b_2 \right) + i\left(a_1 b_2 + a_2 b_1 \right)$$
$$z_1 z_2 = \left(a_1 a_2 - b_1 b_2 \right) \text{ if } z_1 z_2 \in \mathbf{R}.$$

Next, we calculate

$$\mathrm{RE}\left[z_1^* z_2^* \right] = \mathrm{RE}\left[\left(a_1 a_2 - b_1 b_2 \right) - i\left(a_1 b_2 + a_2 b_1 \right) \right]$$
$$\mathrm{RE}\left[z_1^* z_2^* \right] = \left(a_1 a_2 - b_1 b_2 \right)$$

and we can see that the relationship is proven. Thus

$$\frac{\partial \Phi_d}{\partial \hat{A}(m',n')} = \mathrm{RE}\left[\hat{E}_p^{\dagger}(m',n') \exp\left(-i\hat{\phi}(m',n') \right) \right]. \tag{2.118}$$

2.3 Optimization

The goal of the phase retrieval algorithm is to minimize the objective function defined in Equation (2.24). As has been previously stated, a variety of algorithms have been explored for this task. The algorithm preferred in the literature is conjugate gradient minimization.

A significant portion of the community uses Matlab (a product of The Mathworks, Inc. of Natick, MA). Matlab has a variety of algorithms available in its core product and its Optimization Toolbox product, but does not include conjugate gradient algorithms among these. Custom code for the conjugate gradient algorithm was written for this project.

As part of this research effort, other optimization algorithms have been investigated as well. Two different algorithms available in Matlab's Optimization Toolbox Version 6.1 (R2011b) have been tried. These are implemented as the "medium scale" and "large scale" algorithms implemented via the function fminunc(), which performs unconstrained minimization of an

objective function. When gradient information is available – as it is for phase diversity – the medium scale algorithm is a quasi-Newton algorithm with Hessian updating via the Broyden, Fletcher, Goldfarb, and Shanno (BFGS) method.

The large scale algorithm is a trust-region method which restricts the multi-dimensional problem to a two-dimensional subspace determined via a preconditioned conjugate gradient method. This prevents the need for calculating the full Hessian matrix. Details on these algorithms are available in the Matlab Optimization Toolbox User's Guide and "Practical Methods of Optimization" by Roger Fletcher (Fletcher 1987).

The trust-region method has proven considerably more effective than conjugate gradient algorithms. It generally provides a more accurate solution in a shorter period of time. This is surprising considering work in the literature almost exclusively uses conjugate gradient methods.

Experience also indicates, though, that for the case where the phase is allowed to vary on a pixel-by-pixel basis, the conjugate gradient algorithm is superior. The algorithms implemented in the Matlab Optimization Toolbox use considerably more memory and struggle with phase maps of any significant size.

2.4 Phase Diversity Testbed

A goal of this research effort is to demonstrate that phase diversity algorithms work on real data. Much of the work in the literature focuses on simulated data. To this end a phase diversity testbed system has been built.

2.4.1 Testbed Design

The first step of development of the phase diversity testbed was to demonstrate that accurate monochromatic wavefronts could be reconstructed from measured point-spread functions. The standard method of wavefront measurement is interferometry, and thus a system was designed that allowed the wavefront to be interferometrically measured.

The interferometric configuration is shown below. A PhaseCam interferometer with a wavelength of 632.8 nm from 4D Technology is used. Light passes through an f/10 diverger and then is directed to the test lens.

The test lens is an achromat from Edmund Optics (part NT45-271). The test lens is placed immediately behind an iris with a diameter of 1.641 inches. The image space f/number (the ratio of the focal length to the beam diameter) is 15.8.

After the test lens light is directed to a Zygo reference sphere with a numerical aperture (NA) of 0.68. The Zygo reference sphere is a concave mirror that returns light back on itself so that it passes through the optical system a second time and then returns to the interferometer.

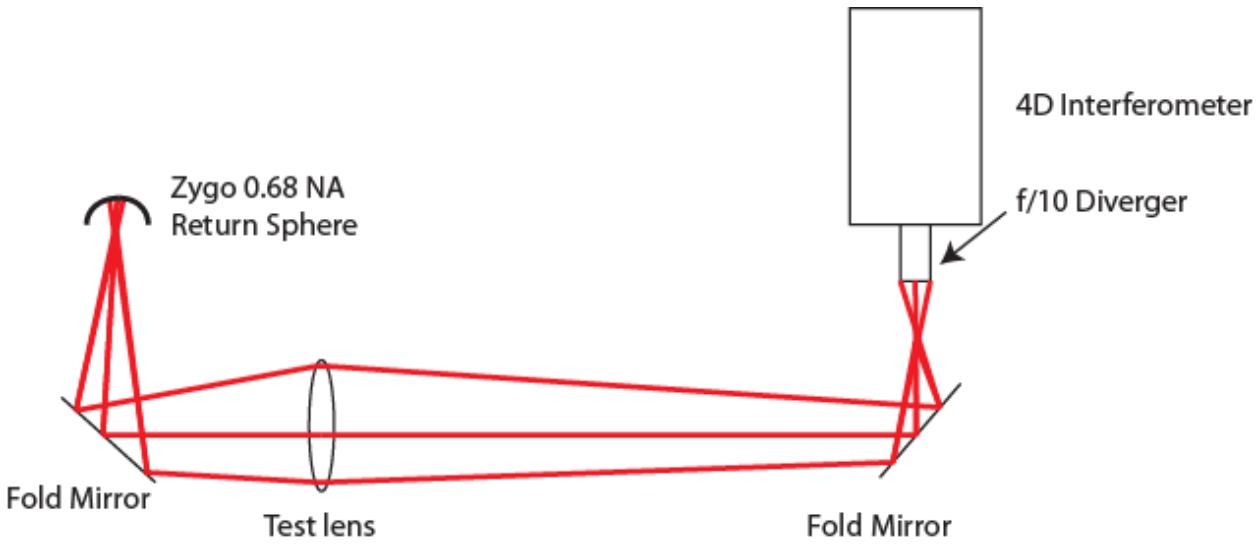

Figure 1: Monochromatic Testbed in the Interferometric Configuration

Note that the tip and tilt of the test lens can be adjusted to change the wavefront error.

The system is then modified for the phase diversity configuration. First a 10 micron diameter pinhole is aligned to the interferometric beam. This ensures that the field angle of the beam is the same for both configurations. Next a ground glass diffuser (on a substrate of ultraviolet-grade fused silica) is inserted between the diverger and the pinhole. This ensures that test lens is uniformly illuminated and destroys any effects that might arise because of the spatial coherence of the laser beam. Lastly, the return sphere is replaced with an Allied Vision Technologies (AVT) Stingray F-504 camera. This is a 12-bit 2/3" progressive scan CCD camera with a sensing area of 8.5 x 7.1 millimeters, a resolution of 2456x2058 pixels, and a pixel size of 3.45x3.45 microns. The following figure shows the testbed in the phase diversity configuration.

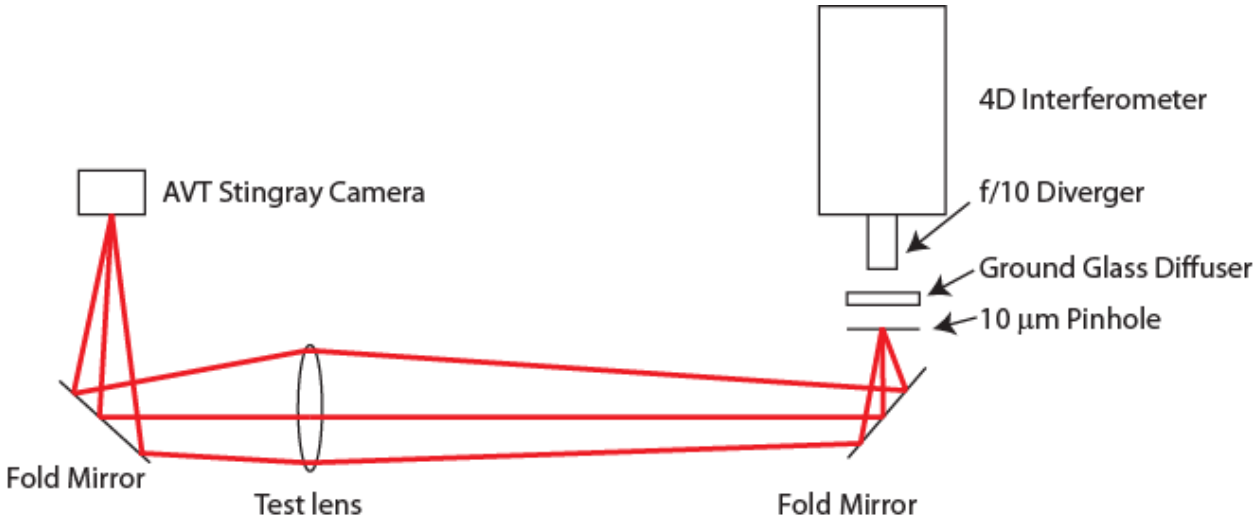

Figure 2: Monochromatic Testbed in the Phase Diversity Configuration

The AVT camera is placed on a translation stage that allows it to be moved along the optical axis. Matlab code was written to control this translation stage, the camera, and a shutter placed between the pinhole and the first fold mirror.

Care must be taken to fully understand the coordinate systems of the two configurations. In the interferometric configuration the wavefront is sensed from the source side of the test lens while in the phase diversity configuration it is sensed from the opposite side. This induces an effective flipping of the wavefront (i.e., multiplication of the wavefront phase by -1). The lateral coordinates must be fully understood and corrected for the alignment of the camera and the interferometric detector.

The camera response was characterized by illuminating it with a uniform source. The camera was placed in the exit port of an 8 inch integrating sphere with a 4 inch exit port. A quartz-tungsten-halogen (QTH) source was used to illuminate the integrating sphere. Spatial variations of the pixel gains could thus be measured. These variations are assumed to be independent of integration time.

2.4.2 Interferometric Measurements

Four different wavefronts were tested with each of three different optimization algorithms. Note that a radial ringing pattern appears in the interferometrically-measured wavefronts. This radial ringing is an artifact of the interferometric measurement process. The test lens is uncoated and produces multiple reflections that give this weak, secondary interference pattern.

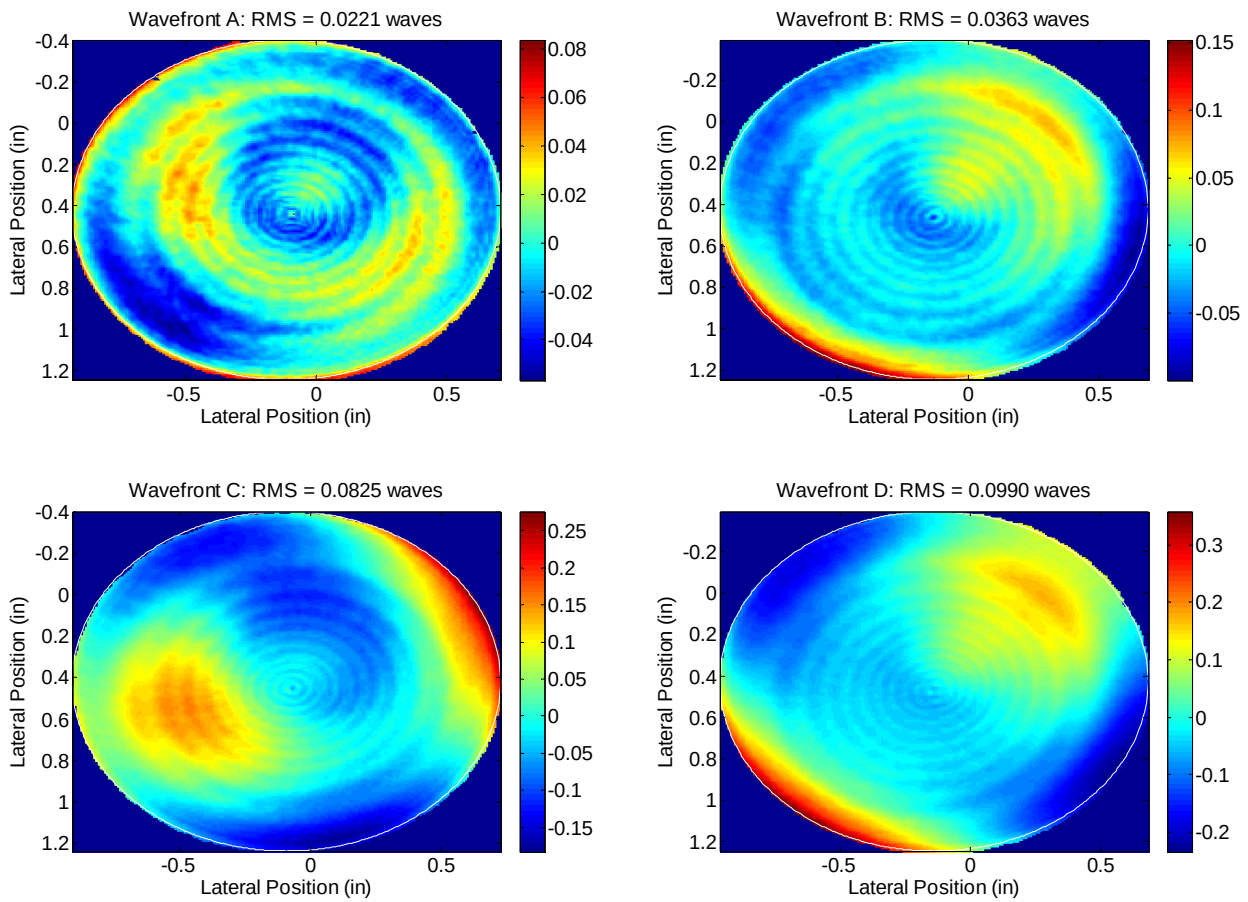

Figure 3: Interferometrically-Measured Wavefronts Analyzed for Monochromatic PDPR

The ringing visible in the wavefronts in Figure 3 above makes visually comparing the wavefronts difficult. The following figure shows the interferometrically-measured wavefronts decomposed to the same Zernike coefficients used for the phase diversity reconstructions. This tends to remove high-spatial-frequency noise from the measured wavefronts as the wavefronts are not expected to have significant energy in higher order Zernike terms. These wavefronts are shown below, again using the same color ranges as Figure 3.

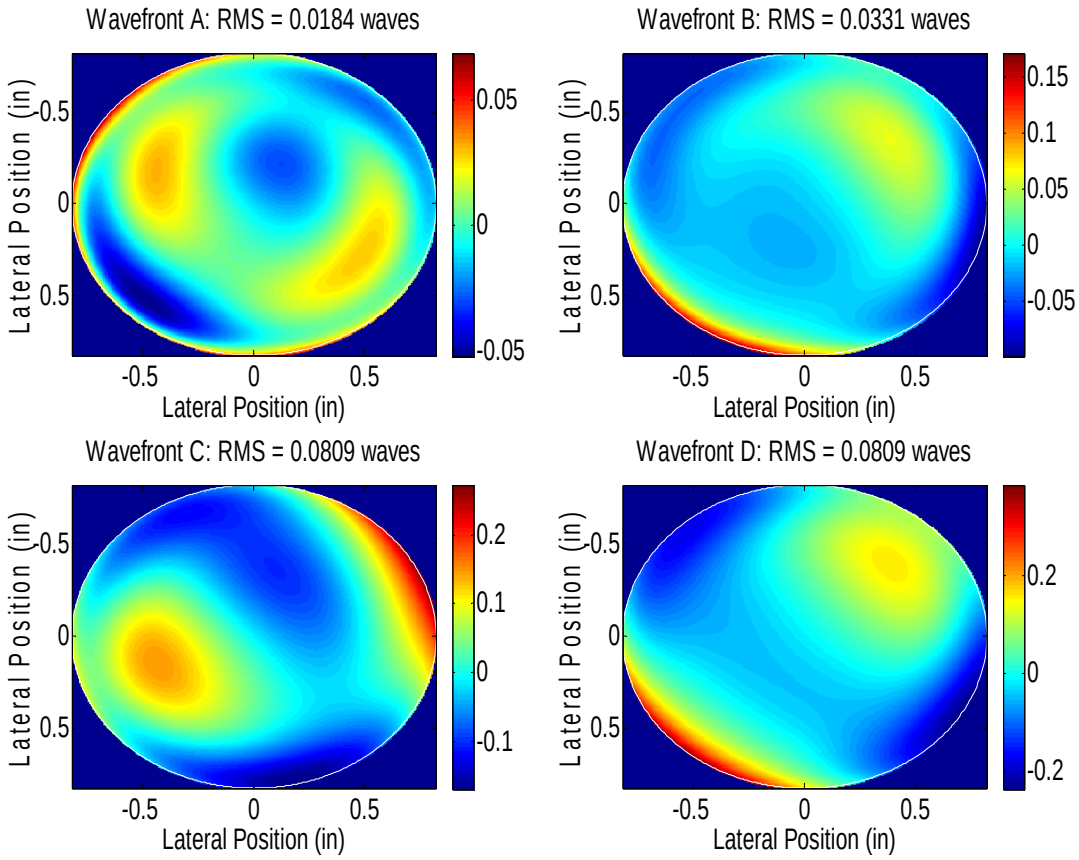

Figure 4: Interferometrically-Measured Wavefronts Decomposed to 37 Zernike Terms

2.4.3 Phase Diversity Reconstructions

After each interferometric measurement of a wavefront was performed, the testbed configuration was changed to the phase diversity configuration. Data were collected at variety of defocus depths. The camera integration time at each defocus depth was set to provide a peak signal level of about 80% of the full well capacity. Also, a number of frames were collected at each defocus depth with the shutter closed. These frames were averaged and used to perform background subtraction.

For the analyses shown below, data at the estimated best focus depth as well as one millimeter on either side of this were used. At a defocus depth of 1 mm, the standard Z4 defocus Zernike term has a magnitude of 0.228. Gain correction was used.

Each algorithm was allowed to initially run for five minutes. Standard Zernike terms Z5-Z15 were calculated. The optimization was carried out iteratively in the following steps:

1. Optimize lateral and axial shifts only
2. Optimize Zernike coefficients only
3. Optimize Zernike coefficients, lateral shifts, and axial shifts jointly

After five minutes of iterating in this manner, another five minute run was performed. During this run standard Zernikes Z5-Z37 were calculated. The optimization was performed iteratively in the same manner.

The RMS wavefront errors of the reconstructed wavefronts as well as the final objective function values, as calculated by Equation (2.13), are reported for each case. Results are shown in the table below, along with the measured RMS wavefront errors from the interferometric test.

Wavefront	Interferometry	Conjugate Gradient		Quasi-Newton		Trust-Region	
	RMS	RMS	Objective Function Value	RMS	Objective Function Value	RMS	Objective Function Value
A	0.0221	0.0590	0.03365	0.2064	0.05181	0.0271	0.02347
B	0.0363	0.0458	0.008938	0.0908	0.0223	0.0390	0.004221
C	0.0825	0.0822	0.01118	0.3390	0.03983	0.0853	0.009151
D	0.0990	0.1473	0.03945	0.2192	0.0407	0.1175	0.01548

Table 1: Comparison of Monochromatic Reconstruction Results

This table demonstrates that the trust-region algorithm seems to be superior to the others for phase diversity calculations. In fact, the quasi-Newton method never provided an adequate result.

The following figures show the reconstructed wavefronts using the different optimization methods. Note that the color scalings used for these plots are the same as are used in Figure 3 above.

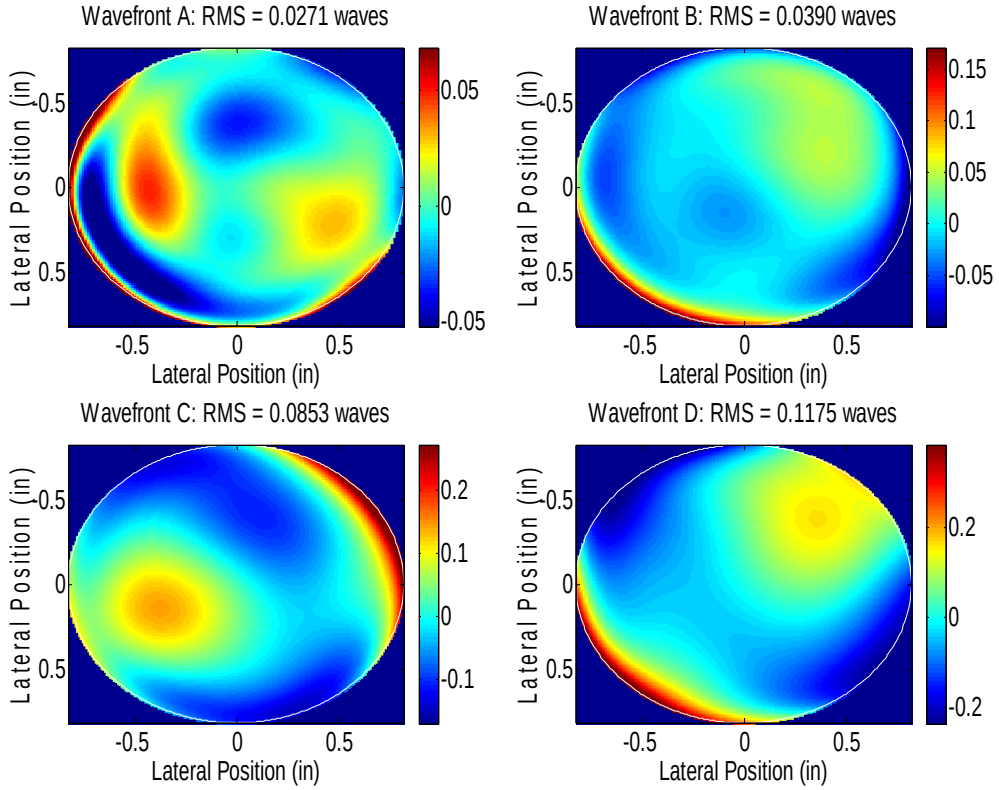

Figure 5: Wavefront Reconstructions Using the Trust-Region Algorithm

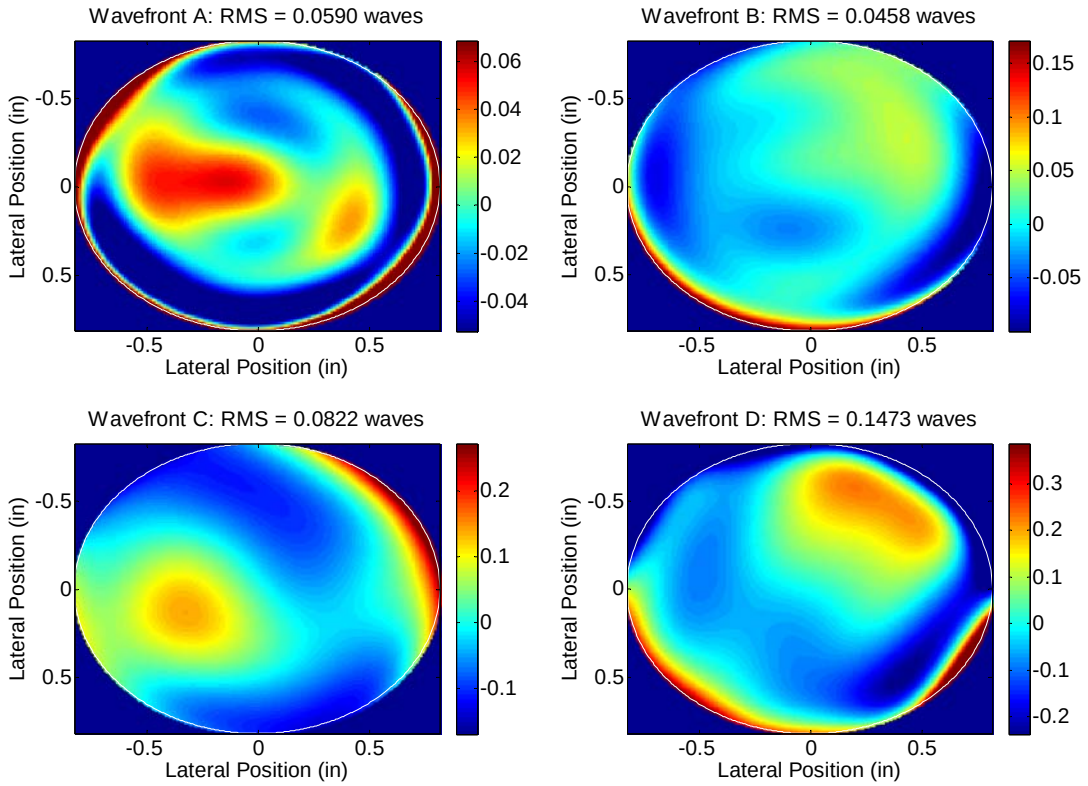

Figure 6: Wavefront Reconstructions Using the Conjugate Gradient Algorithm

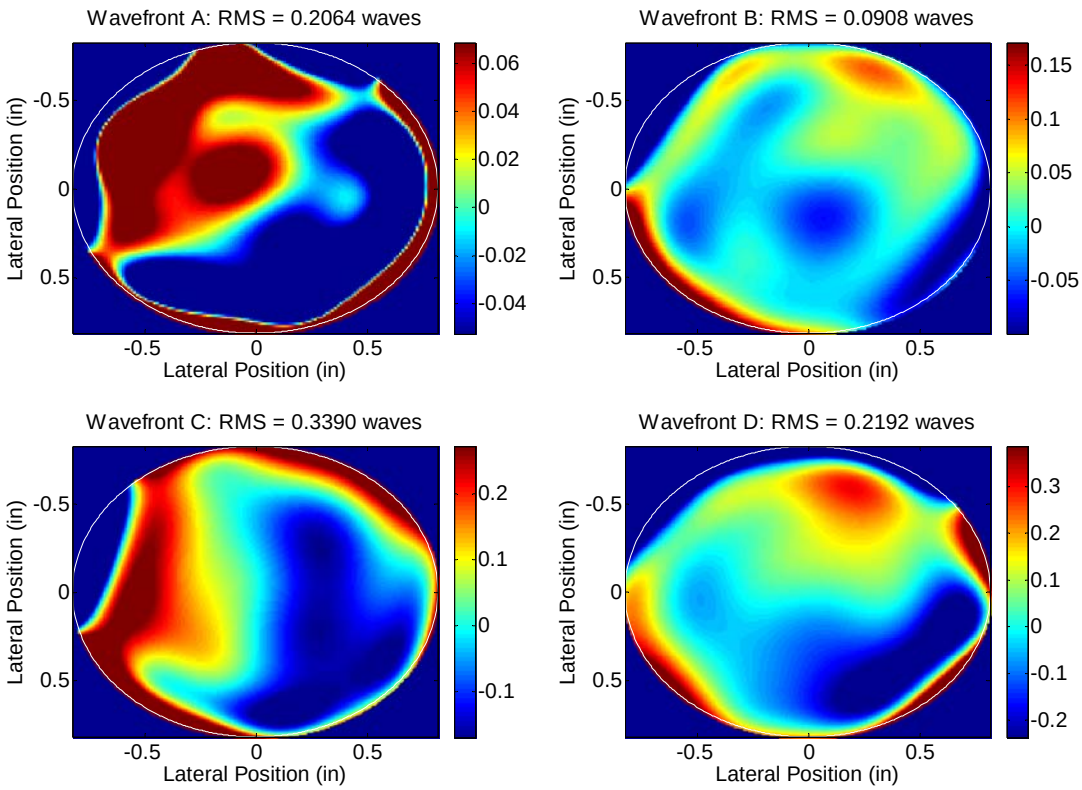

Figure 7: Wavefront Reconstructions Using the Quasi-Newton Algorithm

Another way of assessing the accuracy of the wavefront reconstructions is to compare the individual Zernike terms. The following table shows the Zernike coefficients calculated from the interferometrically-measured wavefronts and from the phase diversity reconstructions. Note that Zernike coefficients are expressed in waves.

Term	Interferometric Measurement	Trust-Region PD Reconstruction	Difference
Z5	0.0117	0.0102	0.0015
Z6	0.0010	0.0059	-0.0050
Z7	-0.0034	-0.0035	0.0002
Z8	0.0012	-0.0006	0.0018
Z9	-0.0024	-0.0017	-0.0007
Z10	-0.0008	-0.0005	-0.0004
Z11	-0.0031	0.0030	-0.0061
Z12	-0.0047	-0.0060	0.0013
Z13	-0.0032	-0.0024	-0.0008
Z14	0.0010	-0.0024	0.0034
Z15	-0.0003	0.0011	-0.0014

Table 2: Zernike Coefficients for Wavefront A

Term	Interferometric Measurement	Trust-Region PD Reconstruction	Difference
Z5	-0.0179	-0.0192	0.0013
Z6	-0.0102	-0.0123	0.0021
Z7	0.0136	0.0142	-0.0006
Z8	-0.0154	-0.0179	0.0025
Z9	-0.0021	-0.0048	0.0027
Z10	-0.0003	-0.0005	0.0002
Z11	-0.0042	0.0001	-0.0043
Z12	-0.0060	-0.0053	-0.0007
Z13	-0.0028	-0.0045	0.0017
Z14	-0.0007	-0.0002	-0.0005
Z15	0.0008	0.0005	0.0003

Table 3: Zernike Coefficients for Wavefront B

Term	Interferometric Measurement	Trust-Region PD Reconstruction	Difference
Z5	-0.0345	-0.0375	0.0030
Z6	0.0491	0.0467	0.0023
Z7	-0.0318	-0.0301	-0.0016
Z8	0.0380	0.0424	-0.0044
Z9	-0.0018	-0.0042	0.0025
Z10	-0.0010	-0.0027	0.0016
Z11	-0.0018	0.0149	-0.0167
Z12	-0.0048	-0.0024	-0.0024
Z13	-0.0034	-0.0098	0.0065
Z14	0.0004	0.0010	-0.0006
Z15	0.0004	-0.0001	0.0005

Table 4: Zernike Coefficients for Wavefront C

Term	Interferometric Measurement	Trust-Region PD Reconstruction	Difference
Z5	-0.0810	-0.0958	0.0148
Z6	-0.0176	-0.0176	-0.0001
Z7	0.0294	0.0380	-0.0087
Z8	-0.0338	-0.0372	0.0034
Z9	-0.0027	-0.0019	-0.0007
Z10	-0.0007	-0.0044	0.0037
Z11	-0.0026	0.0106	-0.0131
Z12	-0.0051	0.0003	-0.0054
Z13	-0.0037	-0.0075	0.0038
Z14	0.0001	-0.0005	0.0006
Z15	0.0000	-0.0014	0.0015

Table 5: Zernike Coefficients for Wavefront D

Thus far we have compared the quality of the reconstruction by comparing the reconstructed wavefront to the interferometrically-measured wavefront. However, in general the interferometrically-measured wavefront is not available. In that case it is useful to compare the reconstructed point-source images with the measurements. This is done in the following figures. These figures show the reconstructed PSFs for each optimization algorithm and for each wavefront. The objective function value Φ_D is shown for each PSF as well.

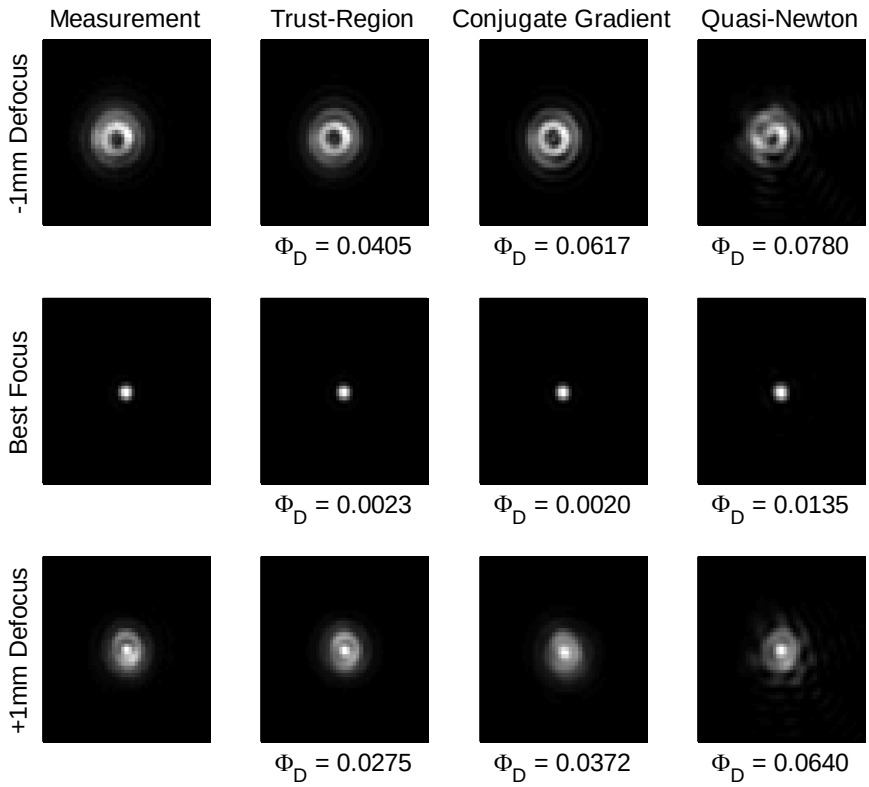

Figure 8: Measured and Reconstructed PSFs for Wavefront A

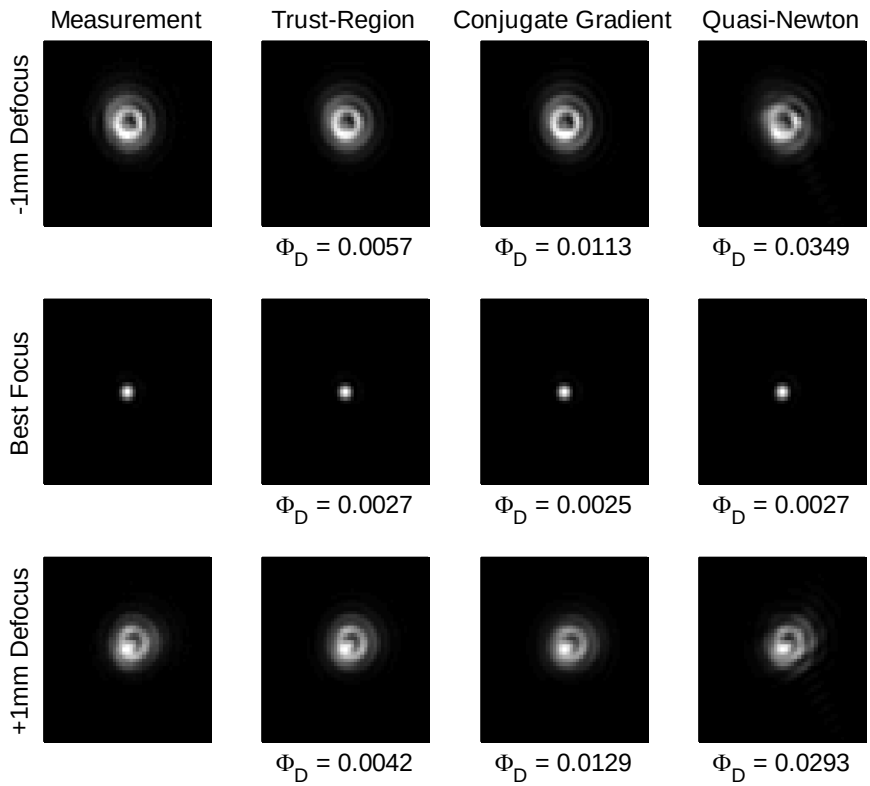

Figure 9: Measured and Reconstructed PSFs for Wavefront B

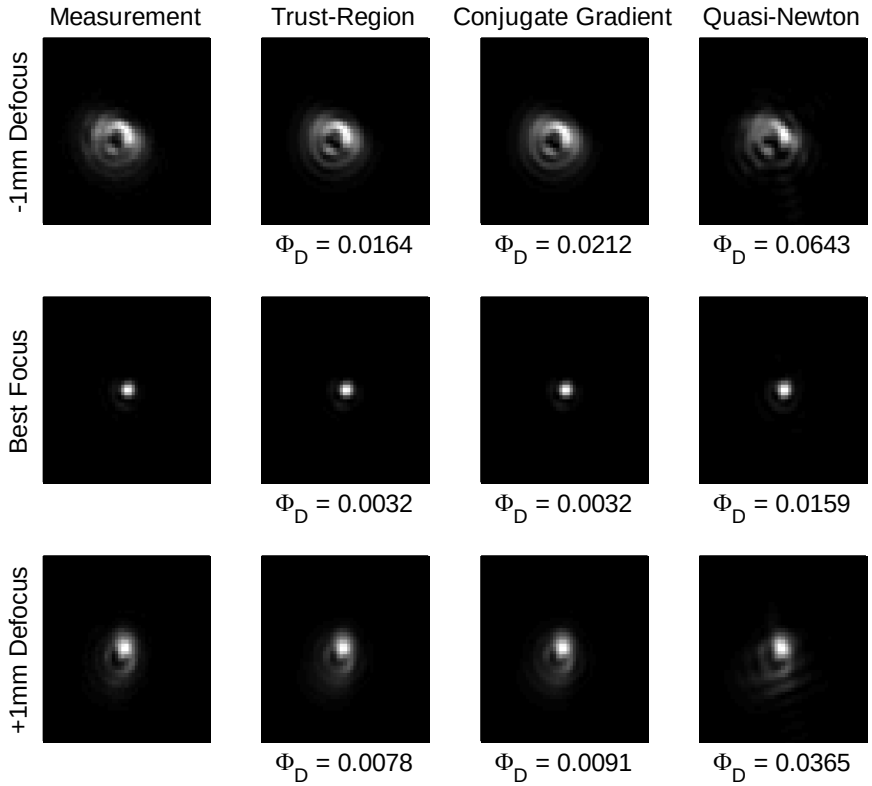

Figure 10: Measured and Reconstructed PSFs for Wavefront C

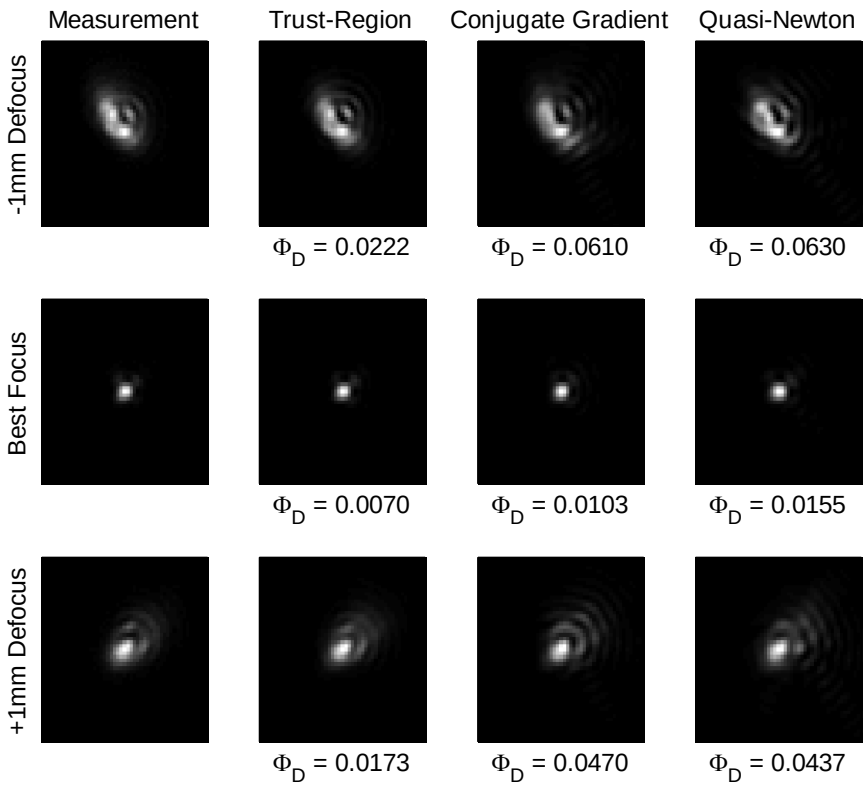

Figure 11: Measured and Reconstructed PSFs for Wavefront D

Another way of checking the fidelity of the reconstructed wavefront is to compare reconstructed PSFs at defocus depths that were not used in the optimization against measurements. This method assumes that data at more defocus depths are available.

The following figure shows the results of this analysis for Wavefront D. The lateral and axial shifts were interpolated to assume linear behavior across the full defocus range used in the optimization. This enforces a linear variation in both lateral motion and defocus. The objective function value is calculated for a single frame of data at each of the 21 defocus depths measured.

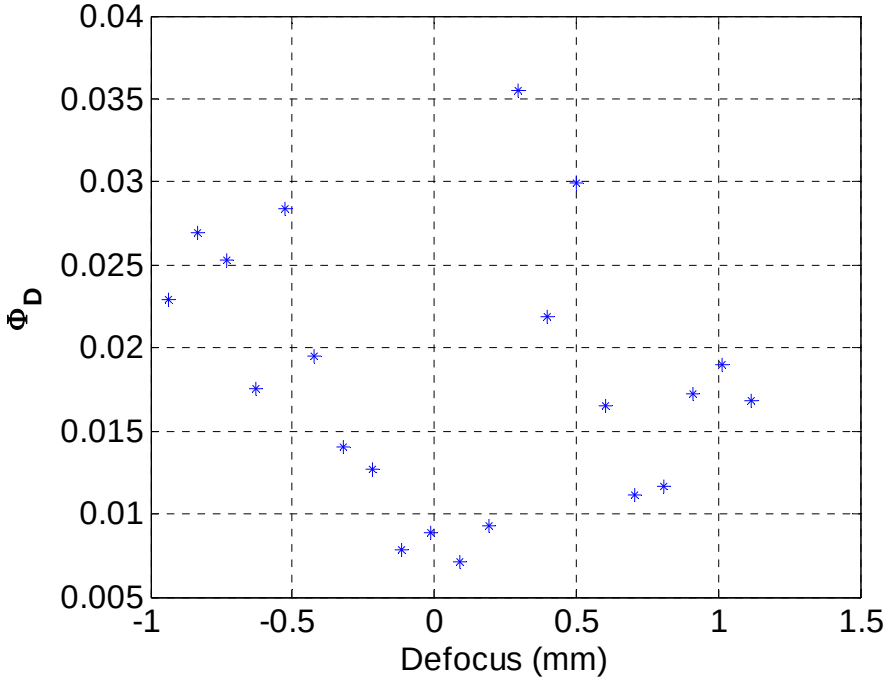

Figure 12: Objective Function Values vs. Defocus with Linear Transverse PSF Motion

This plot demonstrates that the reconstructed PSFs at defocus depths not included in the optimization also agree well with measurements. This provides further confidence that the solution accurately represents the system.

At this point in the analysis it may also be valid to optimize the lateral shifts to avoid imposing the linear constraint describe above. Random jitter may be present in the system due to vibration. The following plot shows the objective function values after lateral shifts only have been optimized. Note that the scale of this figure matches that of Figure 12.

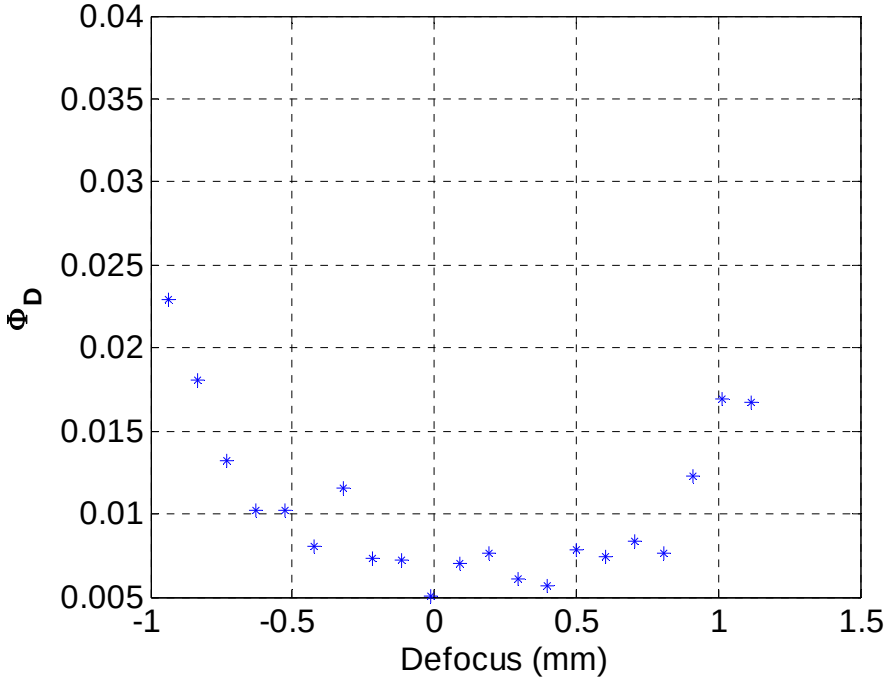

Figure 13: Objective Function Values versus Defocus after Optimizing Lateral Shifts

Figure 13 shows that much of the residuals errors shown in Figure 12 are due to jitter in the system and that the reconstructed wavefront accurately represents the system.

The monochromatic data collected with interferometer as the source clearly indicate that retrieval of the wavefront from measured point-spread functions is practical. The accuracy of the reconstruction does depend on how the optimization is performed. The trust-region algorithm included in Matlab's Optimization Toolbox seems superior. It is possible the quasi-Newton and conjugate gradient algorithms could provide better solutions if given more time.

By analyzing the value of the objective function as well as comparing the reconstructed PSFs to the measurements, a judgment of the quality of the reconstruction can be made independent of the availability of interferometrically-measured wavefronts.

3 BROADBAND PHASE-DIVERSE PHASE RETRIEVAL

The broadband theory presented here builds on the theory presented in Section 2.2 above. The theory is extended to consider the case of performing through-focus PSF measurements of a broadband source. The source is considered to be composed of a number of discrete wavelengths.

3.1 Variable Definitions

Addition variables to those presented in Section 2.1 above will be defined to handle the broadband case. These variables are presented here.

L: The total number of discrete wavelengths modeled

$l = 1, 2, ..., L$: An index over discrete wavelengths

S_l: The spectral weight of the system at wavelength l

M_l: The number of data points along transverse dimension 1 for wavelength l

N_l: The number of data points along transverse dimension 2 for wavelength l

λ_0: The reference wavelength

λ_l: The value of the lth wavelength

$\hat{\phi}_0(m,n)$: The estimated phase at the reference wavelength λ_0

$\hat{\phi}_l(m,n)$: The estimated phase at wavelength λ_l

3.2 Mathematical Theory

The mathematical theory is similar to that presented in Section 2.2. Below we show how to handle modeling the system at different discrete wavelengths.

3.2.1 Optical Model

We begin by modeling the broadband system as L discrete wavelengths. We define one of these wavelengths to be the reference wavelength and denote this wavelength by λ_0. We can then write the estimated optical field at the pupil plane as

$$\hat{E}_{p,l}(m,n) = \hat{A}(m,n)\exp\left\{ i\frac{\lambda_0}{\lambda_l}\hat{\phi}_l(m,n) \right\}. \tag{3.1}$$

For each wavelength we size the arrays so that the following equations hold (J. R. Fienup 1999):

$$\frac{1}{M_l} = \frac{1}{M}\frac{\lambda_0}{\lambda_l} \tag{3.2}$$

$$\frac{1}{N_l} = \frac{1}{N}\frac{\lambda_0}{\lambda_l}. \tag{3.3}$$

Matrices are truncated or zero-padded as necessary to make these equations hold. To keep M, N, M_l, and N_l equal to integers, the values of the wavelengths must either be carefully selected or adjusted slightly from desired values.

We can then calculate the estimated optical field at the nominal focal plane of the imaging system. We again use the discrete Fourier transform to get

$$\hat{E}_{f,l}\left(p,q\right)=\frac{1}{\sqrt{M_l N_l}}\frac{\lambda_0}{\lambda_l}\exp\left[\frac{i\pi}{\lambda_l f}\left(p^2\Delta_p^2+q^2\Delta_q^2\right)\right]\sum_{m,n}^{M_l,N_l}\hat{E}_{p,l}(m,n)\exp\left[-i2\pi\left(\frac{mp}{M_l}+\frac{nq}{N_l}\right)\right], \quad (3.4)$$

where we have again assumed that the pupil plane is at the lens plane.

We calculate the angular plane-wave spectrum at the focal plane using the discrete Fourier transform, obtaining

$$\hat{U}_{f,l}(m,n)=\frac{1}{\sqrt{M_l N_l}}\sum_{p,q}^{M_l,N_l}\hat{E}_{f,l}\left(p,q\right)\exp\left[-i2\pi\left(\frac{mp}{M_l}+\frac{nq}{N_l}\right)\right]. \quad (3.5)$$

Multiplying this by the free space transfer function provides the angular plane-wave spectrum at the *k*th defocus plane. We therefore have

$$\hat{U}_{k,l}(m,n)=\hat{U}_{f,l}(m,n)\exp\left[i2\pi\hat{z}_k\sqrt{\frac{1}{\lambda_l^{\,2}}-m^2\Delta_m^2-n^2\Delta_n^2}\right], \quad (3.6)$$

where we have again neglected constant phase terms that do not affect the measured point-spread function. We use the inverse discrete Fourier transform to calculate the optical field at the *k*th defocus plane, obtaining

$$\hat{E}_{k,l}(p,q)=\frac{1}{\sqrt{M_l N_l}}\sum_{m,n}^{M_l,N_l}\hat{U}_{k,l}(m,n)\exp\left[+i2\pi\left(\frac{mp}{M_l}+\frac{nq}{N_l}\right)\right]. \quad (3.7)$$

We now again assume a square-law detector to calculate the intensity at the *k*th defocus plane. However, we now must also incoherently sum intensities across the wavelengths. We therefore obtain the following estimated intensity at the *k*th defocus plane:

$$\hat{I}_k\left(p,q\right)=\frac{1}{L}\sum_{l=1}^{L}S_l\left|\hat{E}_{k,l}(p,q)\right|^2, \quad (3.8)$$

where S_l is used to represent spectral weights.

Equations (2.10), (2.11), and (2.12) then hold as well using this broadband definition of $\hat{I}_k\left(p,q\right)$.

3.2.2 Objective Function

We begin by considering the error metric presented in Equation (2.24). The objective function depends on the weighting functions $W_k\left(p,q\right)$, the measured point-spread functions $G_k\left(p,q\right)$,

and the estimated point-spread function $\hat{G}_k(p,q)$. Of these terms, only $\hat{G}_k(p,q)$ depends on wavelength.

3.2.3 Unchanged Gradients

The gradients calculated in Section 2 with respect to PSF estimates, transverse shifts, and optical intensity estimates are valid in the broadband case as well, provided that the broadband simulation methodology described in Section 3.2.1 is employed.

3.2.4 Gradient with respect to Defocus Amounts

We follow the same methodology as Section 2.2.6, using iterations of the multivariable chain rule to perform the analysis. Derivatives are calculated with respect to $\hat{E}_{k,l}(m,n)$, then $\hat{U}_{k,l}(m,n)$, then $\hat{z}_k$.

We start the chain rule with

$$\frac{\partial \Phi_d}{\partial \hat{E}_{k,l}(p',q')} = \sum_{p,q} \frac{\partial \Phi_d}{\partial \hat{I}_k(p,q)} \frac{\partial \hat{I}_k(p,q)}{\partial \hat{E}_{k,l}(p',q')}. \tag{3.9}$$

We already have $\frac{\partial \Phi_d}{\partial \hat{I}_k(p,q)}$ from Equation (2.60). We therefore need to calculate $\frac{\partial \hat{I}_k(p,q)}{\partial \hat{E}_{k,l}(p',q')}$.

We start with

$$\frac{\partial \hat{I}_k(p,q)}{\partial \hat{E}_{k,l}(p',q')} = \frac{\partial \hat{I}_k(p,q)}{\partial \left\{ \mathrm{RE}\left[\hat{E}_{k,l}(p',q') \right] \right\}} + i \frac{\partial \hat{I}_k(p,q)}{\partial \left\{ \mathrm{IM}\left[\hat{E}_{k,l}(p',q') \right] \right\}} \tag{3.10}$$

and

$$\hat{I}_k(p,q) = \frac{1}{L} \sum_{l=1}^{L} S_l \left| \hat{E}_{k,l}(p,q) \right|^2 = \frac{1}{L} \sum_{l=1}^{L} S_l \hat{E}_{k,l}(p,q) \hat{E}^*_{k,l}(p,q). \tag{3.11}$$

We calculate these terms below:

$$\frac{\partial \hat{I}_k(p,q)}{\partial \left\{ \mathrm{RE}\left[\hat{E}_{k,l}(p',q') \right] \right\}} = \frac{\partial}{\partial \left\{ \mathrm{RE}\left[\hat{E}_{k,l}(p',q') \right] \right\}} \left\{ \frac{1}{L} \sum_{l=1}^{L} S_l \hat{E}_{k,l}(p,q) \hat{E}^*_{k,l}(p,q) \right\} \tag{3.12}$$

$$\frac{\partial \hat{I}_k(p,q)}{\partial \left\{ \mathrm{RE}\left[\hat{E}_{k,l}(p',q') \right] \right\}} = \frac{S_l}{L} \left[\hat{E}_{k,l}(p,q) + \hat{E}^*_{k,l}(p,q) \right] \tag{3.13}$$

$$\frac{\partial \hat{I}_k(p,q)}{\partial \left\{ \mathrm{RE}\left[\hat{E}_{k,l}(p',q') \right] \right\}} = \frac{2S_l}{L} \mathrm{RE}\left\{ E_{k,l}(p',q') \right\} \tag{3.13}$$

$$\frac{\partial \hat{I}_k(p,q)}{\partial\left\{\mathrm{IM}\left[\hat{E}_{k,l}\left(p',q'\right)\right]\right\}} = \frac{\partial}{\partial\left\{\mathrm{IM}\left[\hat{E}_{k,l}\left(p',q'\right)\right]\right\}}\left\{\frac{1}{L}\sum_{l=1}^{L} S_l \hat{E}_{k,l}\left(p,q\right)\hat{E}^*_{k,l}\left(p,q\right)\right\} \tag{3.14}$$

$$\frac{\partial \hat{I}_k(p,q)}{\partial\left\{\mathrm{IM}\left[\hat{E}_{k,l}\left(p',q'\right)\right]\right\}} = \frac{S_l}{L}\left[i\hat{E}^*_{k,l}\left(p',q'\right) - i\hat{E}_{k,l}\left(p',q'\right)\right] \tag{3.15}$$

$$\frac{\partial \hat{I}_k(p,q)}{\partial\left\{\mathrm{IM}\left[\hat{E}_{k,l}\left(p',q'\right)\right]\right\}} = \frac{-iS_l}{L}\left[\hat{E}_{k,l}\left(p',q'\right) - \hat{E}^*_{k,l}\left(p',q'\right)\right] \tag{3.16}$$

$$\frac{\partial \hat{I}_k(p,q)}{\partial\left\{\mathrm{IM}\left[\hat{E}_{k,l}\left(p',q'\right)\right]\right\}} = \frac{-iS_l}{L}\left[2i\,\mathrm{IM}\left\{\hat{E}_{k,l}\left(p',q'\right)\right\}\right] \tag{3.17}$$

$$\frac{\partial \hat{I}_k(p,q)}{\partial\left\{\mathrm{IM}\left[\hat{E}_{k,l}\left(p',q'\right)\right]\right\}} = \frac{2S_l}{L}\mathrm{IM}\left[\hat{E}_{k,l}\left(p',q'\right)\right]. \tag{3.18}$$

Using Equations (3.10), (3.13), and (3.18) lets us write

$$\frac{\partial \hat{I}_k(p,q)}{\partial \hat{E}_{k,l}(p',q')} = \frac{2S_l}{L}\mathrm{RE}\left\{E_{k,l}\left(p',q'\right)\right\} + i\frac{2S_l}{L}\mathrm{IM}\left[\hat{E}_{k,l}\left(p',q'\right)\right] \tag{3.19}$$

$$\frac{\partial \hat{I}_k(p,q)}{\partial \hat{E}_{k,l}(p',q')} = \frac{2S_l}{L}\hat{E}_{k,l}\left(p',q'\right). \tag{3.20}$$

Using Equations (3.9), (2.60), and (3.20) lets us write

$$\frac{\partial \Phi_d}{\partial \hat{E}_{k,l}(p',q')} = \frac{2S_l}{L}\hat{E}_{k,l}\left(p',q'\right)\frac{1}{\sqrt{MN}}\sum_{m,n}\hat{f}^{\dagger}_k(m,n)\exp\left[i2\pi\left(\frac{mp'}{M}+\frac{nq'}{N}\right)\right]. \tag{3.21}$$

In a manner similar to Equation (2.76) and (2.77) we define

$$\hat{E}^{\dagger}_{k,l}\left(p',q'\right) = \frac{2S_l}{L}\hat{E}_{k,l}\left(p',q'\right)\frac{\partial \Phi_d}{\partial \hat{I}_k(p',q')} \tag{3.22}$$

so that we can write

$$\frac{\partial \Phi_d}{\partial \hat{E}_{k,l}(p',q')} = \hat{E}^{\dagger}_{k,l}\left(p',q'\right). \tag{3.23}$$

Next we calculate

$$\frac{\partial \Phi_d}{\partial \hat{U}_{k,l}(m,n)} = \sum_{p,q} \frac{\partial \Phi_d}{\partial \hat{E}_{k,l}(p,q)} \frac{\partial \hat{E}_{k,l}(p,q)}{\partial \hat{U}_{k,l}(m,n)}. \tag{3.24}$$

Using Equation (3.7) it can be seen that

$$\frac{\partial \hat{E}_{k,l}(p,q)}{\partial \hat{U}_{k,l}(m,n)} = \frac{1}{\sqrt{M_l N_l}} \exp\left[+i2\pi\left(\frac{mp}{M_l} + \frac{nq}{N_l}\right)\right]. \tag{3.25}$$

Inserting Equations (3.23) and (3.25) into Equation (3.24) results in

$$\frac{\partial \Phi_d}{\partial \hat{U}_{k,l}(m,n)} = \frac{1}{\sqrt{M_l N_l}} \sum_{p,q} \hat{E}^{\dagger}_{k,l}(p,q) \exp\left[+i2\pi\left(\frac{mp}{M_l} + \frac{nq}{N_l}\right)\right] \tag{3.26}$$

$$\frac{\partial \Phi_d}{\partial \hat{U}_{k,l}(m,n)} = \hat{U}^{\dagger *}_{k,l}(m,n) \tag{3.27}$$

where we have defined

$$\hat{U}^{\dagger}_{k,l}(m,n) = \frac{1}{\sqrt{M_l N_l}} \sum_{p,q} \hat{E}^{\dagger}_{k,l}(p,q) \exp\left[-i2\pi\left(\frac{mp}{M_l} + \frac{nq}{N_l}\right)\right]. \tag{3.28}$$

We now calculate

$$\frac{\partial \Phi_d}{\partial \hat{z}_k} = \sum_{m,n} \frac{\partial \Phi_d}{\partial \hat{U}_{k,l}(m,n)} \frac{\partial \hat{U}_{k,l}(m,n)}{\partial \hat{z}_k}. \tag{3.29}$$

Differentiating Equation (3.6) yields

$$\frac{\partial \hat{U}_{k,l}(m,n)}{\partial \hat{z}_k} = 2\pi i \hat{U}_{k,l}(m,n) \sqrt{\frac{1}{\lambda_l^2} - m^2\Delta_m^2 - n^2\Delta_n^2}\ . \tag{3.30}$$

Thus we have

$$\frac{\partial \Phi_d}{\partial \hat{z}_k} = \sum_{m,n}^{M_l,N_l} \hat{U}^{\dagger *}_{k,l}(m,n) \hat{U}_{k,l}(m,n) 2\pi i \sqrt{\frac{1}{\lambda_l^2} - m^2\Delta_m^2 - n^2\Delta_n^2} \tag{3.31}$$

$$\frac{\partial \Phi_d}{\partial \hat{z}_k} = \sum_{m,n}^{M_l,N_l} \mathrm{IM}\{i2\pi\} \sqrt{\frac{1}{\lambda_l^2} - m^2\Delta_m^2 - n^2\Delta_n^2} \hat{U}^{\dagger}_{k,l}(m,n) \hat{U}^{*}_{k,l}(m,n), \tag{3.32}$$

where we have used the fact that $\frac{\partial \Phi_d}{\partial \hat{z}_k} \in \mathbf{R}$ and our previous proof of $\mathrm{IM}\left[iz_1^* z_2\right] = iz_1 z_2^*$ if $iz_1 z_2^* \in \mathbf{R}$.

3.2.5 Gradient with respect to Pupil Phase

As we did in section 2.2.7, we will use multiple iterations of the chain rule. We progress in the same manner, starting with with $\frac{\partial \Phi_d}{\partial \hat{U}_{k,l}(m,n)}$ and then differentiating with respect to $\hat{U}_{f,l}(m,n)$, $\hat{E}_{f,l}(p,q)$, $\hat{E}_{p,l}(m,n)$, and finally $\hat{\phi}_l(m,n)$. We start with

$$\frac{\partial \Phi_d}{\partial \hat{U}_{f,l}(m',n')} = \sum_{m,n} \frac{\partial \Phi_d}{\partial \hat{U}_{k,l}(m,n)} \frac{\partial \hat{U}_{k,l}(m,n)}{\partial \hat{U}_{f,l}(m',n')} \tag{3.33}$$

and

$$\frac{\partial \hat{U}_{k,l}(m,n)}{\partial \hat{U}_{f,l}(m',n')} = \exp\left[i2\pi \hat{z}_k \sqrt{\frac{1}{\lambda_l^2} - m^2\Delta_m^2 - n^2\Delta_n^2} \right] \tag{3.34}$$

if $m = m'$ and $n = n'$, otherwise it is zero. Using this we can write

$$\frac{\partial \Phi_d}{\partial \hat{U}_{f,l}(m',n')} = \hat{U}_{k,l}^{\dagger *}(m,n) \exp\left(i2\pi \hat{z}_k \sqrt{\frac{1}{\lambda_l^2} - m^2\Delta_m^2 - n^2\Delta_n^2} \right) \tag{3.35}$$

$$\frac{\partial \Phi_d}{\partial \hat{U}_{f,l}(m',n')} = \hat{U}_{f,l}^{\dagger *}(m,n) \tag{3.36}$$

where we have defined

$$\hat{U}_{f,l}^{\dagger}(m,n) = \hat{U}_{k,l}^{\dagger}(m,n) \exp\left(-i2\pi \hat{z}_k \sqrt{\frac{1}{\lambda_l^2} - m^2\Delta_m^2 - n^2\Delta_n^2} \right) \tag{3.37}$$

Using Equation (3.5) lets us write

$$\frac{\partial \hat{U}_{f,l}(m,n)}{\partial \hat{E}_{f,l}(p',q')} = \frac{1}{\sqrt{M_l N_l}} \exp\left[-i2\pi \left(\frac{mp'}{M_l} + \frac{nq}{N_l} \right) \right] \tag{3.38}$$

where only the $p = p'$ and $q = q'$ terms are nonzero in the summation over (p,q). Thus

$$\frac{\partial \Phi_d}{\partial \hat{E}_{f,l}(p',q')} = \sum_{m,n} \hat{U}_{f,l}^{\dagger *}(m,n) \frac{1}{\sqrt{M_l N_l}} \exp\left[-i2\pi \left(\frac{mp'}{M_l} + \frac{nq'}{N_l} \right) \right] \tag{3.39}$$

$$\frac{\partial \Phi_d}{\partial \hat{E}_{f,l}(p',q')} = \hat{E}_{f,l}^{\dagger *}(p',q') \tag{3.40}$$

where we have defined

$$\hat{E}_{f,l}^{\dagger}(p',q') = \frac{1}{\sqrt{M_l N_l}} \sum_{m,n} \hat{U}_{f,l}^{\dagger}(m,n) \exp\left[+i2\pi \left(\frac{mp'}{M_l} + \frac{nq'}{N_l} \right) \right]. \tag{3.41}$$

Next we calculate

$$\frac{\partial \Phi_d}{\partial \hat{E}_{p,l}(m',n')} = \sum_{p,q} \frac{\partial \Phi_d}{\partial \hat{E}_{f,l}(p,q)} \frac{\partial \hat{E}_{f,l}(p,q)}{\partial \hat{E}_{p,l}(m',n')}. \tag{3.42}$$

Using Equation (3.4) yields

$$\frac{\partial \hat{E}_{f,l}(p,q)}{\partial \hat{E}_{p,l}(m',n')} = \frac{1}{\sqrt{M_l N_l}} \frac{\lambda_0}{\lambda_l} \exp\left[\frac{i\pi}{\lambda_l f}\left(p^2\Delta_p^2 + q^2\Delta_q^2\right)\right] \exp\left[-i2\pi\left(\frac{m'p}{M_l} + \frac{n'q}{N_l}\right)\right]. \tag{3.43}$$

We therefore have

$$\frac{\partial \Phi_d}{\partial \hat{E}_{p,l}(m',n')} = \frac{1}{\sqrt{M_l N_l}} \frac{\lambda_0}{\lambda_l} \sum_{p,q}^{M_l,N_l} \hat{E}_{f,l}^{\dagger *}(p,q) \exp\left[\frac{i\pi}{\lambda_l f}\left(p^2\Delta_p^2 + q^2\Delta_q^2\right)\right] \exp\left[-i2\pi\left(\frac{m'p}{M_l} + \frac{n'q}{N_l}\right)\right] \tag{3.44}$$

$$\frac{\partial \Phi_d}{\partial \hat{E}_{p,l}(m',n')} = \hat{E}_{p,l}^{\dagger *}(m',n') \tag{3.45}$$

where we have defined

$$\hat{E}_{p,l}^{\dagger}(m',n') = \frac{1}{\sqrt{M_l N_l}} \frac{\lambda_0}{\lambda_l} \sum_{p,q}^{M_l,N_l} \hat{E}_{f,l}^{\dagger}(p,q) \exp\left[\frac{-i\pi}{\lambda_l f}\left(p^2\Delta_p^2 + q^2\Delta_q^2\right)\right] \exp\left[+i2\pi\left(\frac{m'p}{M_l} + \frac{n'q}{N_l}\right)\right]. \tag{3.46}$$

Next, we calculate

$$\frac{\partial \Phi_d}{\partial \hat{\phi}_l(m',n')} = \sum_{l=1}^{L} \frac{\partial \Phi_d}{\partial \hat{E}_{p,l}(m,n)} \frac{\partial \hat{E}_{p,l}(m,n)}{\partial \hat{\phi}_l(m',n')}. \tag{3.47}$$

From Equation (3.1) we have

$$\frac{\partial \hat{E}_{p,l}(m,n)}{\partial \hat{\phi}_l(m',n')} = i\frac{\lambda_0}{\lambda_l} \hat{E}_{p,l}(m,n) \tag{3.48}$$

and hence

$$\frac{\partial \Phi_d}{\partial \hat{\phi}_l(m',n')} = \sum_{l=1}^{L} i\frac{\lambda_0}{\lambda_l} \hat{E}_{p,l}^{\dagger *}(m',n') \hat{E}_{p,l}(m,n) \tag{3.49}$$

$$\frac{\partial \Phi_d}{\partial \hat{\phi}_l(m',n')} = \mathrm{IM}\left[\sum_{l=1}^{L} \frac{\lambda_0}{\lambda_l} \hat{E}_{p,l}^{\dagger}(m',n') \hat{E}_{p,l}^{*}(m,n)\right], \tag{3.50}$$

where we have used $\frac{\partial \Phi_d}{\partial \hat{\phi}_l(m',n')}$ is real.

We will consider decomposing the $\hat{\phi}_l(m,n)$ wavefronts into basis polynomials (e.g., Zernike polynomials) which are allowed to vary as a function of wavelength. We can write:

$$\hat{\phi}_l(m,n) = \sum_{j=1}^{J} \alpha_{j,l} Z_j(m,n). \tag{3.51}$$

To calculate the gradient of the objective function with respect to the coefficients we start with

$$\frac{\partial \Phi_d}{\partial \alpha_{j,l}} = \sum_{m,n} \frac{\partial \Phi_d}{\partial \hat{E}_{p.l}(m',n')} \frac{\partial \hat{E}_{p.l}(m',n')}{\partial \alpha_{j,l}}. \tag{3.52}$$

We have

$$\hat{E}_{p,l}(m,n) = \hat{A}(m,n) \exp\left[i \frac{\lambda_0}{\lambda_l} \sum_{j=1}^{J} \alpha_{j,l} Z_j(m,n) \right] \tag{3.53}$$

and hence

$$\frac{\partial \hat{E}_{p,l}(m,n)}{\partial \alpha_{j,l}} = i \frac{\lambda_0}{\lambda_l} Z_j(m,n) \hat{E}_{p,l}(m,n). \tag{3.54}$$

We therefore have

$$\frac{\partial \Phi_d}{\partial \alpha_{j,l}} = \sum_{m,n} i \frac{\lambda_0}{\lambda_l} Z_j(m,n) \hat{E}_{p,l}(m,n) \hat{E}^{\dagger *}_{p,l}(m,n) \tag{3.55}$$

$$\frac{\partial \Phi_d}{\partial \alpha_{j,l}} = \sum_{m,n} \frac{\lambda_0}{\lambda_l} Z_j(m,n) \mathrm{IM}\left[\hat{E}^{*}_{p,l}(m,n) \hat{E}^{\dagger}_{p,l}(m,n) \right]. \tag{3.56}$$

3.2.6 Gradient with respect to Spectral Weights

To calculate the gradient of the objective function with respect to spectral weights we use the chain rule once again. We can write

$$\frac{\partial \Phi_d}{\partial S_l} = \sum_{k=1}^{K} \sum_{p,q} \frac{\partial \Phi_d}{\partial \hat{I}_k(p,q)} \frac{\partial \hat{I}_k(p,q)}{\partial S_l}. \tag{3.57}$$

We have $\frac{\partial \Phi_d}{\partial \hat{I}_k(p,q)}$ from Equation (2.60). We can use Equation (3.8) to calculate

$$\frac{\partial \hat{I}_k(p,q)}{\partial S_l} = \frac{1}{L} \left| \hat{E}_{k,l}(p,q) \right|^2 \tag{3.58}$$

and hence

$$\frac{\partial \Phi_d}{\partial S_l} = \frac{1}{L\sqrt{MN}} \sum_{p,q} \sum_{k=1}^{K} \sum_{m,n} \hat{f}_k^{\dagger}(m,n) \exp\left[i2\pi \left(\frac{mp}{M} + \frac{nq}{N} \right) \right] \left| \hat{E}_{k,l}(p,q) \right|^2 \tag{3.59}$$

$$\frac{\partial \Phi_d}{\partial S_l} = \frac{1}{L} \sum_{k=1}^{K} \sum_{p,q} \mathrm{IDFT}\left[\hat{f}_k^{\dagger}(m,n) \right] \left| \hat{E}_{k,l}(p,q) \right|^2. \tag{3.60}$$

4 BROADBAND SIMULATION

Initial broadband simulations to investigate aberration recovery using the phase diversity algorithm described in Section 3 use a simplified aberration and optical system model as depicted in Figure 14.

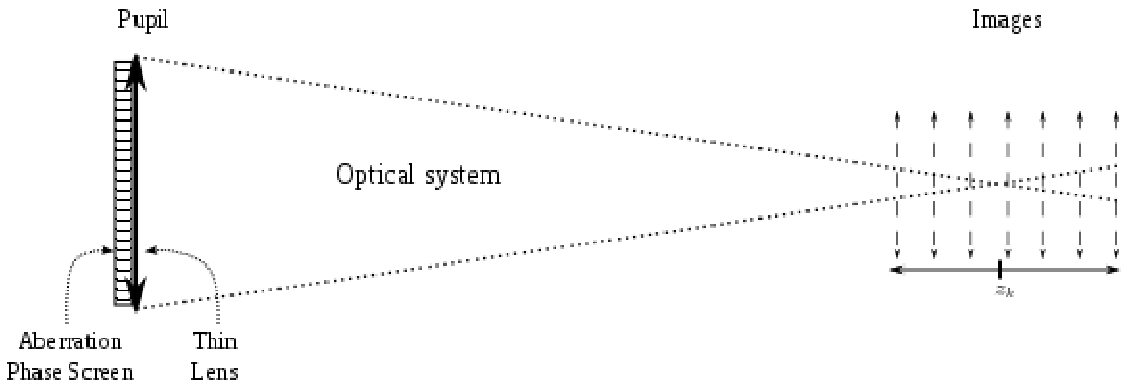

Figure 14: Basic optical model used in simulations

The phase screen is constructed using a set of Zernike polynomials with random coefficients. Zernike polynomials are functions which are orthogonal on the unit circle. There are several realizations of these polynomials with differing orderings; we have elected mainly to use those described by Noll (Noll 1976).

The Zernike polynomials are used to describe system aberrations. Some orders correspond to named aberrations (e.g., Z4 corresponds to focus shift, while Z8 corresponds to third-order coma along the *x*-axis). The phase in the pupil plane for the ℓth wavelength is computed by

$$\phi_\ell\left(m,n\right)=\sum_{i=1}^{N}\alpha_i W_i Z_i\left(m\Delta_m, n\Delta_n\right), \tag{4.1}$$

where α_i is the coefficient for the ith Zernike polynomial, W_i is a normalizing weighting factor, and N is the total number of Zernike polynomials to be used.. The electric field is then calculated and propagated as discussed in Section 3.2.1. Reconstruction was done using the conjugate-gradient minimization function as described in section 2.3.

4.1 Simulation at Five Discrete Wavelengths

The initial examination of the algorithm involved simulation and reconstruction at five wavelengths: 525 nm, 575 nm, 632.8 nm, 625 nm, and 725 nm, with 632.8 nm designated as the "reference wavelength". In preparation for further research, some statistical research was required in order to evaluate the goodness of the recovery (Zernike optimization) algorithm. Initially, fifty-one simulation sets were run. The optical system modeled was f/10, with a one inch diameter pupil and 11 diversity planes axially spread ±1.0 mm from the focal point.

A simulated set of diversity plane point spread functions was obtained with a simulated pupil wavefront aberration constructed of Zernike terms to the 14th order. The coefficients of the random terms were derived from a normal distribution. Coefficients were then scaled by 2^{-n}, where *n* is the order of the corresponding Zernike polynomial. Finally, the total simulation

aberration was scaled to produce a root-mean-square (RMS) wavefront error of 0.15 waves (0.94 radians) at the reference wavelength.

Optimizations were conducted in several sections. First, in order to simulate correction for positional error, the error metric was optimized for lateral and axial position a total of 25 times. Following that, an optimization for pupil Zernike coefficients of tip, tilt, and focus (Z2-Z4) was performed for 35 iterations. Next, 35 iterations of optimization of all wavelength- and diversity plane-dependent Zernike terms through 7th order were conducted. Finally, a point-by-point phase optimization in the pupil plane was conducted for 200 iterations. Results are shown in Figure 15(a).

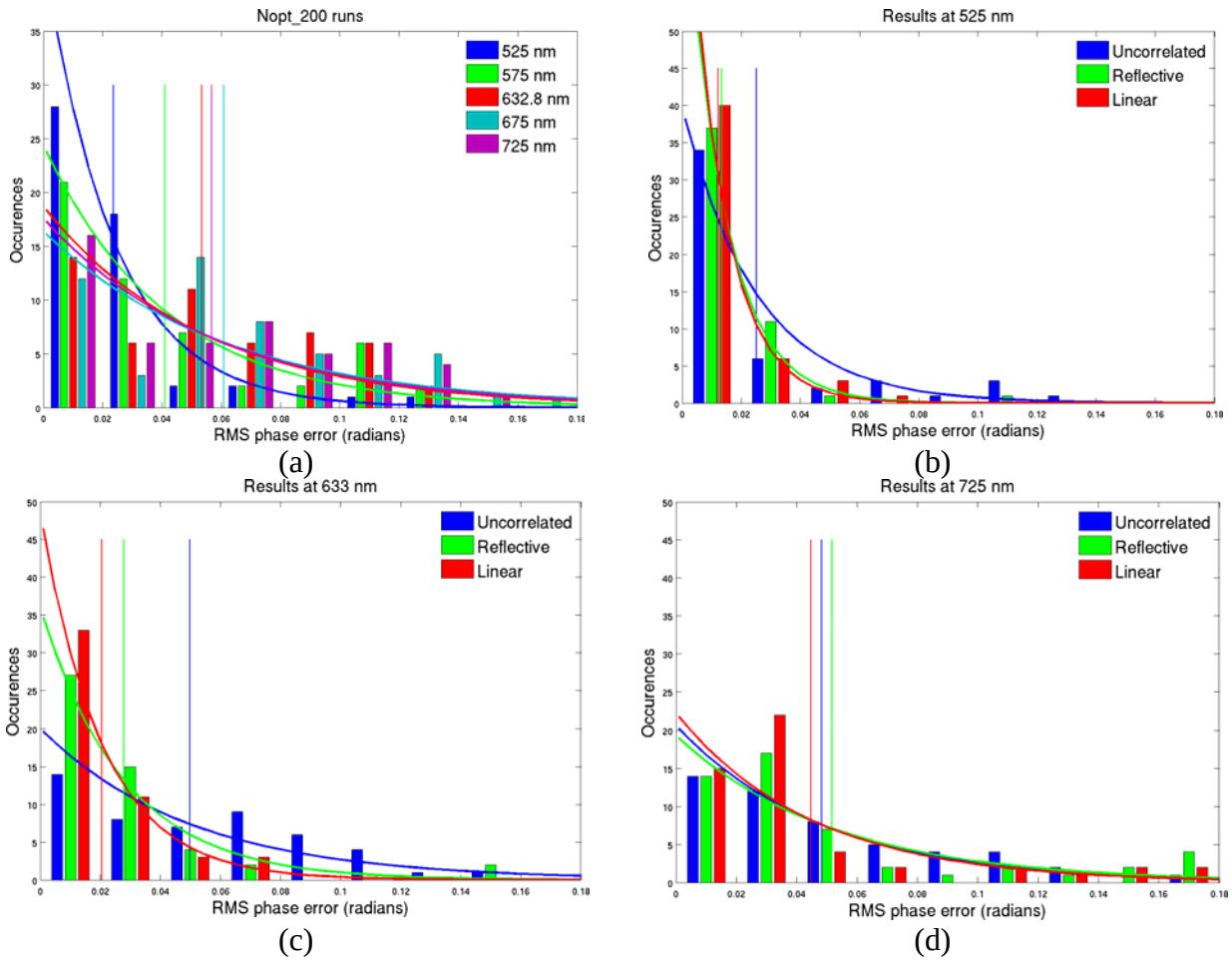

Figure 15: Histograms of wavefronts after phase diversity reconstruction: Five wavelengths were used to simulate a broadband signal, with the algorithm attempting to recover the simulated aberrations at those same wavelengths. Nine histogram bins per wavelength are shown. Vertical lines mark the mean values, and curves representing a log-normal distribution with the respective mean are plotted for visual effect. (a) Uncorrelated aberrations. (b)–(d) Comparisons of remaining wavefront errors when the aberrations are uncorrelated, identical ("reflective"), and linearly correlated.

Aberration reconstruction was much better for the shorter wavelengths than the longer wavelengths. However, even the worst case showed a significant recovery of the original aberration, averaging more than 90% even at the longer wavelengths.

The computation time for an average wavefront reconstruction in the above set was 2:27 hours. Some experimentation showed that changing the number of iterations to 25 for axial and lateral optimization, 35 for tip, tilt, and focus Zernike term optimization, 50 for optimization of all Zernike polynomials, and finally 50 for point-by-point phase optimization, reduced the time to 1:23 hours, while only suffering less than a 0.005 radian change in RMS phase error. Due to the reduction in computational time of over 40%, this sequence of optimizations was used in the subsequent few sets of simulations.

In a real system, it is likely that the wavefront error would be a smoothly varying function of wavelength rather than totally uncorrelated. Statistical runs were next conducted using identical Zernike coefficients for each wavelength (with phase variation measured in terms of the reference wavelength). This would reasonably model a totally reflective optical system. Statistical runs were also run with the coefficients being a linear function of wavelength, varying approximately ±20% from those of the reference wavelength. A histogram of the resulting RMS wavefront errors (between simulated and recovered pupil phases) is shown in Figure 15(b) – (d). Once again, in all cases the shorter wavelength phase errors were recovered more precisely, with the correlated aberrations showing a significant improvement in recovery. However, this benefit was reduced at longer wavelengths, with only minor improvement noticed at the longest wavelength.

In the above simulations, the simulated spot size was produced with an aberration error formed with Zernike terms through order 14 and recovered with terms only through 7th order. This placed an upper bound on the ability of the algorithm to recover the original aberrations in terms of Zernike polynomials alone. The use of point-by-point phase aberration is intended to ameliorate this problem.

In order to examine the significance of this effect, a set of simulations was done in which both the simulated phase errors used to produce the PSFs, as well as the recovered phase errors, were composed of Zernike polynomials up to 7th order.

Results are depicted in Figure 16(a). In these plots, “Same order” refers to the use of 7th order Zernike polynomials for both simulation of the input error (used to create the PSFs) and for the Zernike coefficient recovery portion of the optimization sequence. “Different orders” refers to the use of 14th order Zernike polynomials to create the simulated aberrations and PSF, with the Zernike coefficients being recovered limited to the use of 7th order Zernike polynomials. Once again the shorter wavelength aberrations were extrapolated significantly better than those of longer wavelengths.

Of interest, as shown in Figure 16(b) – (f), when compared to the earlier simulations with different orders, there is a significant improvement in reconstruction at the longer wavelengths when the Zernike recovery algorithm is of the same order as the simulated aberrations. Since the optimization based upon Zernike coefficients at the pupil precedes the optimization based upon a

point-by-point phase, this may indicate that the Zernike coefficients for the shorter wavelengths are better optimized than those at longer wavelengths. As a result of this, the point-by-point phase optimization process would make relatively better progress at the longer wavelengths, since the starting point (in terms of Zernike coefficients) is further from the ideal than is the case at shorter wavelengths.

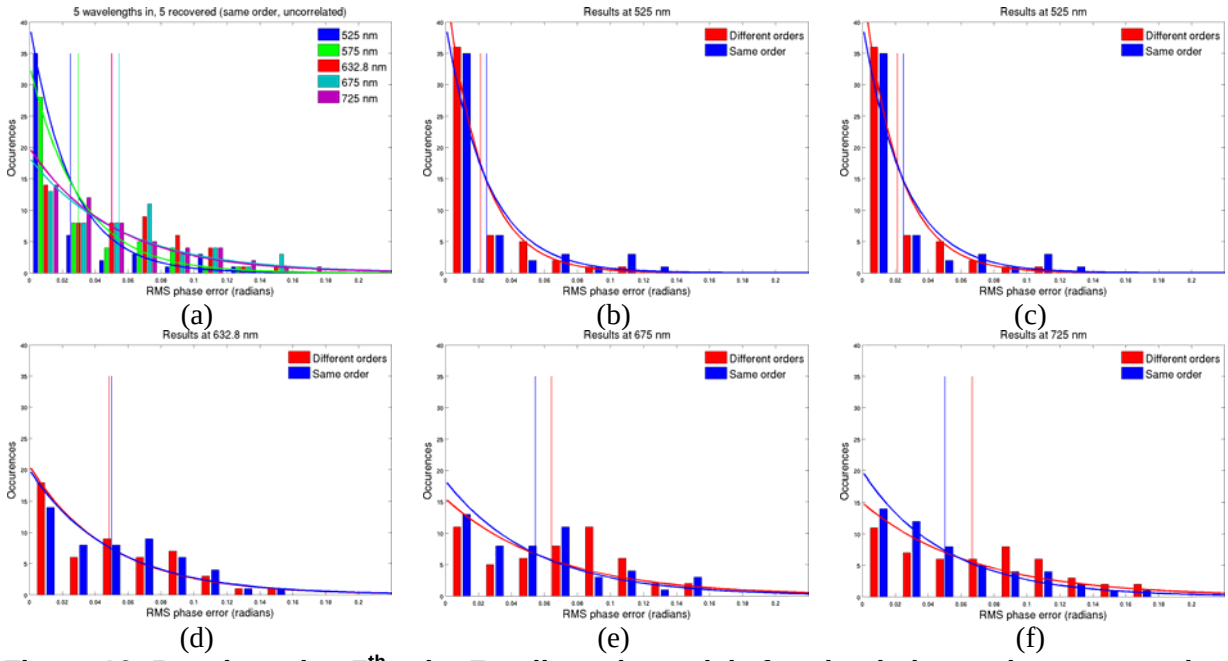

Figure 16: Results using 7th order Zernike polynomials for simulation and reconstruction: Eleven histogram bins are shown, with a vertical line plotted at the mean value and a log-normal curve plotted for visual effect. (a) A comparison of results by wavelength. (b)– (f) Comparison by wavelength to simulations where Zernike polynomials through order 14 (labeled "Different orders") was used to create the simulated image PSFs.

5 EXPERIMENTAL TESTING

The broadband phase-diverse phase retrieval algorithm was tested with two lasers of significantly different wavelengths. The testbed layout shown in Figure 2 was modified to the configuration shown below.

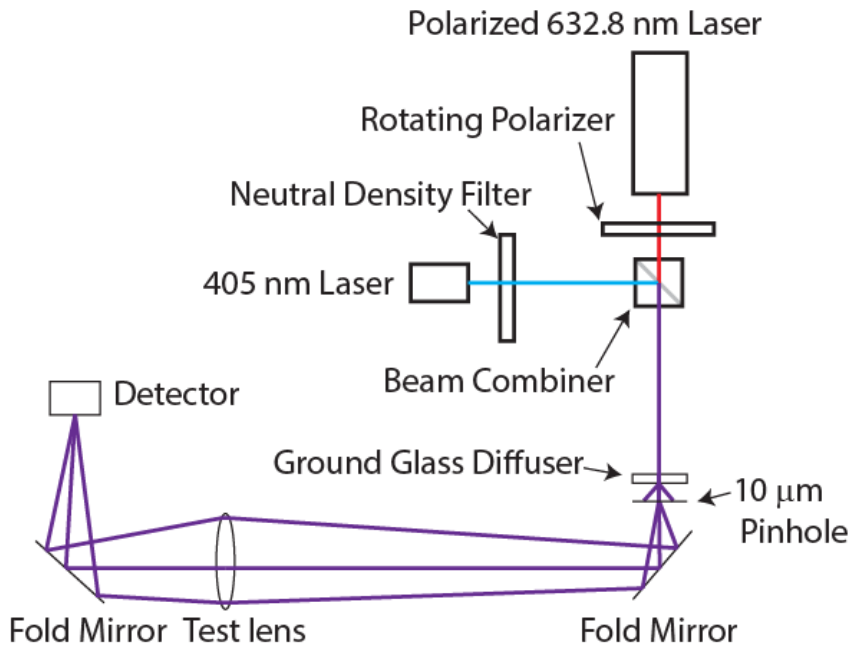

Figure 17: Dual-Wavelength Phase-Diverse Phase Retrieval Testbed Configuration

This configuration was used to combine the two laser beams. The 632.8 nm laser was polarized and its amplitude was controlled by the use of the rotating polarizer. The 405 nm laser was not polarized and its amplitude was controlled via a neutral density filter. These beams were combined with a polarization-insensitive beam combiner and illuminated a ground glass diffuser. The ground glass diffuser served to provide uniform illumination of the 10 μm pinhole. This makes the alignment of the two beams relative to each other rather insensitive and also serves to reduce beam amplitudes to levels that do not saturate the detector.

Data were first collected with each laser independently. The monochromatic phase-diverse phase retrieval algorithm described in Section 2 was used to independently measure the wavefronts at the two wavelengths. The axial shifts of the spots were not allowed to vary in this analysis. Instead, the Z4 (defocus) Zernike coefficient was allowed to vary. This allows for the focus of the system to be adjusted axially while maintaining the known separations between the measurement planes. A single frame of data at each of three defocus depths was used to perform the reconstructions.

The relative strengths of the two beams were characterized by comparing the total energy (in detector counts) of the two beams when incident on the detector independently. The ratio of the total energy in the 632.8 nm beam to the 405 nm beam was 0.65.

5.1 Simulations of Broadband Images

By definition, current phase-diversity reconstruction techniques are based upon optimizing an error function at discrete wavelengths. In other words, it is multi-spectral, and rather than truly broadband. The purpose of our investigation is to determine the extent to which this multi-spectral technique can be used in the presence of a broadband image.

This subsection reports the results of simulations of a pseudo-broadband system with multi-spectral phase diversity reconstruction of pupil plane phase aberrations. The simulated optical system is modeled on the test bed described in Section 5, which is an f/16 system with a 1.65" (41.9 mm) circular aperture. Diversity plane locations were set at locations 1 mm apart on the range $-5\text{ mm} \le z \le 5\text{ mm}$, with the nominal focus at the origin. To simulate jitter in the detector as it is set to the various diversity planes, the *x*- and *y*- locations were offset a random distance described by a normal distribution with a standard deviation of 20 pixels. Since jitter along the *z*-axis can be subsumed into the coefficients of the focus Zernike polynomial (Z4) peculiar to each diversity plane, no *z*-axis jitter was simulated.[1] We also defined the pupil aberrations to be correlated linearly with wavelength, *i.e.,* that the aberrations, in terms of coefficients of Zernike polynomial bases functions, are linear functions of wavelength, in the same manner as in Section 4.1. The RMS wavefront error at the reference wavelength (632.8 nm) was maintained at 0.15 waves (0.94 radians).

Two multi-spectral broadband wavelength distributions were used in addition to a five-wavelength simulation at the wavelengths used for reconstruction. The following numbers and wavelengths used were:

- **Five:** 525 nm, 575 nm. 632.8 nm, 675 nm, 725 nm
- **Nine:** 525 nm, 550 nm, 575 nm, 600 nm, 632.8 nm, 650 nm, 675 nm, 700 nm, 725 nm
- **Eleven:** 500 nm, 525 nm, 550 nm, 575 nm, 600 nm, 632.8 nm, 650 nm, 675 nm, 700 nm, 725 nm, 750 nm

The five wavelengths are those at which pupil aberrations are recovered. These are present in the simulation in all cases. For nine wavelengths, additional PSFs were inserted by incoherent addition from wavelengths in between the original set. For eleven wavelengths, two additional wavelengths, outside the recovery band, were added. These two sets were chosen as a baselines to examine the ability of the phase diversity phase recovery algorithm to function in the presence of signals outside the recovery wavelengths: if the algorithm didn't perform adequately in these situations, it would have no hope of performing in the case of a true broadband signal.

[1] It was found in simulations that optimizing these focus terms as well as *z*-axis location could lead to "fighting" between the two. Since other Zernike coefficients that vary by diversity plane are optimized in the diversity algorithm, it was believed most efficient to set the *z*-axis locations to their nominal values.

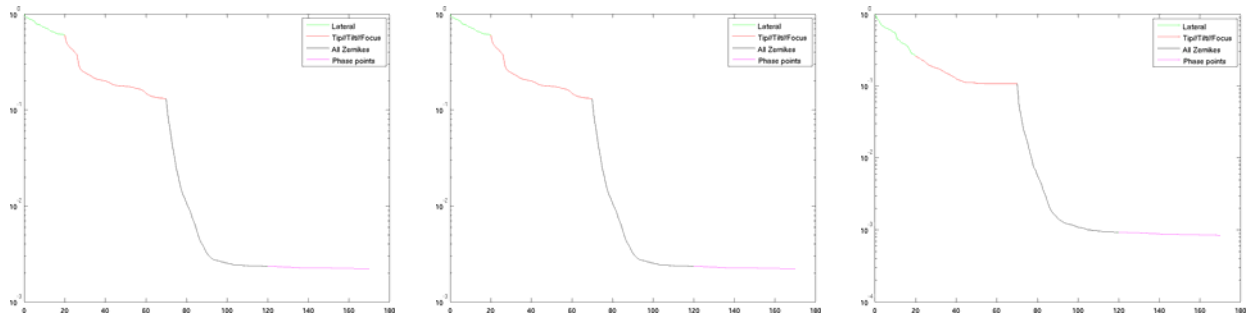

(a) (b) (c)

Figure 18: Log of the error function versus iteration step for an arbitrary simulation: In each case, the error function was computed for recovery at five wavelengths. The simulated PSFs were constructed from simulations using the specified number of wavelengths (see text). (a) Five wavelengths. (b) Nine wavelengths. (c) Eleven wavelengths.

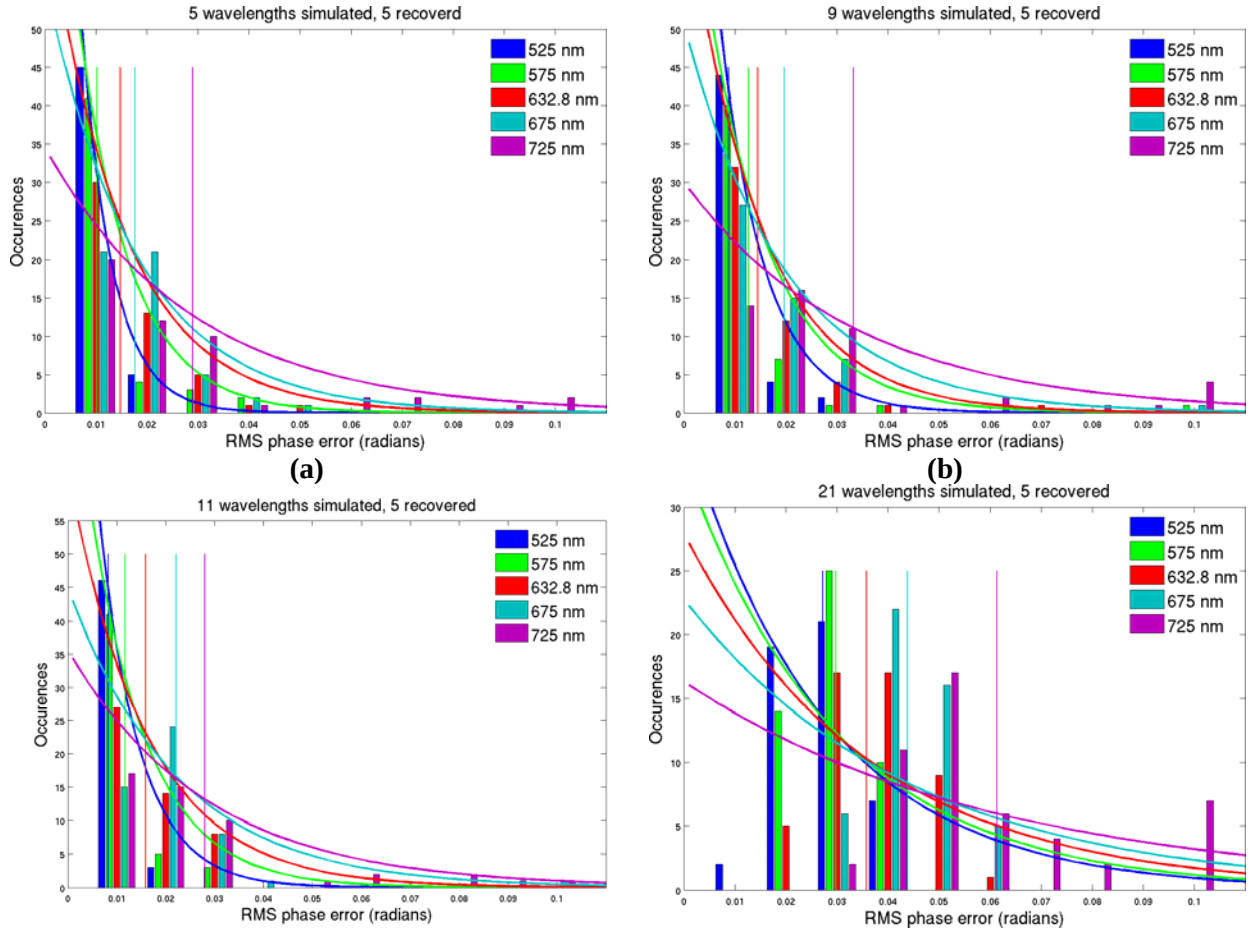

(a) **(b)** **(c)** **(d)**

Figure 19: Histograms showing phase errors for 50 simulation runs in each set: All sets recovered phase errors at five wavelengths. The simulated PSFs were constructed from simulations using the specified number of wavelengths (see text). (a) Five wavelengths. (b) Nine wavelengths. (c) Eleven wavelengths. (d) Twenty-one wavelengths. The right-most bin includes all values equal to or greater than 0.10 radians.

The phase error remaining after phase recovery at five wavelengths was similar in both the case where five wavelengths were used to create the simulated PSFs and where nine wavelengths within the wavelength band were used, as shown in

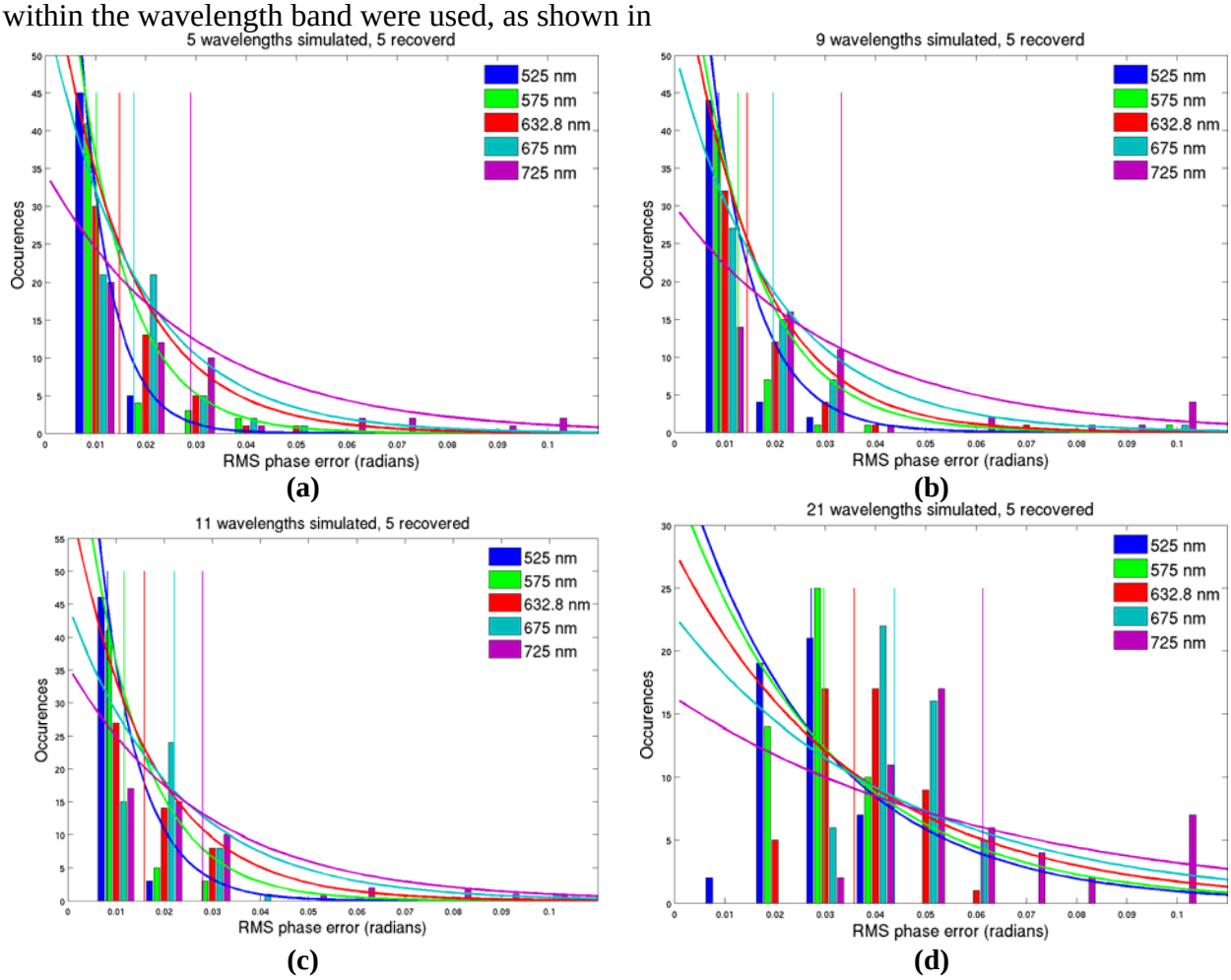

Figure 19 (a) and (b). As noted in section 4.1, the phase errors at shorter wavelengths were notably less accurate than those at longer wavelengths. When eleven wavelengths, including two outside the recovery band, were used to construct the simulated PSFs, there was a notable increase in average phase error for the middle wavelengths. In other words, the benefits of the shorter wavelength seen in previous reconstructions were reduced. The exact cause is unclear, but it is hypothesized that the shortest wavelength, having the more tightly focused PSF (*i.e.*,a smaller Airy disk) has a greater impact on the PSF images than longer wavelengths with their "softer" foci.

In order to better simulate a true broadband signal, a set of simulations was run with 21 wavelengths, ranging from 375 nm through 875 nm, used to create the simulated PSFs. The RMS wavefront error at the reference wavelength ($\lambda_0 = 632.8$ nm) was held to 0.15 waves (0.94 radians). In addition, to better simulate an actual signal, the intensities were spectrally weighted by a Gaussian function,

$$S_l(\lambda_n) = \exp\left(-1\frac{(\lambda_n - \lambda_0)^2}{\sigma^2}\right); \quad \sigma = 500\,\text{nm}. \tag{5.1}$$

The statistics for 50 simulation runs are shown in Figure 19(d).

A definite lowering of recovery accuracy was noted, with the average of the shorter wavelengths performing no better than the worst wavelength in the earlier simulations with only five spectral components. On the other hand, the remaining wavefront error for the longer wavelengths almost doubled. Even so, the phase diversity algorithm still recovered more than 90% of the original wavefront error, indicating that phase diversity is a promising method for broadband phase error reconstruction.

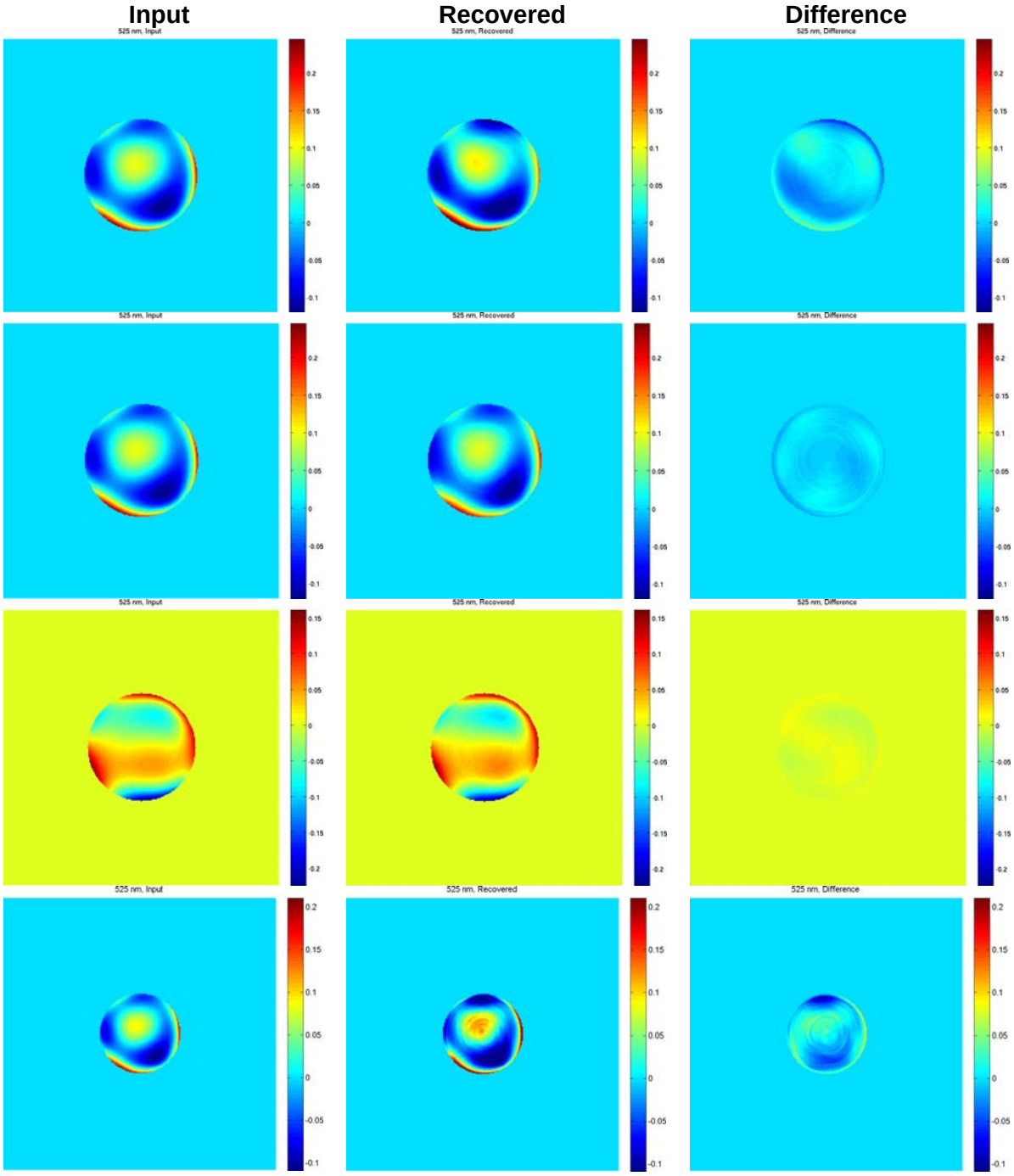

Figure 20: Wavefront reconstructions at 525 nm for an arbitrarily selected simulation: Columns are simulated input phase, recovered phase, and difference. Rows indicate the number of simulation wavelengths (see text). Piston, tip/tilt, and power are removed.

Figure 20 (525 nm), Figure 21 (632.8 nm), and Figure 22 (725 nm) depict the results for four arbitrarily selected reconstructions, one each from simulations using five, nine, eleven, and 21

wavelengths to create the PSFs.[2] Again, it is readily apparent that phase-diversity aberration reconstruction is beneficial in each of these cases.

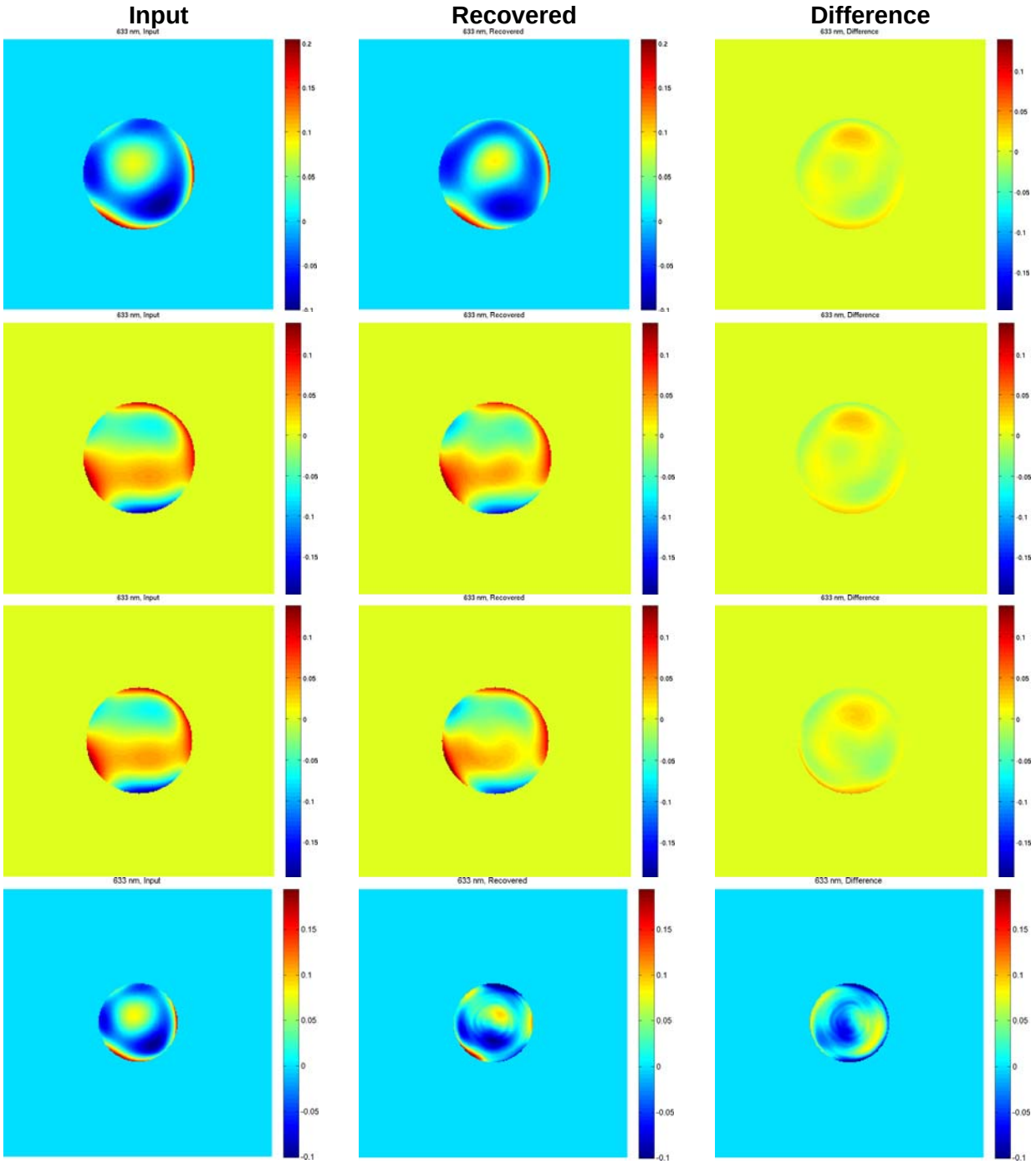

Figure 21: Wavefront reconstructions at 633 nm for an arbitrarily selected simulation: Columns are simulated input phase, recovered phase, and difference. Rows indicate the number of simulation wavelengths (see text). Piston, tip/tilt, and power are removed.

[2] The zero-phase reference is arbitrary depending upon the random nature of the phase errors. In other words, the fact that the eleven-wavelength phase error is more negative while the others are more positive is not significant. Also, since these are individual simulations, they cannot be used to draw conclusions requiring a statistical analysis.

Simulations in support of two-wavelength testing are discussed in Section 5.4.

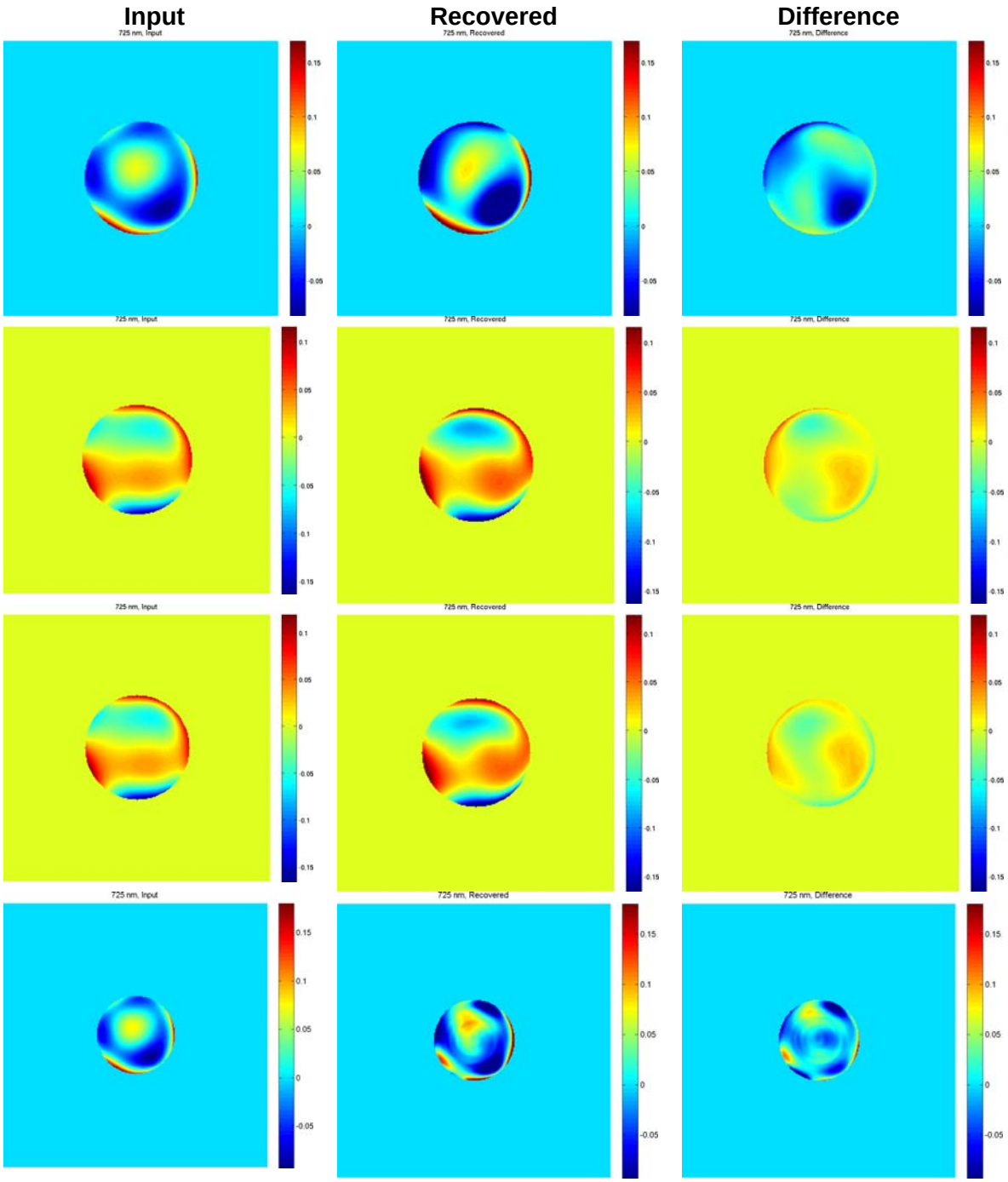

Figure 22: Wavefront reconstructions at 725 nm for an arbitrarily selected simulation: Columns are simulated input phase, recovered phase, and difference. Rows indicate the number of simulation wavelengths (see text). Piston, tip/tilt, and power are removed.

5.2 632.8 nm Monochromatic Testing

The axial coordinate system was set up so that the 632.8 nm wavelength had its best focus position near Z=0. The Z4 Zernike coefficient for the reconstructed wavefront at 632.8 nm was 0.0045 waves, corresponding to a relative shift between the actual best focus position and the Z=0 position of only 20 μm. The following figure shows the reconstructed wavefront at 632.8 nm with piston, tip, tilt, and power removed.

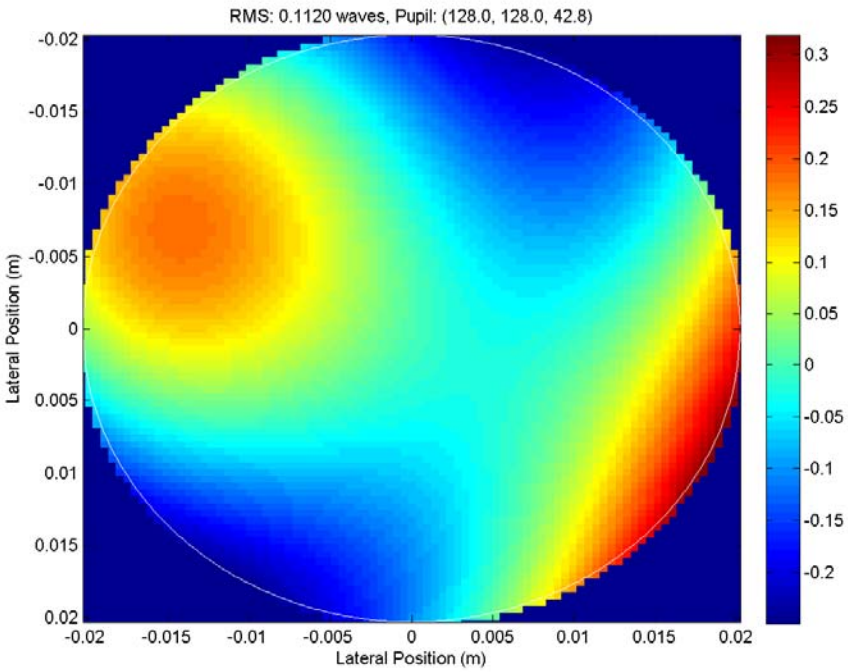

Figure 23: Reconstructed Wavefront at 632.8 nm without Piston, Tip, Tilt, and Power

No interferometric measurement was possible at this time as the interferometer had been sent back to the manufacturer to fix an electrical safety problem. These data were collected on July 3rd, 2012. The system had not been changed since the previous use on May 25th, 2012, though. On that day, an interferometric measurement was performed with the following result. The wavefront was fit to 37 Zernike coefficients to reduce radial ringing artifacts associated with the uncoated nature of the test lens.

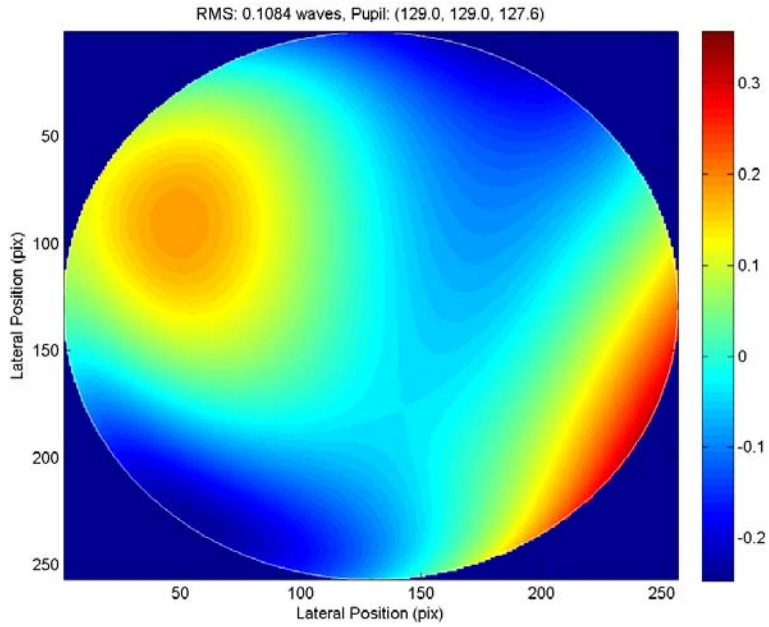

Figure 24: Interferometrically Measured Wavefront fit to 37 Zernike Terms

We see that Figure 23 and Figure 24 agree well. This is born out in the normalized root-mean-square error (NRMSE) analysis of the phase diversity reconstruction as well. NRMSE provides a metric for how well the reconstructed PSF matches the measured PSF. The following plot shows NRMSE as a function of position for the interferometer data collections made. The defocus depths of -4, 0, and +4 mm were used in the phase diversity reconstruction, the other depths were not.

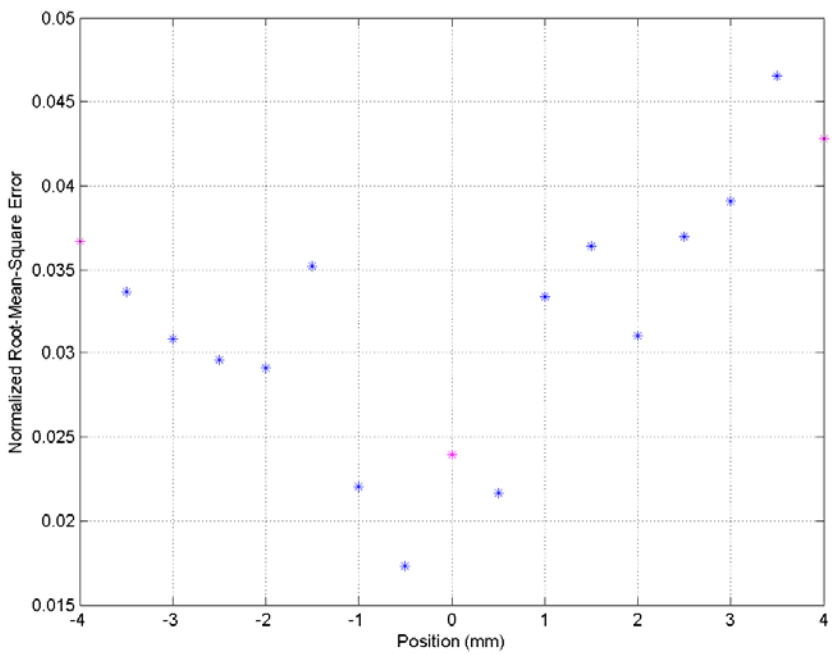

Figure 25: NRMSE vs. Position for the 632.8 nm Phase Diversity Reconstruction

Lastly, the reconstructed PSFs were compared visually against the measured PSFs. These can be seen to agree well. The following figure shows these PSFs at the -4 mm position.

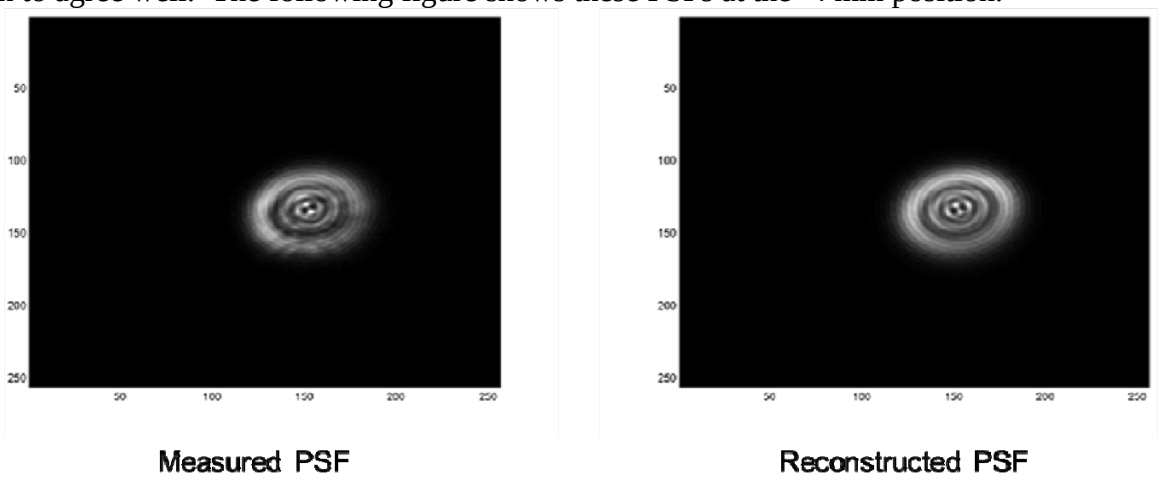

Figure 26: Measured and Reconstructed PSFs at -4 mm Position for the 632.8 nm Test

5.3 405 nm Monochromatic Testing

Next testing with the 405 nm laser as the only source was performed. The axial coordinate system was maintained. The reconstructed Z4 Zernike coefficient was 1.477 waves, corresponding to a focus shift of 4.122 mm. This agrees well with results from a Zemax model of the system, which predicts a shift of 4.046 mm. The following figure shows the reconstructed wavefront at 405 nm with piston, tip, tilt, and power removed.

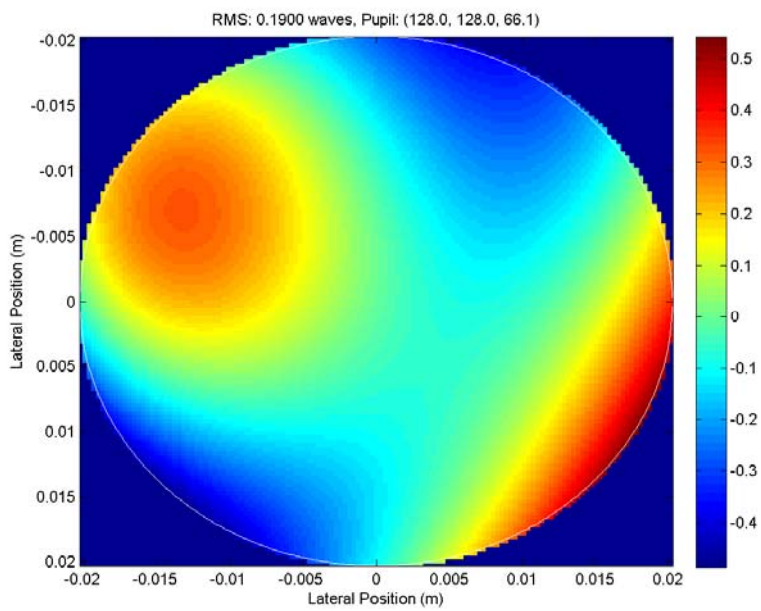

Figure 27: Reconstructed Wavefront at 405 nm without Piston, Tip, Tilt, and Power

No interferometric data exist since no interferometer is available at this wavelength. The following plot shows NRMSE versus position for this test. Data at five defocus depths (0.5, 2, 4.5, 6.5, and 8.5 mm) were used in the phase diversity reconstruction.

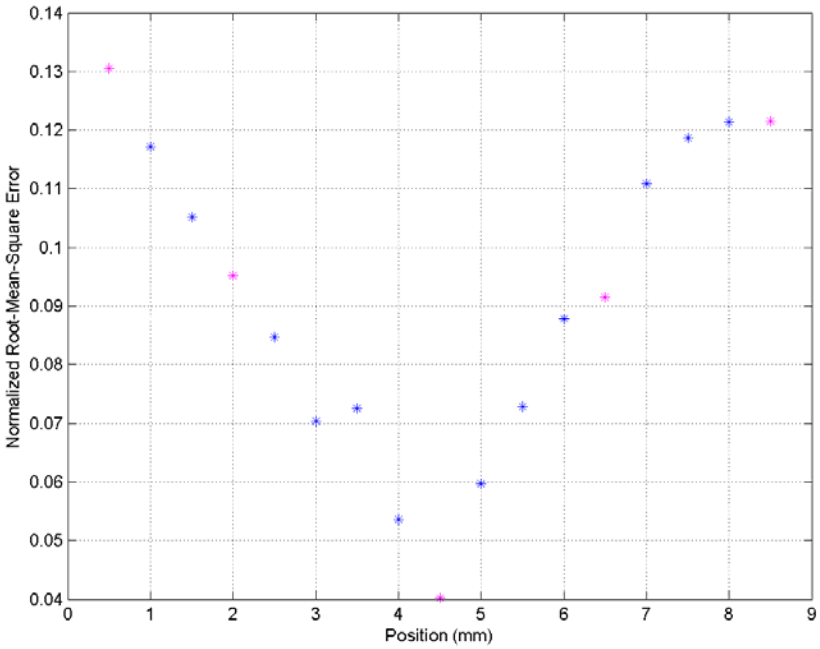

Figure 28: NRMSE vs. Position for the 405 nm Phase Diversity Reconstruction

Clearly the values for this reconstruction are higher than those shown in Figure 25. In particular, the data appear to have a characteristic V-shape. This is not understood at this time. The V-shape can be worsened by changing the focal length of the system, but the 661 mm focal length used in this simulation seems to give the best results.

The reconstructed PSFs also do not agree quite as well with the measured PSFs. The following figures show these PSFs at the 0.5 mm defocus depth.

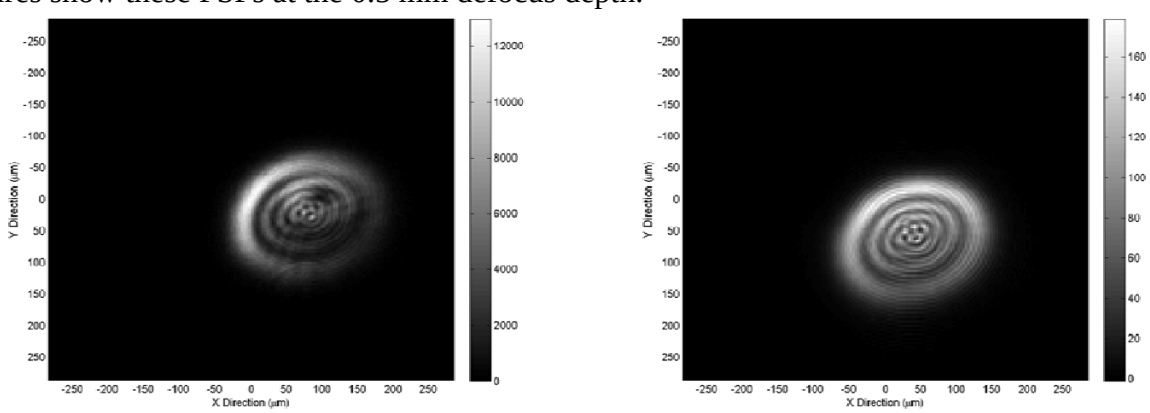

Measured PSF Reconstructed PSF

Figure 29: Measured and Reconstructed PSFs at 0.5 mm Position for the 405 nm Test

Testing with a true broadband spectral source was abandoned in favor of the two-wavelength methodology described above. This two-wavelength methodology provides a stepping stone to the broadband case from the monochromatic case that is considerably simpler.

It is not clear why the NRMSE is higher for the 405 nm case. It is perhaps likely that this is due to the shorter wavelength providing higher spatial frequency content in the PSF, which is more difficult to match. Indeed, the reconstructed PSF shown in Figure 29 shows some radial ringing artifacts that are not present in the measurement, perhaps because of motion blur.

The magnitude of the wavefront error being reconstructed is likely close to being correct. A Zemax model of the system was created and the tilt of the lens was set to 1.45°. The following wavefront was simulated for the 632.8 nm case:

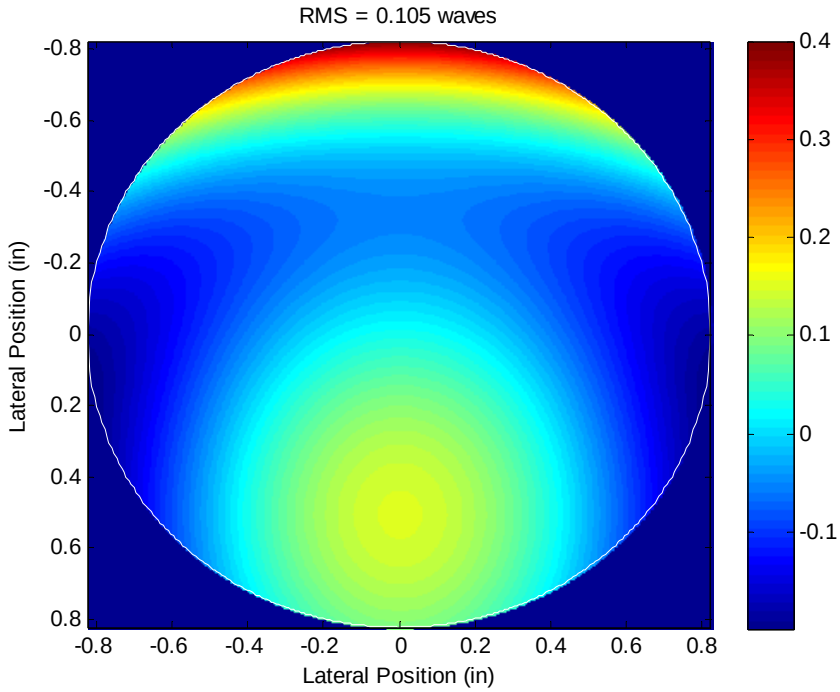

Figure 30: Zemax Model of 632.8 nm Wavefront assuming 1.45° Lens Tilt

Neglecting the rotation of the wavefront (which could be adjusted by changing the tilt angle in Zemax), the wavefront is similar to that shown in Figure 24. The corresponding wavefront at 405 nm is shown in the next figure.

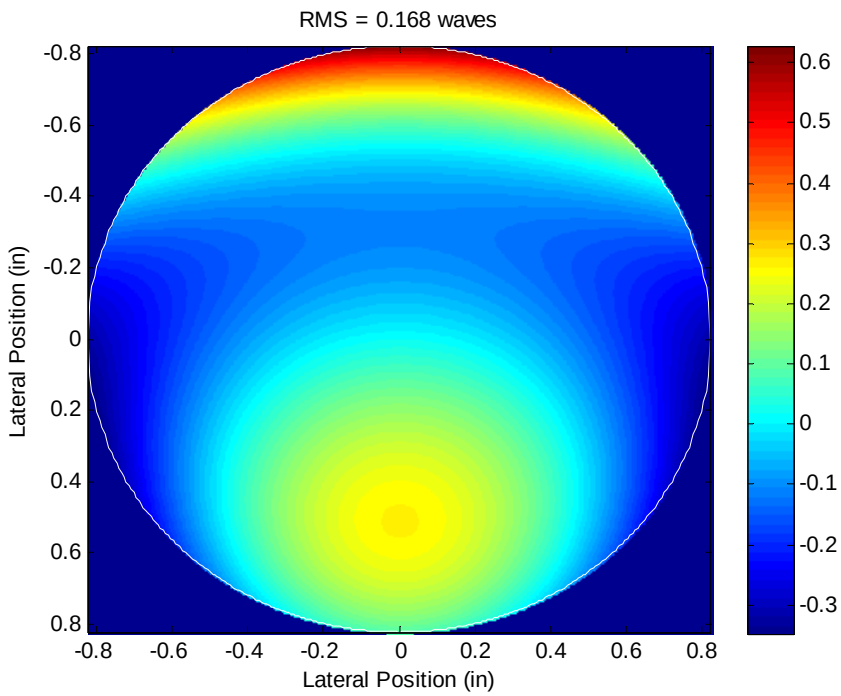

Figure 31: Zemax Model of 405 nm Wavefront assuming 1.45° Lens Tilt

As can be seen from these figures, the RMS wavefront error of the 405 nm wavefront is expected to be considerably greater than the RMS wavefront error of the 632.8 nm wavefront. In fact, the reconstructed value of 0.190 waves is not too far off from the predicted value of 0.168 waves.

5.4 Two-Wavelength Testing

A set of 50 simulations were run to examine the expected effect of the algorithm on an error-free experiment corresponding to the testbed. The spectral weights were assigned based upon laboratory measurements, but all other parameters are as specified in section 4, with Zernike polynomials through 9th order used to produce the PSFs and Zernike polynomials through 7th order used for recovery.

Figure 32(a) provides a histogram of the remaining RMS phase error. Performance was excellent with, in the majority of cases, over 99% of the error recovered for each wavelength. Again, the longer wavelength was not recovered quite as well.

Figure 32(b) shows the reduction in the error metric as a function of minimization iteration for an arbitrary run. The first 20 iterations center the PSFs close to the optical axis. Significant and quick improvements occur when optimizing based upon Zernike coefficients, with incremental improvements following the major initial reductions. The point-by-point phase optimization also produces some benefit, but the effect is minor.

Phase images for an arbitrary run are shown in Figure 33. A comparison to Figure 20 through Figure 22 readily establishes visually that the algorithm would be expected to work quite well at two single wavelengths.

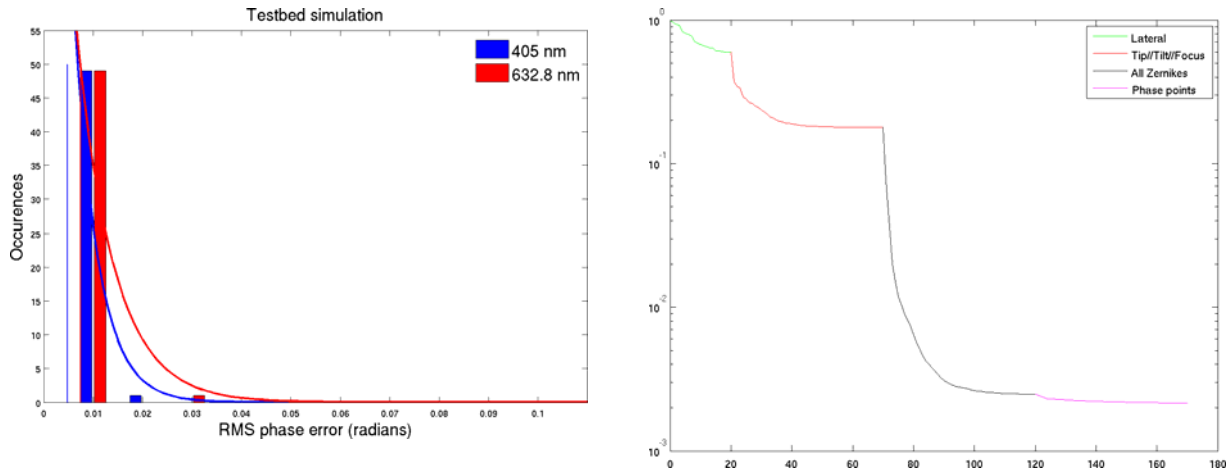

(a) (b)

Figure 32: Simulation of testbed.
(a) Histogram showing remaining wavefront RMS error after reconstruction at the two wavelengths. The vertical lines represent the mean value of the remaining RMS error. The curves represent a log-normal plot with the given mean value, and are included for visualization purposes only. (b) Plot showing progress in reducing the error function for an arbitrary simulation.

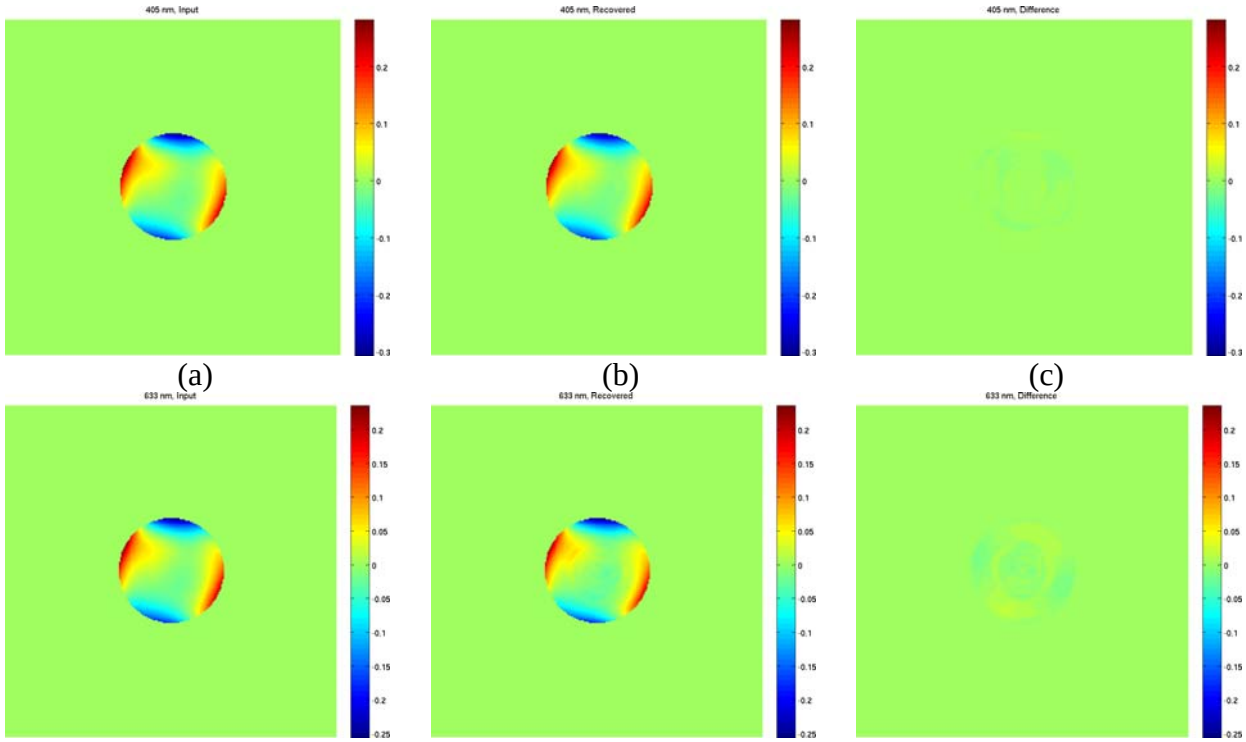

(a) (b) (c)

(d) (e) (f)

Figure 33: Wavefront images from arbitrary simulation.
Leftmost column shows phase error used to create the PSFs. Middle column shows recovered phase error. Rightmost column shows the difference between the recovered and the simulated error. Images (a) – (c): 425 nm. Images (d) – (f): 632.8 nm.

Actual data were collected for the two-wavelength case using the testbed. The following figures show the reconstructed wavefronts.

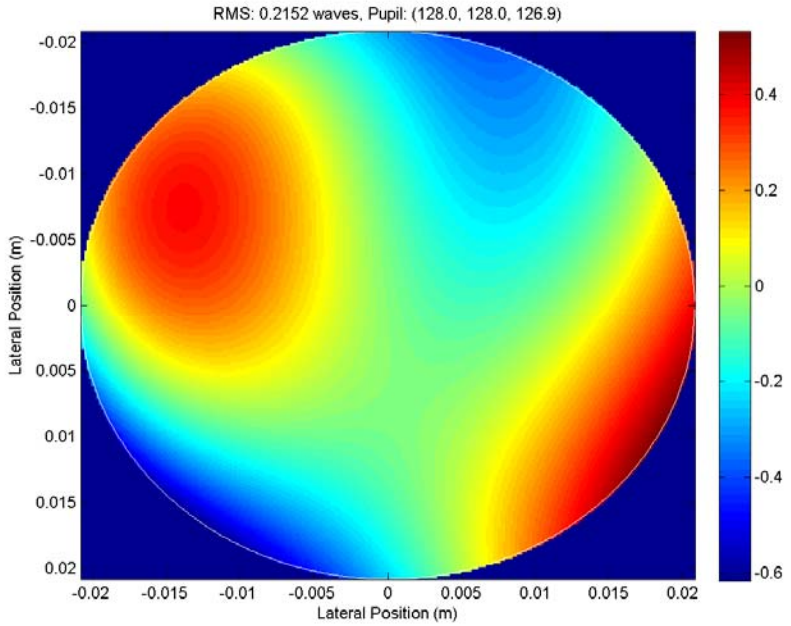

Figure 34: 405 nm Wavefront Reconstructed from Two-Wavelength Data

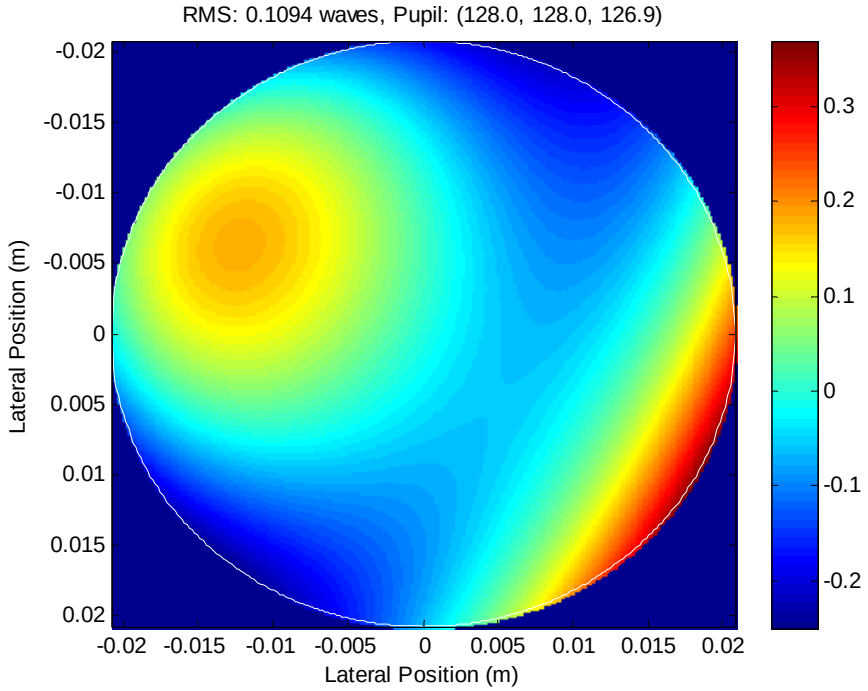

Figure 35: 632.8 nm Wavefront Reconstructed from Two-Wavelength Data

The two reconstructed wavefronts agree well with the monochromatic measurements. The following plot shows NRMSE versus position for this test; all defocus depths were used in the optimization.

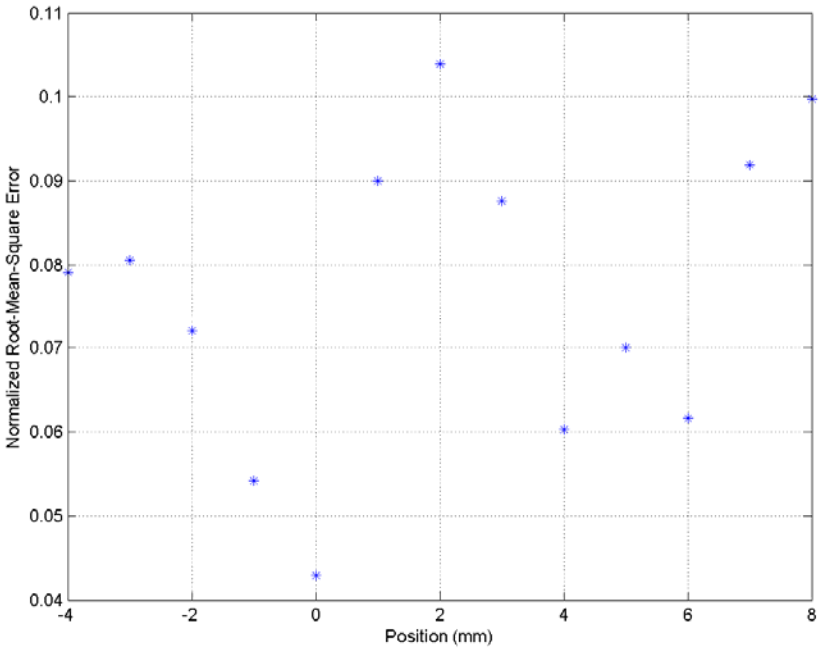

Figure 36: NRMSE vs. Position for the Two-Wavelength Phase Diversity Reconstruction

The reconstructed PSFs do show slight errors relative to the reconstructed PSFs. The following figure shows the PSFs at the 8 mm position.

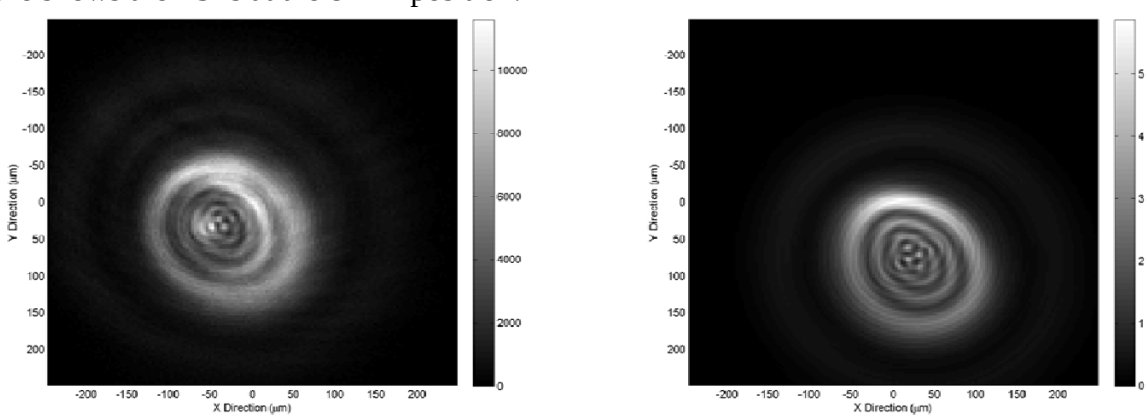

Measured PSF Reconstructed PSF

Figure 37: Measured and Reconstructed PSFs at 8 mm Position for the Two-Wavelength Test

There is some asymmetry in the measured PSF that is not present in the reconstructed PSF.

6 CONCLUSIONS

A method for incorporating wavelength-varying wavefront information in a broadband phase-diverse phase retrieval algorithm has been devised and presented. This algorithm extends earlier work in broadband phase-diverse phase retrieval by allowing the wavefront variations as a function of wavelength to be optimized rather than specified. This algorithm also allows the spectral weights to be optimized, potentially allowing the spectrum of an unknown point source to be characterized by a panchromatic imaging system.

Simulation results for the broadband PDPR algorithm demonstrate its utility. Accurate reconstructions were achieved under a variety of circumstances, including the case where fewer wavelengths were considered in the reconstruction as compared to the simulation. This is an encouraging result, as it more closely simulates what happens when reconstructions are performed with a true broadband source. The accuracy of the reconstruction was generally poorer at longer wavelengths compared to shorter wavelengths. This is believed to be due to the fact that shorter wavelengths are responsible for the sharper features in the PSF and are hence better determined by the data.

An experimental test was performed with two wavelengths. Results of this testing indicate that the algorithm can successfully retrieve the wavefront at two different wavelengths from a polychromatic measurement. No assumption on the variation of wavefront as a function of wavelength is imposed.

Future work on this program would continue with the two-wavelength testing to see if the agreement could be improved further. Some testing indicates that improved reconstructions may be possible when defocus depths are added one at a time to the optimization routine, rather than a single optimization being performed simultaneously over all defocus depths. Testing could also be performed with a different test lens where the shape of the wavefront varied more as a function of wavelength.

Next, optimizations assuming that the wavefronts as a function of wavelength are known but the spectral weights are not could be performed. The same two-wavelength test configuration and data could be used for this analysis.

Lastly, testing could be conducted with a full broadband source. Careful characterization of the spectral response of the testbed system would need to be made. This includes characterizing the response of any optics used as well as the spectral response of the detector.

7 REFERENCES

Fienup, J. R. "Phase retrieval for undersampled broadband images." *J. Opt. Soc. Am. A* 16, no. 7 (July 1999): 1831-1837.

Fienup, James R. "Invariant error metrics for image reconstruction." *Appl. Opt.* 36, no. 32 (1997): 8352-8357.

Fletcher, Roger. *Practical Methods of Optimization.* 2nd. Chichester: John Wiley and Sons, 1987.

Goodman, Joseph W. *Introduction to Fourier Optics.* 2nd. New York: McGraw-Hill, 1996.

Noll, R. J. "Zernike Polynomials and Atmospheric-Turbulence." *J Opt Soc Am* 66, no. 3 (March 1976): 207-211.

Thurman, Samuel T, Ryan T DeRosa, and James R Fienup. "Amplitude metrics for field retrieval with hard-edged and uniformly illuminated apertures." *JOSA A* 26, no. 3 (2009): 700-709.

APPENDIX A: ZERNIKE COEFFICIENTS

The Zernike polynomials are a set of polynomials that are orthogonal over the unit circle. A number of ordering and scaling conventions are used in the literature and by various software packages. The convention used here are the orthonormal Zernike coefficients described by Noll (Noll 1976). The following figure shows the first fifteen polynomials.

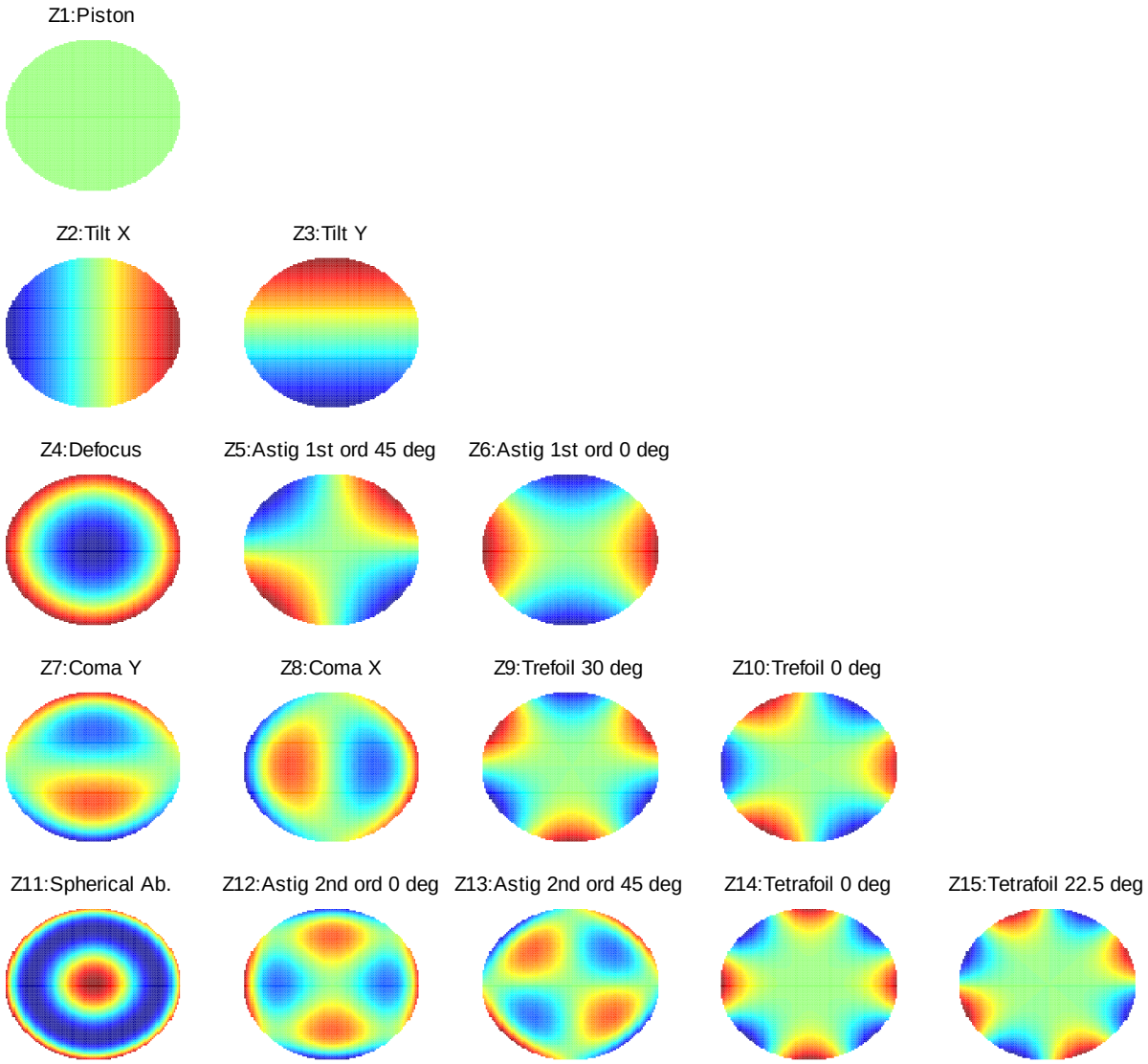

Figure 38: The First 15 Standard Zernike Polynomials

The following table provides the equations for the first fifteen Zernike polynomials using Noll's convention:

Zernike #	n	m	Equation	Description
1	0	0	1	Piston
2	1	0	$2r\cos(\phi)$	Tilt X
3	1	1	$2r\sin(\phi)$	Tilt Y
4	2	0	$\sqrt{3}\left(2r^2-1\right)$	Defocus
5	2	1	$\sqrt{6}r^2 sin(2\phi)$	Astig 1st ord. 45 deg
6	2	2	$\sqrt{6}r^2\cos(2\phi)$	Astig 1st ord. 0 deg
7	3	0	$\sqrt{8}(3r^3-2r)\sin(\phi)$	Coma Y
8	3	1	$\sqrt{8}(3r^3-2r)\cos(\phi)$	Coma X
9	3	2	$\sqrt{8}r^3\sin(3\phi)$	Trefoil 30 deg
10	3	3	$\sqrt{8}r^3\cos(3\phi)$	Trefoil 0 deg
11	4	0	$\sqrt{5}\left(6r^4-6r^2+1\right)$	Spherical Aberration
12	4	1	$\sqrt{10}(4r^4-3r^2)\cos(2\phi)$	Astig 2nd ord 0 deg
13	4	2	$\sqrt{10}(4r^4-3r^2)\sin(2\phi)$	Astig 2nd ord 45 deg
14	4	3	$\sqrt{10}r^4\cos(4\phi)$	Tetrafoil 0 deg
15	4	4	$\sqrt{10}r^4\sin(4\phi)$	Tetrafoil 22.5 deg

Table 6: Definition of the First 15 Standard Zernike Polynomials

DISTRIBUTION

1	MS0406	Eric Shields	Org. 5712
1	MS1153	James Gruetzner	Org. 5444
1	MS0899	Technical Library	Org. 9536 (electronic copy)
1	MS0359	D. Chavez, LDRD Office	Org. 1911

Sandia National Laboratories